

UNIVERSITY OF SOUTHAMPTON

**Disc Winds Matter: Modelling
Accretion and Outflow on All Scales**

by

James Matthews

A thesis submitted in partial fulfillment for the
degree of Doctor of Philosophy

in the
Faculty of Physical Sciences and Engineering
Department of Physics & Astronomy

March 2016

“Here, on the edge of what we know, in contact with the ocean of the unknown, shines the mystery and the beauty of the world.

And it’s breathtaking.”

Seven Brief Lessons on Physics, Carlo Rovelli

“Good enough for government work.”

Christian Knigge

UNIVERSITY OF SOUTHAMPTON

Abstract

Faculty of Physical Sciences and Engineering

Department of Physics & Astronomy

Doctor of Philosophy

by James Matthews

The Thesis Abstract is written here (and usually kept to just this page). The page is kept centered vertically so can expand into the blank space above the title too...

Acknowledgements

The acknowledgements and the people to thank go here, don't forget to include your project advisor...

Contents

Abstract	ii
Acknowledgements	iii
1 Introduction	1
1.1 The Physics of Accretion	3
1.1.1 Spherical Accretion and The Eddington Limit	3
1.1.2 Accretion Discs	4
1.1.2.1 Steady-state Accretion Discs: The α -prescription	5
1.2 Accreting Compact Binaries	7
1.2.1 Roche Lobe-Overflow	7
1.2.2 Cataclysmic Variables	8
1.2.2.1 Nova-like Variables	9
1.2.2.2 Dwarf Novae and the Disc-instability Model	9
1.2.3 Low Mass X-ray Binaries	9
1.3 Quasars and Active Galactic Nuclei	12
1.3.1 AGN Taxonomy	12
1.3.1.1 Radio Galaxies	12
1.3.1.2 BL Lacs and Blazars	12
1.3.1.3 LINERs	14
1.3.1.4 Low-luminosity AGN	14
1.3.2 AGN Unification and the dusty Torus	14
1.3.3 The Broad Line Region and Connection to Outflows	15
1.4 The Current Understanding of the Disc Continuum	17
1.4.1 The Spectral shape of CV discs	17
1.4.2 The Big Blue Bump in AGN	17
1.4.2.1 The Accretion Disc Size Problem	17
1.4.2.2 The Soft-Xray Excess	17
1.5 The Universality of Accretion	17
1.5.1 The RMS-flux relation	18
1.5.2 Accretion States	19
1.5.3 Jets and Outflows	19
1.5.4 A Global Picture	19
2 Accretion Disc Winds	20
2.1 Accretion Disc Winds: Observational Evidence	20

2.1.1	Cataclysmic Variables	20
2.1.2	X-ray Binaries	20
2.1.3	AGN and Quasars	20
2.1.3.1	Broad Absorption Line Quasars	20
2.1.3.2	Warm Absorbers	20
2.1.3.3	Ultra-fast Outflows	20
2.1.4	Stellar Winds	20
2.1.4.1	Clumping	20
2.2	Accretion Disc Winds: Driving Mechanisms	20
2.2.1	Thermal Winds	21
2.2.2	Radiatively Driven Winds	22
2.2.3	Line-driven Winds	22
2.2.4	Magneto-centrifugal Winds	22
2.3	Accretion Disc Wind Models	22
2.4	A Kinematic Prescription	22
2.5	The really, really big picture: AGN Feedback	22
2.5.1	Observational evidence for feedback	22
2.5.2	Radiative or quasar mode feedback	24
2.5.3	Kinetic or radio mode feedback	24
2.5.4	In-situ Explanations	24
3	Radiative Transfer and Ionization	25
3.1	Fundamentals of Radiative Transfer	25
3.1.1	Spectral Line Formation	27
3.1.2	The Two Level Atom	27
3.1.2.1	Einstein Coefficients	27
3.1.2.2	Collision Strengths	28
3.1.3	The Sobolev Approximation	28
3.1.3.1	Escape Probabilities	29
3.1.4	Monte Carlo approaches	29
3.2	PYTHON: A Monte Carlo Ionization and Radiative Transfer Code	29
3.2.1	Basics	29
3.3	Macro-atoms	31
3.3.1	Macro-Atom Estimators	33
3.3.1.1	Radiation Field Estimators	33
3.3.1.2	Heating And Cooling Estimators	33
3.3.2	Ionization Fractions and Level Populations	33
3.4	Simple-atoms	33
3.5	Heating And Cooling	33
3.5.1	Heating And Cooling Balance	33
3.5.2	Heating And Cooling Estimators	33
3.5.2.1	Macro-atoms	33
3.5.2.2	Simple-atoms	34
3.6	Spectral Synthesis	35
3.7	Atomic Data	35
3.8	Clumping	36
3.8.1	Motivation	36

3.8.2	Microclumping	37
3.9	Code Validation	38
3.9.1	Testing against Cloudy	38
3.9.2	Testing against Tardis	38
3.10	Code Maintenance and Version Control	38
3.10.1	Parallelisation	38
4	The Impact of Accretion Disc Winds on the Optical Spectra of Cataclysmic Variables	39
4.1	Introduction	39
4.2	PYTHON: A MONTE CARLO IONIZATION AND RADIATIVE TRANSFER CODE	42
4.2.1	Basics	42
4.2.2	Ionization and Excitation: ‘Simple Atoms’	43
4.2.3	Ionization and Excitation: Macro-Atoms	44
4.2.4	Ionization and Excitation: A Hybrid Approach	45
4.2.5	Atomic Data	46
4.2.6	Code Validation and Testing	46
4.3	Describing the System and its Outflow	46
4.3.1	Wind Geometry and Kinematics	47
4.3.2	Sources and Sinks of Radiation	49
4.3.2.1	Accretion disc	50
4.3.2.2	White Dwarf	50
4.3.2.3	Boundary Layer	50
4.3.2.4	Secondary Star	51
4.4	A Benchmark disc Wind Model	52
4.4.1	Physical Structure and Ionization State	52
4.4.2	Synthetic Spectra	53
4.5	A Revised Model Optimized for Optical Wavelengths	57
4.5.1	Synthetic Spectra	58
4.5.2	Continuum Shape and the Balmer Jump	60
4.5.3	Line Profile Shapes: Producing Single-Peaked Emission	61
4.5.4	Sensitivity to Model Parameters	64
4.5.5	Comparison to RW Tri	65
4.6	Conclusions	66
5	Testing Quasar Unification: Radiative Transfer In Clumpy Winds	68
5.1	Introduction	68
5.2	Ionization and Radiative Transfer	71
5.2.1	Line transfer	71
5.2.2	Ionization and Excitation Treatment	72
5.2.3	Physical Processes	72
5.2.4	Atomic Data	73
5.3	A Clumpy Biconical Disk Wind Model for Quasars	73
5.3.1	Photon Sources	73
5.3.2	Kinematics and Geometry	74
5.3.3	A Simple Approximation for Clumping	75

5.3.4	The Simulation Grid	76
5.4	Results and Discussion From A Fiducial Model	77
5.4.1	Physical Conditions and Ionization State	77
5.4.2	Synthetic Spectra: Comparison to Observations	80
5.4.2.1	Broad absorption lines ('BALQSO-like' angles)	80
5.4.2.2	Broad emission lines ('quasar-like' angles)	83
5.4.3	X-ray Properties	85
5.4.4	LoBALs and Ionization Stratification	86
5.4.5	Parameter Sensitivity	87
5.5	Summary And Conclusions	88
 Bibliography		 90

Chapter 1

Introduction

“And now you’re asking, I don’t know where to begin”

Mike Vennart, Silent/Transparent

The release of gravitational potential energy as mass falls towards a compact object is the most efficient energetic process in the universe, capable of liberating more rest mass energy than nuclear fusion. This *accretion* process is thought to power the huge radiative engines at the centres of every galaxy – accreting supermassive black holes known as active galactic nuclei (AGN). As the matter falls into the potential well of the black hole it often forms an accretion disc, which, in many cases, is an efficient radiator of the gravitational energy released. In some cases, the accretion disc can outshine the entire stellar population of the galaxy, appearing as a quasi-stellar object (QSOS) or *quasar*. In addition to AGN, accretion discs are present in X-ray binaries (XRBs), young-stellar objects (YSOs) and cataclysmic variables (CVs). Accretion is a universal process; broadly speaking, the physics is similar of whether matter is falling on to a $\sim 1 M_\odot$ Neutron Star or White Dwarf system, or a $\sim 10^{10} M_\odot$ black hole.

Outflows are ubiquitous in accreting systems. We see collimated radio jets in AGN (Hazard et al. 1963; Potash and Wardle 1980; Perley et al. 1984; Marscher 2006) and XRBs (Belloni 2010), and there is even evidence of extended radio emission in CVs (Benz et al. 1983; Coppejans et al. 2015). These radio jets tend to appear in specific accretion states (Fender 2001; Körding et al. 2008), implying an intrinsic connection to the accretion process. Even more intriguing, in XRBs less collimated, mass-loaded outflows or *winds* are observed in the opposite accretion state, possibly emanating from the accretion disc. Evidence for disc winds is widespread across the mass range, but perhaps the most spectacular indication is the blue-shifted, broad absorption lines (BALs) in the rest-frame ultraviolet (UV) seen in high-state CVs (Heap et al. 1978; Greenstein and

Oke 1982; Cordova and Mason 1982) and the so-called broad absorption line quasars (BALQSOs) that make up 20 – 40% of quasars (Weymann et al. 1991; Knigge et al. 2008; Allen et al. 2011). BALs and ‘P-Cygni’ profiles (?Rottenberg 1952) are also seen in stellar winds (e.g. Cassinelli 1979) and sometimes even in the optical spectra of CVs (Patterson et al. 1996; Ringwald and Naylor 1998; Kafka and Honeycutt 2004). Broad, blue-shifted absorption is even observed in the Fe K α line in AGN (Reeves et al. 2003; Pounds and Reeves 2009; Tombesi et al. 2010) – these are known as ultra-fast outflows or UFOs¹.

The astrophysical significance of disc winds extends, quite literally, far beyond the accretion environment. They offer a potential mechanism by which the central accretion engine can interact with the host galaxy and interstellar medium via a ‘feedback’ mechanism (King 2003; Fabian 2012). Feedback is required in models of galaxy evolution (Springel et al. 2005) and may explain the famous ‘ $M - \sigma$ ’ relation (Silk and Rees 1998; Häring and Rix 2004). Winds also offer a natural way to *unify* much of the diverse phenomenology of AGN, CVs and XRBs. The principle of unification can be applied along more than one ‘axis’ of parameter space. For example, there exist elegant models that attempt to explain *all* of the behaviour of quasars with only a central black hole, a jet, an accretion disc, and an associated outflow, by varying the viewing angle (Elvis 2000). Similarly elegantly, it has been shown that much of the behaviour of XRBs is directly applicable to AGN (McHardy et al. 2006), and models of outflows in CVs have been successfully ‘scaled-up’ and applied to quasars and AGN (e.g. Higginbottom et al. 2013).

Despite their clear importance and ubiquity, there are still many unanswered questions relating to the true impact of winds and their underlying physical origins. Here, I aim to address some of these questions, and take steps towards building a more holistic picture of the impact of winds on the spectral appearance and accretion physics of disc systems. This thesis is structured as follows. In the remainder of this chapter, I will give the background accretion theory and detail the successes and failures of accretion disc models when compared to observations, as well as describing the different classes of accreting objects in more detail. In chapter 2, I dedicate some time to specifically discussing the theory of, and observational evidence for, accretion disc winds. In chapter 3, I outline the Monte Carlo radiative transfer (MCRT) and photoionization methods I have used in order to investigate the impact of disc winds on the spectra of accreting systems. The science chapters contain three separate submitted papers, in which we investigated the impact of disc winds on the spectra of CVs (Chapter 5), and tested disc wind quasar unification models (Chapters 6 and 7). In chapter 8, I summarise my

¹It should be noted that, while X-ray spectral fitting can be somewhat of a dark art, the explanations for these UFOs are somewhat more believable than their sci-fi namesakes.

findings and their astrophysical significance, and discuss potential avenues for future work.

1.1 The Physics of Accretion

The basic phenomenon of accretion- matter falling into a gravitational potential well- is a ubiquitous one in astrophysics. The energy, ΔE , released by a parcel of mass Δm falling onto an object of mass M and radius R_* is given by

$$\Delta E = \frac{GM\Delta m}{R_*}, \quad (1.1)$$

meaning that the accretion power can then be given by

$$L_{acc} = \frac{GM\dot{m}}{R}. \quad (1.2)$$

We can also parameterise any energetic process with the form

$$\Delta E = \eta \dot{m} c^2, \quad (1.3)$$

where η is some efficiency. Nuclear fusion is one of the more efficient energetic processes in the universe, with an efficient of $\eta = 0.007$. If we rearrange the above equations in terms of η we find

$$\eta = \frac{G}{c^2} \frac{M}{R}. \quad (1.4)$$

In other words, the efficiency of accretion is directly related to the *compactness* of the central object. Values of compactness for four different compact objects are shown in table ??.

1.1.1 Spherical Accretion and The Eddington Limit

The simplest geometry one might propose for accretion would be one in which a central mass accretes matter from an all-encompassing cloud or the inter-stellar medium. The process of spherical accretion has come to be known as Bondi-Hoyle-Lyttleton accretion ([Hoyle and Lyttleton 1939; Bondi and Hoyle 1944](#)). In particular, [Bondi \(1952\)](#) studied spherically symmetric accretion onto a point mass and derived the Bondi radius,

$$r_B = \frac{GM}{c_S^2}, \quad (1.5)$$

where $c_S = c_S(r_B)$ is the sound speed as a function of radius. The Bondi radius represents a critical point inside which the material is supersonic and will accrete on the free-fall timescale.

If this timescale is long enough, then the accreting matter can radiate its potential energy with luminosity L . This radiation can induce a force on free electrons, given by

$$F_{rad} = \frac{L\sigma_T}{4\pi r^2 c}, \quad (1.6)$$

where $\sigma_T = 6.65 \times 10^{-25} \text{ cm}^2$ is the Thomson cross-section. If this radiation force term dominates the inwards gravitational force then the material will no longer fall inwards. Consider radiation pressure acting on electron-proton pairs, for which the gravitational force is approximately given by GMm_p/r^2 . Combining this expression with equation 1.6 gives a natural maximum accretion luminosity, known as the *Eddington limit*, of

$$L_{Edd} = \frac{4\pi GMm_p c}{\sigma_T}, \quad (1.7)$$

with an associated Eddington accretion rate of

$$\dot{m}_{Edd} = \frac{L_{Edd}}{\eta c^2}. \quad (1.8)$$

The Eddington limit makes a number of assumptions, namely that the accretion flow is steady, spherically symmetric, ionized, and has its opacities dominated by electron scattering. Clearly, there are many astrophysical situations where this does not hold. For example, the recent outburst of V404 Cyg showed wildly variable luminosities on short timescales (see, e.g., [Kuulkers et al. 2015](#); [Motta et al. 2015](#), among many, many ATels), and in any binary system or disc dominated system then the assumption of spherical symmetry will break down. Nevertheless, the Eddington limit gives a good order of magnitude estimate of the maximum luminosity of an accreting object, and also provides a useful way of parameterising accretion rate, as it scales linearly with mass.

1.1.2 Accretion Discs

As well as losing gravitational potential energy as it falls towards the central mass, a parcel of matter must always lose angular momentum. If the disc itself maintains the same total angular momentum, then it follows that angular momentum must therefore be transported outwards.

1.1.2.1 Steady-state Accretion Discs: The α -prescription

The so-called α -disc model developed by ([Shakura and Sunyaev 1973](#), hereafter SS73) is currently the leading candidate for explaining how energy and angular momentum is transported an accretion disc. The starting point for this model is the parameterisation of viscosity using a simple form of

$$\nu = \alpha c_s H. \quad (1.9)$$

Viscous torques then allow the conversion of orbital kinetic energy into heat, which can be radiated away. If we then make one further assumption, that the accretion rate is constant throughout the disc, then we can write down a mass continuity equation valid at all radii, given by

$$\dot{m} \equiv 2\pi R V_R \Sigma = 0 \quad (1.10)$$

where Σ is the surface density at that point. The angular momentum equation becomes, in this case

$$\nu' \Sigma = \frac{\dot{m}}{3\pi} \left[1 - \left(\frac{R}{R_*} \right)^{1/2} \right] \quad (1.11)$$

The viscous torques throughout the disc cause a local loss of mechanical energy, allowing one to derive (see, e.g. [Frank et al. 1992](#)) a rate of viscous dissipation, per unit area, given by

$$D(R) = \frac{1}{2} \nu' \Sigma (R \Omega')^2. \quad (1.12)$$

Here, $D(R)$ is proportional to the derivative of the angular velocity, $\Omega' = d\Omega/dR$. By combining equations 1.12 and 1.11 we can show that the viscous dissipation rate is

$$D(R) = \frac{GM\dot{m}}{8\pi R^3} \left[1 - \left(\frac{R}{R_*} \right)^{1/2} \right] \quad (1.13)$$

where we have also set the angular velocity to the Keplerian velocity. This expression is, importantly, independent of viscosity – which is fortunate, because we do not know what value of α to use in equation 1.9. This result comes about because of the implicit assumption that the viscosity regulates the mass accretion rate so as to achieve a steady state.

We can now integrate across the whole disc to obtain the disc luminosity,

$$L_{disc} = 2 \int_{R_*}^{\infty} D(R) 2\pi R dR = \frac{GM\dot{m}}{2R_*} = \frac{1}{2} L_{acc}. \quad (1.14)$$

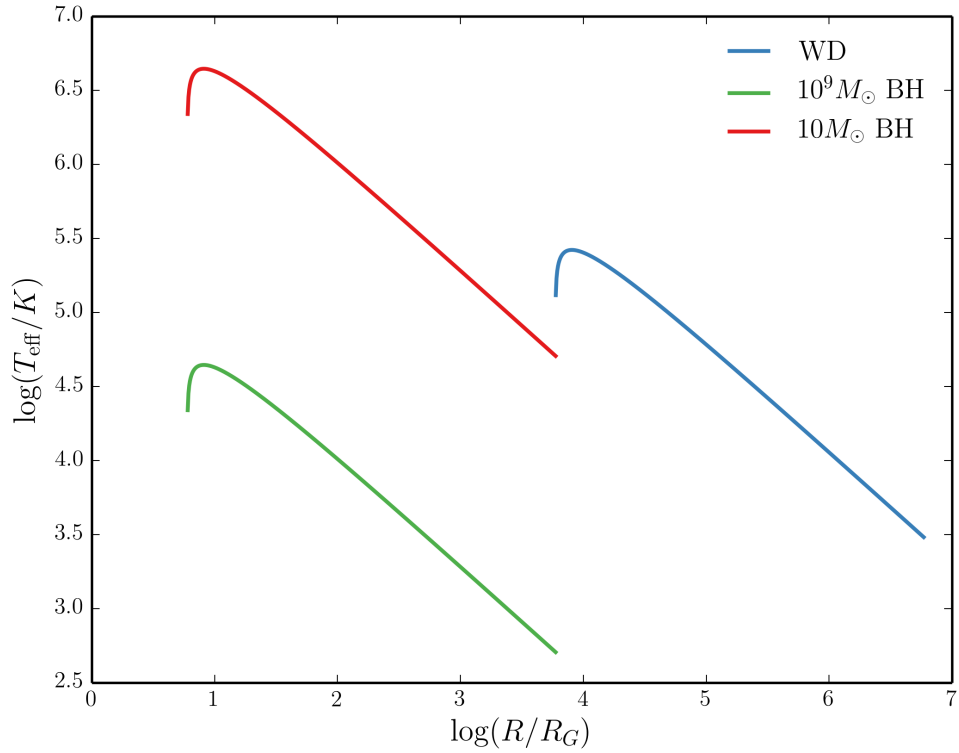


FIGURE 1.1: The temperature profile of an accretion disc for three different classes of compact object.

This result can also be shown by considering the binding energy of gas at R_* and infinity. From equation 1.13 one can also derive an effective temperature distribution, by setting

$$\sigma T_{eff}^4(R) = D(R), \quad (1.15)$$

which then gives

$$T_{eff}(R) = T_*(R/R_*)^{-3/4}, \quad (1.16)$$

where

$$T_* = \left(\frac{3GM\dot{m}}{8\pi R_*^3 \sigma} \right)^{1/4}. \quad (1.17)$$

Now we have not only derived the total luminosity of an accretion disc, but also the effective temperature profile which will govern the shape of the emergent SED. This temperature profile is shown in figure ?? for the same four objects shown in table ??, assuming an Eddington fraction of 0.2.

It is important to recognise that the steady-state disc treatment *does not specify the nature of the disc SED*. What it does do is say where energy is originally released. Typically, accretion discs are modelled as a series of annuli each emitting as blackbodies,

but a disc atmosphere with frequency-dependent opacity would create a somewhat different spectrum. Figure ? shows the blackbody SEDs expected for the same objects as figure 1.1. Figure ? shows a comparison between a disc atmosphere model and blackbody model for a cataclysmic variable accretion disc, showing the differences in spectral shape caused by frequency-dependent opacities in the disc. It is of course possible that *neither* blackbody or disc atmosphere treatments are realistic. I shall therefore devote a little time to discussing the observational arguments for accretion discs and the different classes of accreting objects.

1.2 Accreting Compact Binaries

Accreting compact binaries form many different classes, but are all characterised by matter streaming from a donor star or secondary onto a compact object or primary. There are only two ways by which matter can transfer from the secondary to the compact object. One is by Roche Lobe-overflow (RLOF), whereby stellar evolution causes the donor star to fill its Roche Lobe, the surface of equipotential around the star. The alternative is that the donor may expel material via a disc around the secondary or radiatively driven stellar wind, allowing some of it to flow onto the compact object. Although accretion from a wind or circumstellar disc is common in such as high-mass X-ray binaries (HMXBs; e.g. Bartlett 2013), here I will focus on RLOF as it is more common in the systems that commonly exhibit high-state accretion discs and associated outflows.

1.2.1 Roche Lobe-Overflow

Let us consider a binary system, with masses M_1 and M_2 , at positions \vec{r}_1 and \vec{r}_2 . The Roche potential, Φ_R , in this system is then

$$\Phi_R = -\frac{GM_1}{|\vec{r} - \vec{r}_1|} - \frac{GM_2}{|\vec{r} - \vec{r}_2|} - 1/2(\vec{\omega} \times \vec{r})^2, \quad (1.18)$$

where ω is the angular velocity of the binary and is a vector normal to the orbital plane. This potential is plotted in figure 1.2 for a mass ratio, $q = M_2/M_1$ of 0.25.

In the context of semi-detached binary systems, the most important region of the potential is the dumbbell shaped region enclosing the masses. Each of these enclosed regions is known as the ‘Roche lobe’ of the object and can be expressed approximately in terms of the mass ratio and separation of the system. If one of the binary stars expands enough to fill its Roche lobe, then matter will fall onto the other object. This process is known

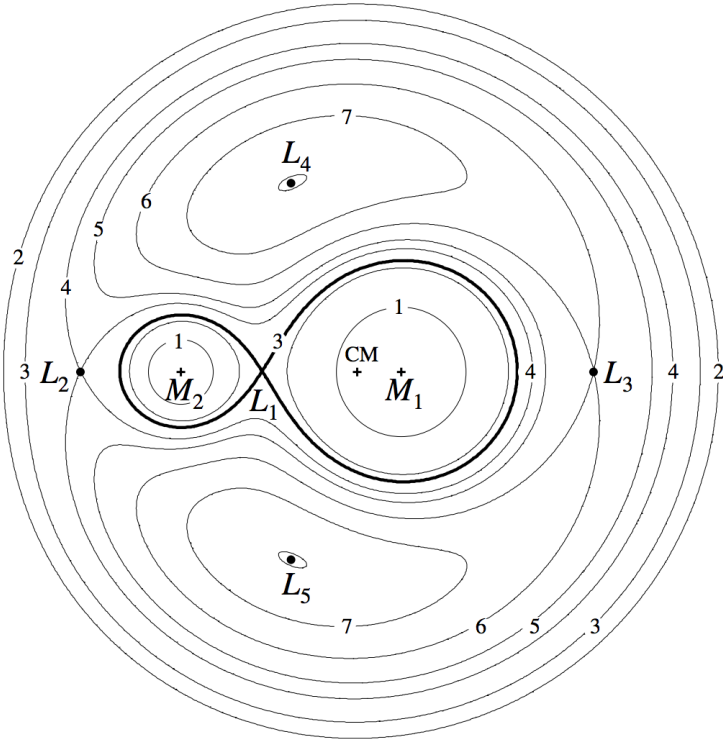


FIGURE 1.2: Credit: Frank et al. 2002. The Roche potential in a binary system for $q = M_2/M_1$ of 0.25. The Lagrangian points are marked, as are the locations of the individual and system centres of mass.

as Roche Lobe overflow (RLOF), and is vitally important in astrophysics. Although caused by stellar evolution, it affects the mass ratio of the binary system and thus itself affects the evolution of binary systems. This has serious ramifications for the orbital period distribution of binaries (REFs) as well as affecting the delay time distribution of Type Ia Supernovae, for which CVs are one of the progenitor candidates. It is also worth noting that the existence of gravitational waves has been required in models for CV evolution since

1.2.2 Cataclysmic Variables

Cataclysmic variables (CVs) are systems in which a white dwarf accretes matter from a donor star via Roche-lobe overflow. CVs are not always accreting objects; classical novae and super soft sources (SSS) have luminosities dominated by nuclear burning. *Accreting* CVs – the focus here – can be classified according to the magnetic field strength (B) and photometric activity. Magnetic systems are classified as either ‘Polars’ ($B \gtrsim 10^7$ G) or ‘Intermediate Polars’ ($10^6 \lesssim B \lesssim 10^7$ G); in these systems the accretion flow is dominated by the WDs magnetic field inside the Alfvén radius (REF). In polars this radius is large enough that no disc forms at all (REFs). When $B \lesssim 10^6$ G then the

accreting material can fall onto the WD via a disc, and the CV is classified as non-magnetic. There are two main types of non-magnetic CVs; Dwarf Novae and Nova-like variables.

1.2.2.1 Nova-like Variables

Nova-like variables (NLs) are similar to DNe in overall structure, except that the disc is always in a relatively high-accretion-rate state ($\dot{M} \sim 10^{-8} M_{\odot} \text{ yr}^{-1}$). NLs are therefore one of the best ‘laboratories’ for testing the steady-state accretion disc theory described in section 1.1.2.1. NLs generally exhibit a series of strong emission lines superposed on a blue continuum.

1.2.2.2 Dwarf Novae and the Disc-instability Model

Dwarf novae (DNe) are accreting systems that are characterised by periods of quiescence and outburst on varying timescales. One of the most famous DNe is SS Cyg, whose century of activity is shown in figure ???. The repeated outbursts, with characteristic shape, can be clearly seen.

1.2.3 Low Mass X-ray Binaries

X-ray binaries are similar to CVs in structure, except that the compact object is either a neutron star (NS) or black hole (BH). The accretion disc emits in the soft X-rays, and an additional hard X-ray power law is also seen in the spectrum (REFs). This hard component is normally attributed to Compton up-scattering of seed disc photons by some kind of ‘corona’ of hot electrons close to the BH (REFs). A characteristic spectrum is shown in figure ??.

Although I do not discuss XRBs directly in this thesis, it is instructive to discuss some of their observational appearance as it is instructive for understanding the theory of disc winds, as well as their wider significance. The discovery that XRBs follow similar tracks on a hardness-intensity diagram (REFs) is particularly interesting in this regard, especially since Ponti et al. (2012) showed that broad Fe absorption lines are only seen in the soft-state high-inclination systems (see section 2.1.2). This implies that equatorial outflows are intrinsic to the accretion process. Although the driving mechanism is almost certainly different to CVs (REFs), the similarity in general structure to models for CVs and quasars is striking.

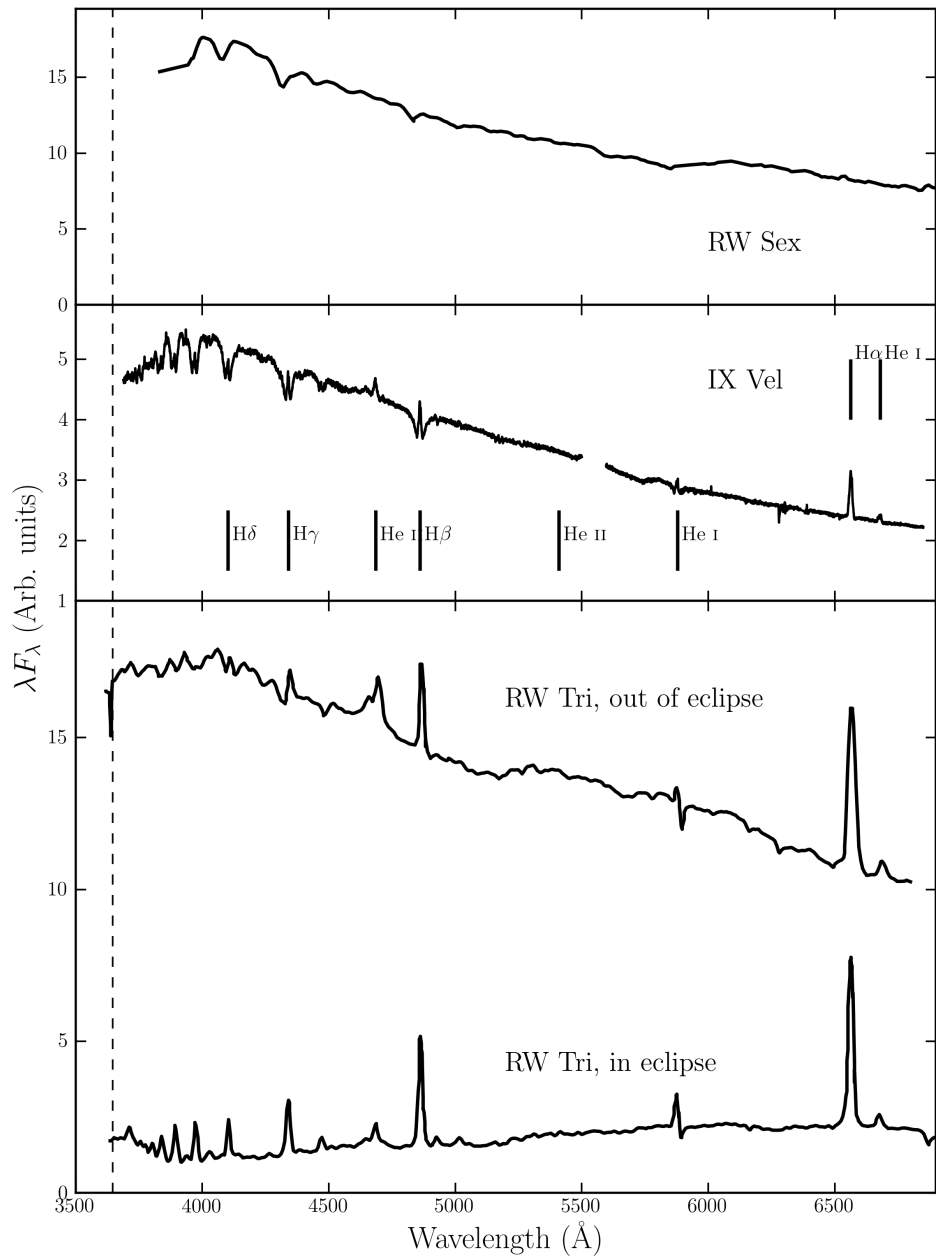


FIGURE 1.3: Optical spectra of three nova-like variables.

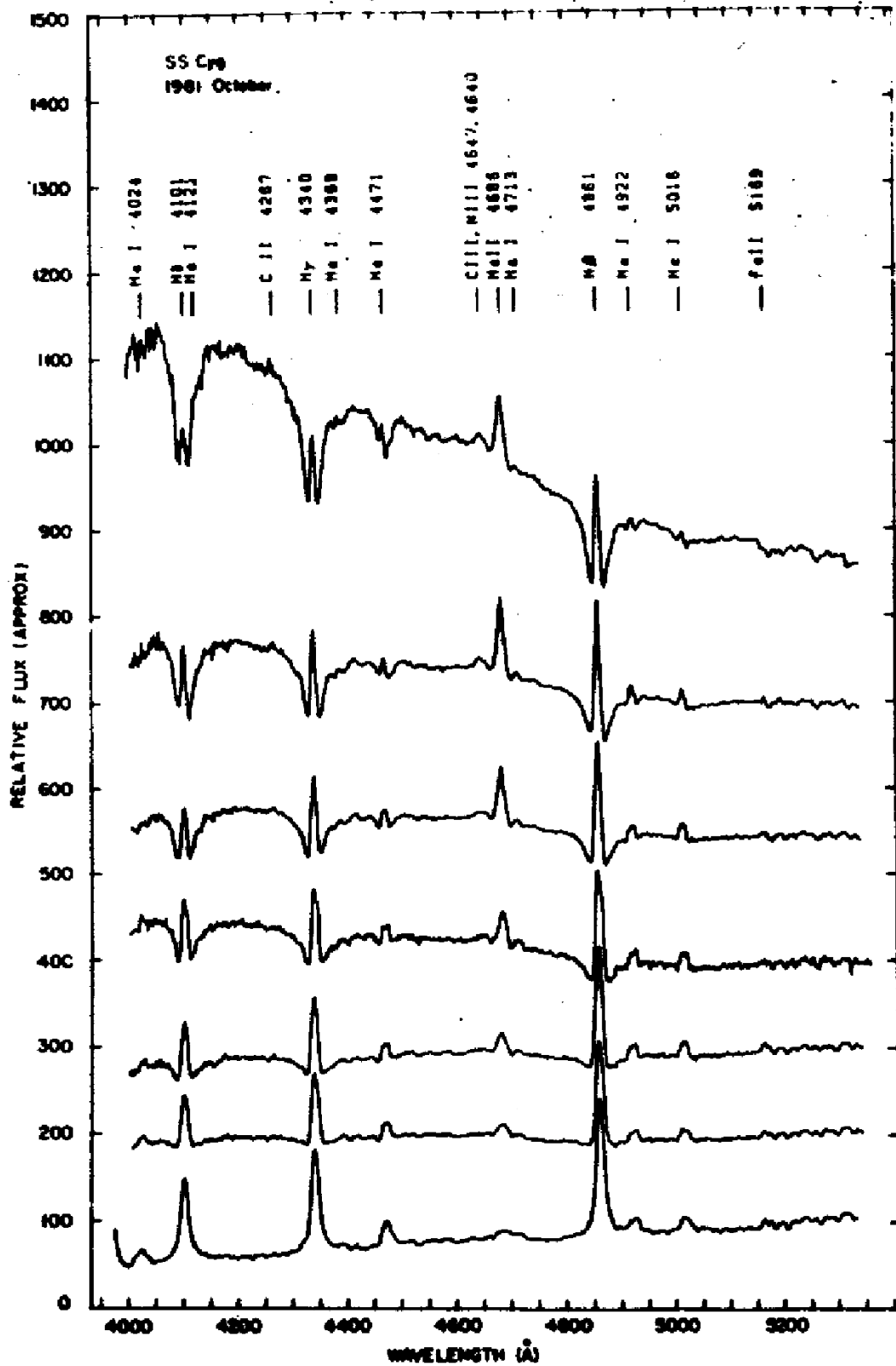


FIGURE 1.4: Credit: Hessman et al. 1984 / Dhillon et al. 1996. Spectra of SS Cyg during an outburst cycle, showing the evolution from minimum to maximum light. The rise is characterised by the appearance of an optically thick accretion disc spectrum. The flux scale is approximate.

1.3 Quasars and Active Galactic Nuclei

Spectra of AGN have now been studied for over 100 years, and we have known that they exhibit strong, broad emission lines since the first spectrum was taken by [Fath \(1909\)](#). However, it wasn't until the work of [Seyfert \(1943\)](#) that the systematic classification of AGN really began, leading to the phrase ‘Seyfert galaxy’. This label was applied to galaxies possessing a bright nucleus, spectroscopically characterised by a blue continuum and a series of strong emission lines. The first real physical insight into the extraordinary nature of AGN was provided by [Woltjer \(1959\)](#), who noted that (i) the nuclei must have sizes < 100 pc, based on the fact that they were unresolved and (ii) the mass of the nucleus must be very high, based on virialised motion. While both of these observations were based on simple arguments, the fact that these ultra-luminous celestial objects are both *compact* and *supermassive* is perhaps the defining insight into the nature of AGN.

Although the field of AGN study was established in the optical, radio astronomy also significantly furthered our understanding of AGN in the mid-20th century. A number of surveys, such as the Cambridge ([Edge et al. 1959](#)), Parkes ([Ekers 1969](#)) and Ohio ([Ehman et al. 1970](#)) surveys discovered a great many bright radio point sources distributed isotropically across the sky. These sources eventually became known as ‘quasi-stellar radio sources’ or *quasars*, and were soon identified to be coincident with bright optical sources or ‘quasi-stellar objects’ (QSOs; REFs). Nowadays, the term quasar normally has very little to do with radio emission and is often used interchangeably with QSO. Indeed, throughout this thesis I shall refer to a quasar as simply a bright, massive AGN; one with sufficiently high luminosity that it dominates the emission from its host galaxy.

1.3.1 AGN Taxonomy

In addition to Seyfert galaxies and quasars, there are a number of different classes of AGN. These are broadly characterised by their spectra in the optical, UV and X-ray as well as their radio behaviour. It is worth noting that these are observational classifications; that is, even after a century of study, the *physical* origins of the diverse behaviour of AGN are still an active area of research.

1.3.1.1 Radio Galaxies

1.3.1.2 BL Lacs and Blazars

BL Lac objects – named for the first object of the class, BL Lacertae – are AGN with featureless non-thermal continua (REFs), in contrast to Seyfert galaxies. Their optical

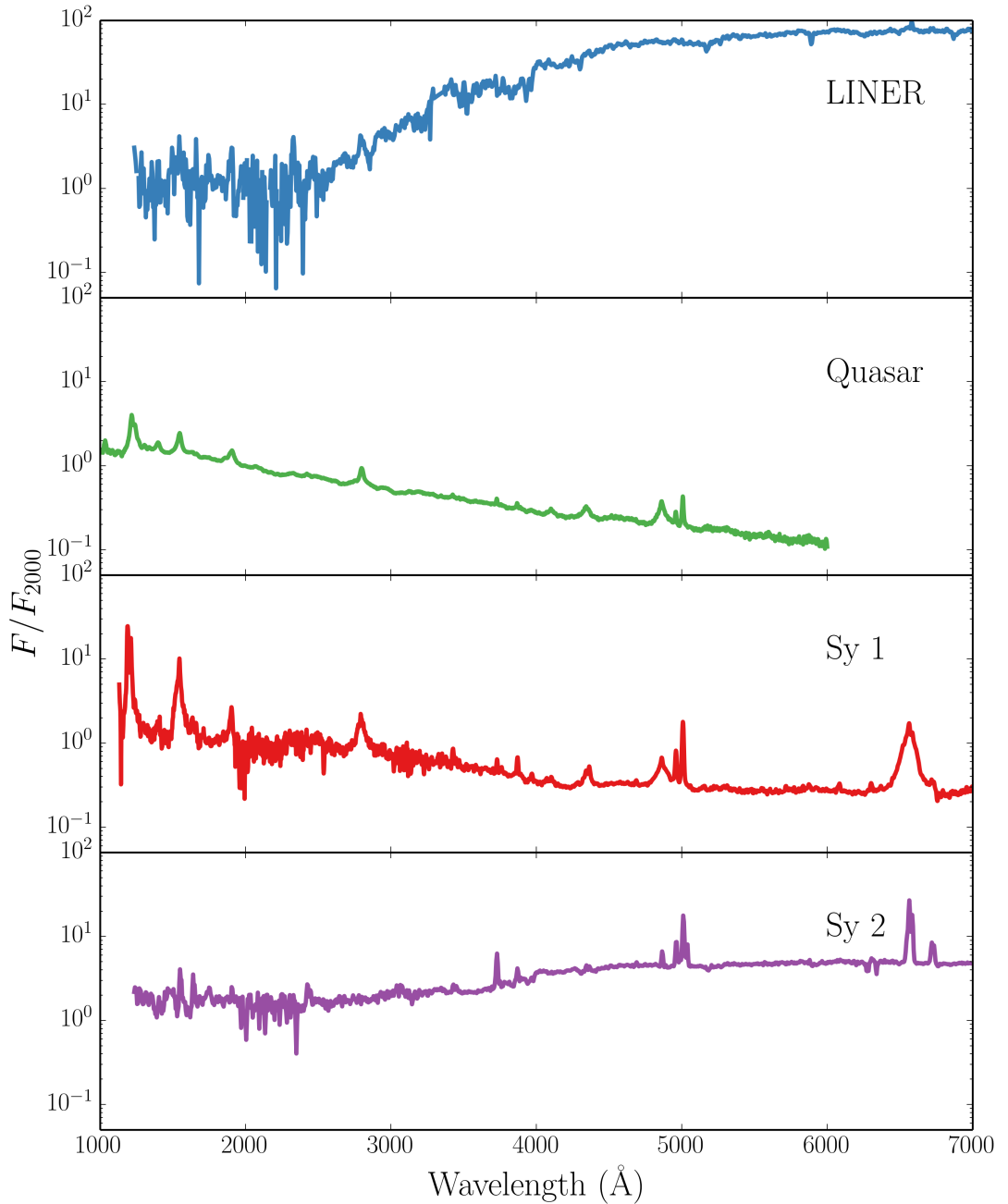


FIGURE 1.5: Template spectra, from the AGN atlas, for four common types of AGN.
Obtained from http://www.stsci.edu/hst/observatory/crds/cdbs_agn.html.

flux is highly polarised (REFs) and they tend to exhibit large-scale optical variability (REFs). BL Lacs are a subset of a larger AGN class known as Blazars, the most luminous of which are known as optically violent variable (OVV) quasars. Blazars require relativistic beaming in order to explain their high radio luminosities (REFs), implying that the jet is orientated towards the observer (REFs). These objects thus have an important place in unification schemes (see section 1.3.2), and also allow us to learn directly about the Lorentz factors and shock physics of relativistic radio jets (REFs).

1.3.1.3 LINERs

1.3.1.4 Low-luminosity AGN

1.3.2 AGN Unification and the dusty Torus

Although Seyfert had identified type 1 and 2 AGN, a physical explanation for this dichotomy was not forthcoming until a study by (Antonucci and Miller 1985, AM85). They showed unambiguously that the nearby Seyfert 2 NGC 1068 is simply an obscured type 1 AGN, by finding that broad emission lines appeared in the spectrum of *polarised* flux. This provided the basis for the first successful attempt to unify AGN behaviour, as it elegantly explained the apparent disconnect between the two types of AGN as simply a viewing angle effect. The obscuring structure became known as the ‘torus’ (Krolik and Begelman 1986), due to its geometry, and it was soon realised that this structure may be made of dust, in which case it could also be responsible for the infra-red (IR) bump in AGN (Neugebauer et al. 1979).

The (Urry and Padovani 1995, UP95) scheme went further than the original unification model proposed by AM85 as it also attempted to explain radio AGN phenomena. The picture they proposed is shown in figure 1.6. This model attempts to explain all of the types of AGN described in section 1.3.1 merely as a function of viewing angle and presence, or lack thereof, of a radio jet.

Since the seminal works by AM85 and UP95, the picture has become somewhat more complicated. Variable X-ray absorption has been detected in so-called ‘Changing look’ AGN (Matt et al. 2003; Puccetti et al. 2007), even in NGC 1068 itself (Marinucci et al. 2016). Changes in type have also been seen in the optical lines; the broad H β component can dramatically disappear or reappear (e.g. Tohline and Osterbrock 1976; Cohen et al. 1986; Denney et al. 2014). The explanation for this could be variable absorption (Elitzur 2012) or linked to the accretion state of the disc. In the latter case, it has even been suggested that a disc wind could be directly responsible for this change in accretion state

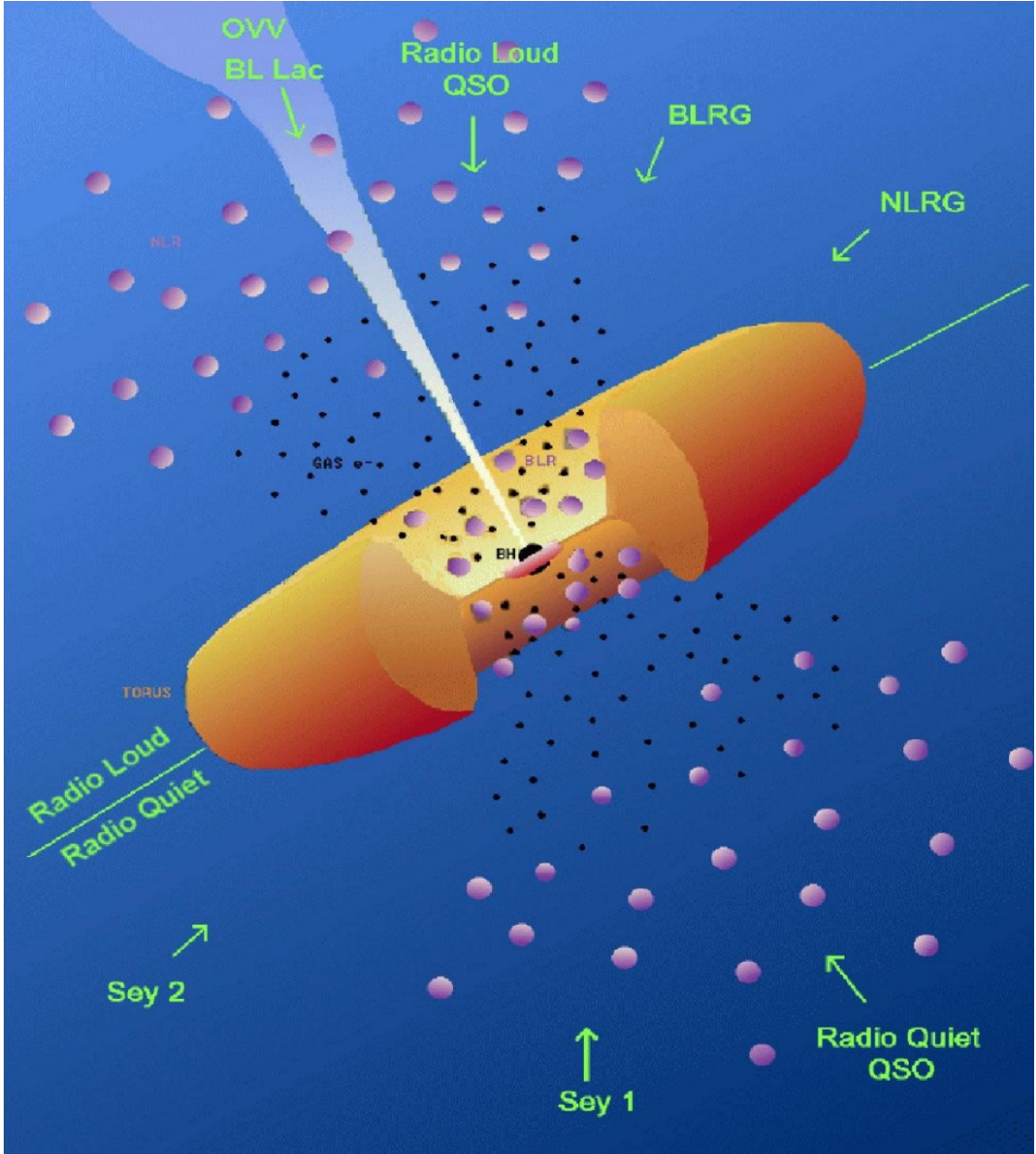


FIGURE 1.6: A unified scheme for AGN.

(Elitzur et al. 2014). Furthermore, dusty *polar* outflows have been found to be important IR emitters (Hönig et al. 2013), implying that, even when it comes to dust, the torus is not the whole picture. Despite these complications, the AGN torus unification picture still helps explain a lot of AGN behaviour, and represents a good framework to test with observations.

1.3.3 The Broad Line Region and Connection to Outflows

In the UP95 unification model, the broad emission lines come from a series of virialised clouds close to the disc plane. As noted by (Murray et al. 1995, hereafter MCGV95),

OCCAM'S QUASAR: THE PRINCIPLE THAT IN EXPLAINING A QUASAR NO MORE ASSUMPTIONS SHOULD BE MADE THAN ARE NECESSARY.

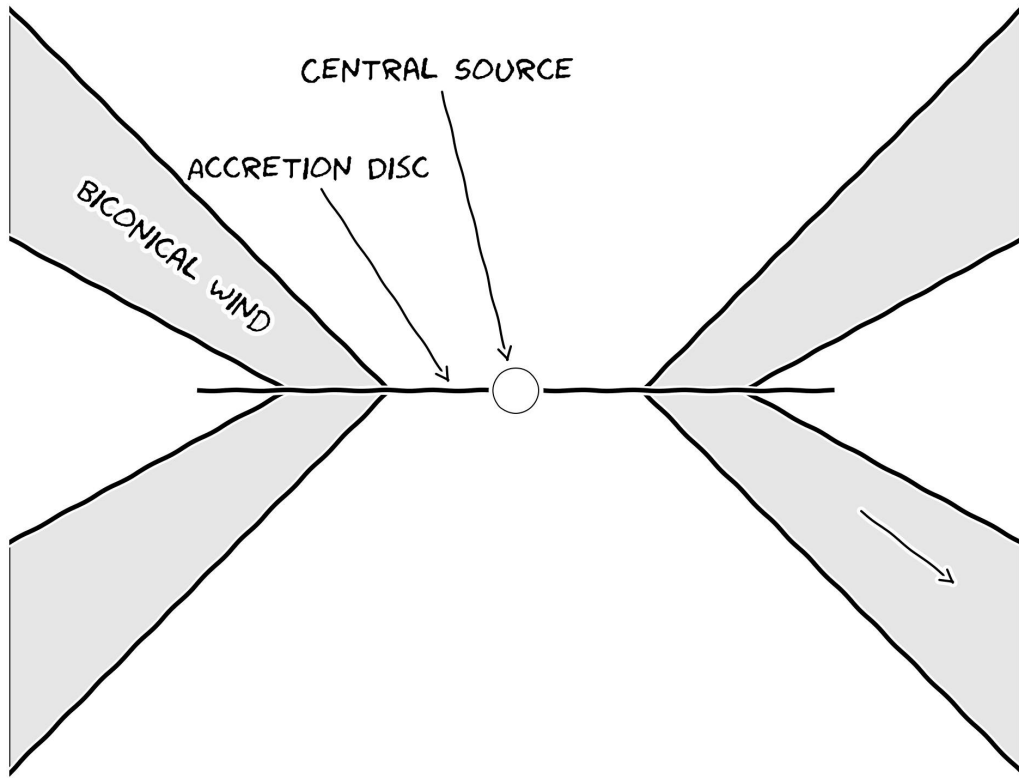


FIGURE 1.7: Occam's quasar. How far can this general picture take us when trying to explain the behaviour of quasars and other accreting compact objects?

there are a number of problems with the BLR ‘cloud’ model, perhaps most notably that there is no obvious physical origin for a series of virialised clouds. While there are exceptions to this statement (REFs), it is important to test other models. Indeed, MCGV95 proposed a disc wind model in order to explain both BALs and BELs in quasars. A disc wind model was also discussed by [Elvis \(2000\)](#), who proposed a structure for quasars that attempted to explain much of the behaviour of luminous AGN merely as a function of viewing angle. Outflow models are discussed further in section 2. The philosophy of these models is that, before invoking additional degrees of freedom in a model, we should first test if known quasar phenomenology (winds) can explain other aspects of their observational appearance. I have illustrated this general principle with the ‘Occam’s quasar’ cartoon shown in figure 1.7. This is the picture that I will quantitatively test in the latter, quasar-focused sections of this thesis, and the general principle can even be applied to cataclysmic variables and other accreting objects.

1.4 The Current Understanding of the Disc Continuum

A number of issues have been raised with the thin-disc model and its applicability to accreting systems.

1.4.1 The Spectral shape of CV discs

Attempts to fit the observed SEDs of high-state CVs with simple disc models have met with mixed success. In particular, the SEDs predicted by most stellar/disc atmosphere models are too blue in the UV (Wade 1988; Long et al. 1991, 1994; Knigge et al. 1998a) and exhibit stronger-than-observed Balmer jumps in absorption (Wade 1984; Haug 1987; La Dous 1989a; Knigge et al. 1998a). One possible explanation for these problems is that these models fail to capture all of the relevant physics. Indeed, it has been argued that a self-consistent treatment can produce better agreement with observational data (e.g. Shaviv et al. 1991; but see also Idan et al. 2010). However, an alternative explanation, suggested by Knigge et al. (1998b; see also Hassall et al. 1985), is that recombination continuum emission from the base of the disc wind might fill in the disc's Balmer absorption edge and flatten the UV spectrum.

1.4.2 The Big Blue Bump in AGN

1.4.2.1 The Accretion Disc Size Problem

One of the most interesting results of recent years relating to AGN and accretion discs is the discovery that the continuum emission region size is a factor ~ 3 larger than predicted by standard Shakura & Sunyaev disc theory. This result has been found independently in both microlensing (?) and reverberation (Edelson et al. 2015).

1.4.2.2 The Soft-Xray Excess

1.5 The Universality of Accretion

Accretion appears to be an important physical processes across ~ 10 orders of magnitude in mass. But is this process the same at all scales? Does any behaviour manifest in all accretion systems?

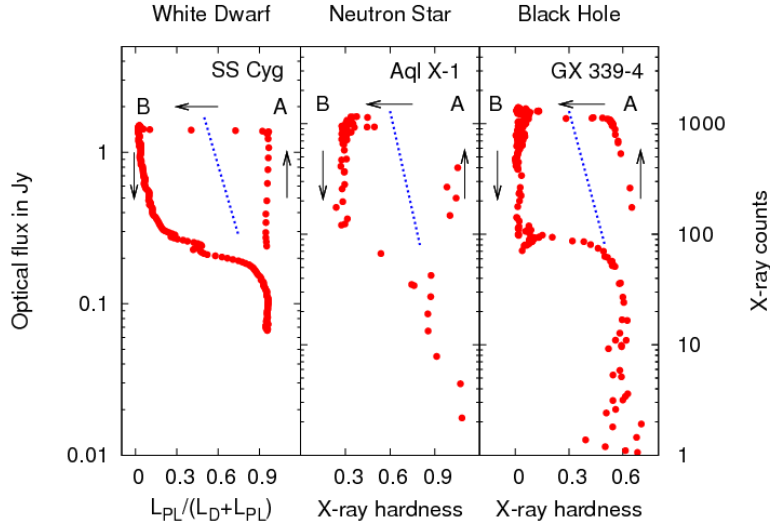


FIGURE 1.8: Credit: Kording et al. XXXX. Caption.

1.5.1 The RMS-flux relation

Broad-band variability is common in all types of accretion disc. It has been known for some time that there exists a linear relationship between the flux and absolute root-mean-square (rms) amplitude of this variability. This was discovered first in XRBs and AGN (Uttley and McHardy 2001; Uttley et al. 2005; Heil et al. 2012), but it has been shown more recently that the relationship extends to CVs and even YSOs (Scaringi et al. 2012, 2015). The relationship is not limited to one type of CV, as it is present in both NLs and DNe (Van de Sande et al. 2015).

The model that best reproduces this behaviour is the so-called ‘fluctuating accretion disc’ model (Lyubarskii 1997; Kotov et al. 2001; Arévalo and Uttley 2006; Hogg and Reynolds 2015). It has been shown that additive processes cannot reproduce the behaviour, and a multiplicative mechanism is required (Uttley et al. 2005). Regardless of the mechanism, the rms-flux relation is one of the most clear-cut examples of a universal accretion phenomenon. It tells us that at least some of the behaviour in CV discs is present in AGN and XRBs, strengthening the argument that CVs should be used as ‘accretion laboratories’.

1.5.2 Accretion States**1.5.3 Jets and Outflows****1.5.4 A Global Picture**

Clearly, accretion physics is relevant to a plethora of astrophysical phenomena. It would also appear that the outflowing material observed in accreting systems has a profound effect on the accretion process itself, as well as acting as a spectral ‘filter’ – modifying, and sometimes dominating the observational appearance of accretion discs.

Chapter 2

Accretion Disc Winds

“A view of space, with an elephant
obstructing it”

Mike Vennart, Silent/Transparent

2.1 Accretion Disc Winds: Observational Evidence

2.1.1 Cataclysmic Variables

2.1.2 X-ray Binaries

2.1.3 AGN and Quasars

2.1.3.1 Broad Absorption Line Quasars

2.1.3.2 Warm Absorbers

2.1.3.3 Ultra-fast Outflows

2.1.4 Stellar Winds

2.1.4.1 Clumping

2.2 Accretion Disc Winds: Driving Mechanisms

Let us consider a parcel of ideal gas. By imposing nothing more than conservation of mass, energy and momentum on that parcel we can write down three equations of

hydrodynamics ¹

$$\frac{D\rho}{Dt} + \rho \nabla \cdot \vec{v} = 0 \quad (2.1)$$

$$\rho \frac{Dv}{Dt} = -\nabla P + \frac{1}{4\pi} (\nabla \times \vec{B}) \times \vec{B} + \rho \vec{F}_{rad} + \rho \vec{g} \quad (2.2)$$

$$\rho \frac{D}{Dt} \left(\frac{e}{\rho} \right) = P \nabla \cdot \vec{v} + \rho \mathcal{L} \quad (2.3)$$

Here D denotes a derivative within the comoving frame of the gas parcel, \vec{v} is the velocity, ρ is the gas density, \vec{B} is the local magnetic field, \vec{F}_{rad} is the radiation force per unit mass and \vec{g} denotes the gravitational acceleration vector. Equation 2.1 is the *continuity equation* and describes conservation of mass. Equation 2.2 is the *equation of motion* and describes conservation of momentum. Equation 2.3 is the *equation of energy conservation*. We can use equation 2.2 to neatly demonstrate how an outflow can be driven. I have deliberately written the equation so that all the force terms lie on the RHS. We can then see that for an outflow to be driven from an accreting object one simply needs one of the terms on the RHS to dominate over gravity, $\rho \vec{g}$. These terms thus signify three potential driving mechanisms.

- Magnetic Forces, $\frac{1}{4\pi} (\nabla \times \vec{B}) \times \vec{B}$.
- Radiative Forces, $\rho \vec{F}_{rad}$.
- Thermal Pressure, $-\nabla P$.

We can now examine under what physical conditions (and in which corresponding astrophysical objects) we might expect these forces to overcome gravity and cause a parcel of mass to escape to infinity. In other words: *what might drive a wind?*

2.2.1 Thermal Winds

In hydrostatic equilibrium (HSE), thermal pressure balances gravity and no other forces are present, meaning that the equation of motion can be written as

$$\rho \frac{Dv}{Dt} = -\nabla P + \rho \vec{g} = 0 \quad (2.4)$$

¹I stress that these equations are not used in hydrodynamic simulations in this thesis (see section ?, for example); they are discussed here because they provide a natural reference point for exploring potential driving mechanisms for winds in accreting systems.

Clearly, if the thermal pressure is then significantly increased then this equilibrium condition no longer holds. This can occur in accretion discs at temperatures in excess of $\sim 10^7$ K – where other forces are negligible compared to thermal pressure – and where the escape velocities are relatively low (i.e. far out in the disc). Due to the temperature and gravity scalings, this means that XRBs are natural candidates for showing evidence of thermally driven winds. The outer disc can be heated to the Compton temperature by the central X-ray source, potentially driving relatively high mass-loss rate outflows ([Begelman et al. 1983](#); [Woods et al. 1996](#)). This driving mechanism has been proposed as a natural explanation for the ever-present equatorial outflows in soft state XRBs ([Ponti et al. 2012](#)). However, they are much less likely candidates in CVs and AGN **Discuss scaling arguments with equations?**.

2.2.2 Radiatively Driven Winds

2.2.3 Line-driven Winds

2.2.4 Magneto-centrifugal Winds

2.3 Accretion Disc Wind Models

2.4 A Kinematic Prescription

2.5 The really, really big picture: AGN Feedback

The event horizon of a $10^9 M_\odot$ BH is approximately 10^{15} cm, a billionth of the size of a typical galactic bulge. This is roughly the difference in size between a small coin and the radius of the Earth. Despite this vast different in scale, there are multiple pieces of evidence that the physics on the scale of the gravitational radius of the BH really does affect the evolution and dynamics of its host galaxy. I shall briefly discuss the evidence for this statement, and assess the potential role of winds together with alternative mechanisms.

2.5.1 Observational evidence for feedback

Perhaps the most famous pieces of evidence for some kind of long-distance relationship between a central BH and its host galaxy are the $M_{BH} - \sigma_*$ and $M_{BH} - M_{bulge}$ correlations, shown in figures ?? and [2.2](#) respectively.

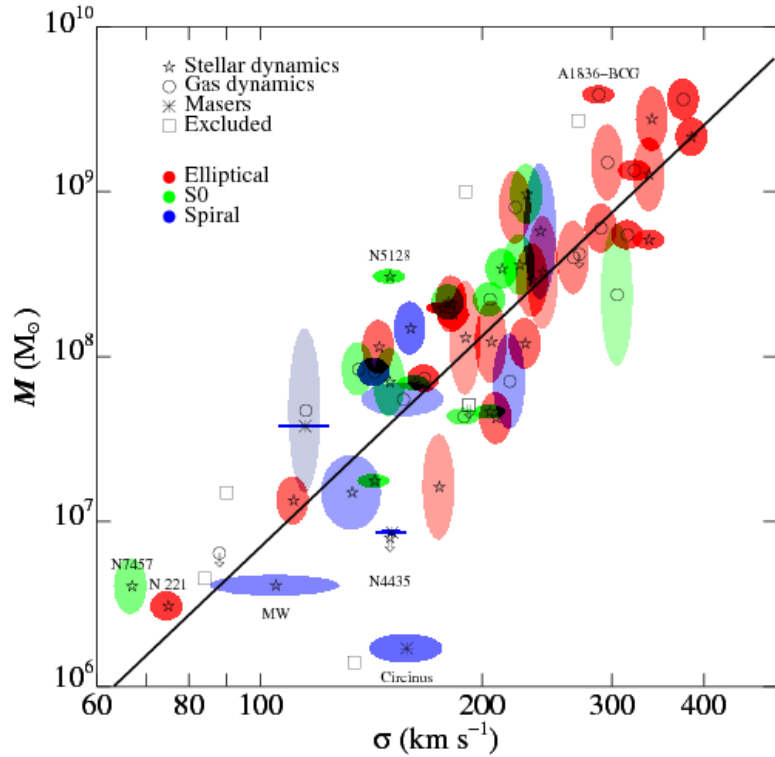


FIGURE 2.1: Credit: Gultekin et al. 2009. The $M_{BH} - \sigma_*$ correlation.

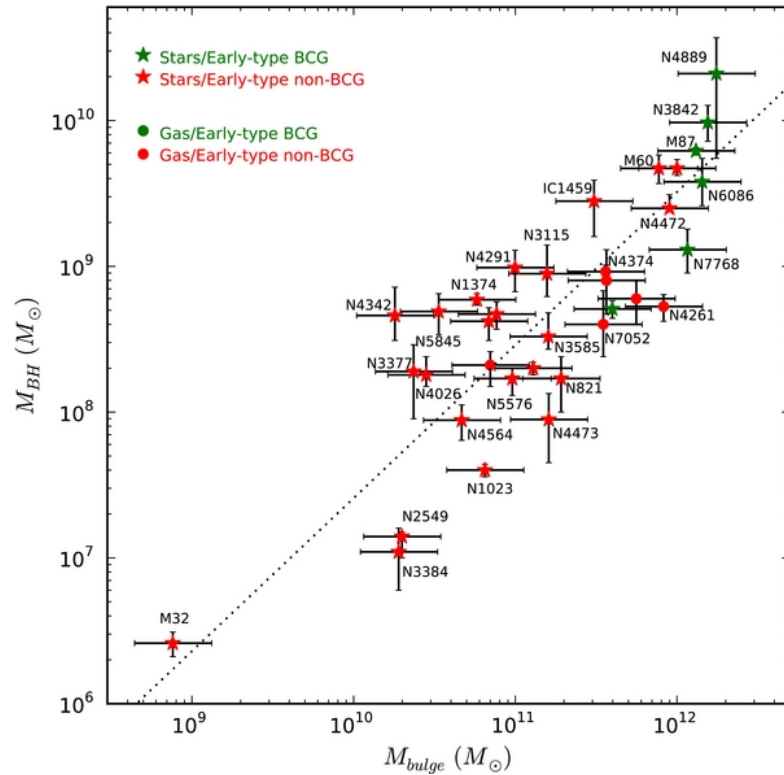


FIGURE 2.2: Credit: McConnell & Ma 2013. The $M_{BH} - M_{bulge}$ correlation.

2.5.2 Radiative or quasar mode feedback

2.5.3 Kinetic or radio mode feedback

2.5.4 In-situ Explanations

Chapter 3

Radiative Transfer and Ionization

“I’m splashing greys where once was
glowing white”

Mike Vennart, Silent/Transparent

In the previous chapters I have given an introduction to the field and some relevant background relating to accretion discs and their associated outflows. Now it proves useful to discuss some of the specific *methods* one might be able to use in order to answer some of the questions raised in the previous sections. In particular, I will discuss radiative transfer techniques and their potential applications.

3.1 Fundamentals of Radiative Transfer

The most fundamental quantity of radiative transfer is the *specific intensity*, I_ν , defined as

$$I_\nu = \frac{dE}{d\Omega dt dA d\nu}, \quad (3.1)$$

which has units of $\text{erg s}^{-1} \text{ Hz}^{-1} \text{ sr}^{-1} \text{ cm}^{-2}$. By successively multiplying by $\cos \theta$ and integrating over solid angle we can obtain the first and second ‘moments’ of the radiation field. These are the flux, F_ν and momentum flux, p_ν , respectively, given by

$$F_\nu = \int I_\nu \cos \theta d\Omega, \quad (3.2)$$

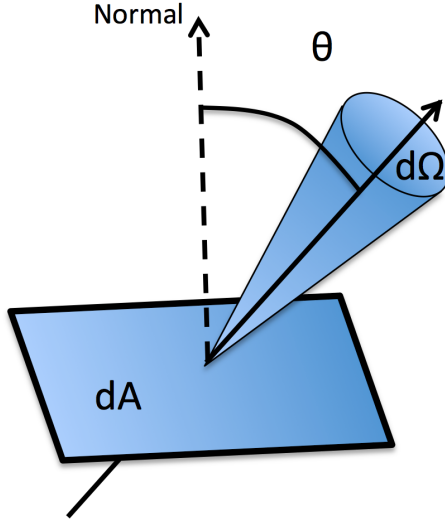


FIGURE 3.1: A schematic showing a ray obliquely incident on a surface of area dA . The labeled quantities are used in the definition of specific intensity.

$$p_\nu = \frac{1}{c} \int I_\nu \cos^2 \theta \, d\Omega \quad (3.3)$$

We can also define the *mean intensity*, J_ν , as

$$J_\nu = \frac{1}{4\pi} \int I_\nu \, d\Omega \quad (3.4)$$

The mean intensity is particularly useful when one wants to ignore the solid angle dependence of the radiation, for example when considering the impact of an ionizing radiation field.

The equation describing the specific intensity change along a path element ds is the radiative transfer equation,

$$\frac{dI_\nu}{ds} = -\kappa_\nu I_\nu + j_\nu, \quad (3.5)$$

where κ_ν and j_ν are the absorption and emission coefficients respectively. If we define the optical depth $d\tau_\nu = \kappa_\nu ds$ we can recast this as

$$\frac{dI_\nu}{d\tau_\nu} = -I_\nu + S_\nu \quad (3.6)$$

where $S_\nu = j_\nu / \kappa_\nu$ is the source function. This equation is called the *formal radiative transfer equation*, and can be solved to give

$$I_\nu = I_{\nu,0} e^{-\tau_\nu} + \int_0^{\tau_\nu} S_\nu(\tau'_\nu) e^{\tau'_\nu - \tau_\nu} d\tau'_\nu. \quad (3.7)$$

A useful limit is when the source function is constant in the absorbing medium, in which case the integral can be easily evaluated to give

$$I_\nu = I_{\nu,0} e^{-\tau_\nu} + S_\nu(1 - e^{-\tau_\nu}). \quad (3.8)$$

3.1.1 Spectral Line Formation

From the above equations, it is trivial to show how emission and absorption lines form when the source function is approximately constant. Say we have a plasma illuminated by a blackbody of temperature T_0 , such that $I_{\nu,0} = B_\nu(T_0)$. The plasma layer then has a different temperature, T , such that $S_\nu = B_\nu(T)$ in that medium. By inspecting equation 3.8 we can see that if we are optically thick within the line, but optically thin in the continuum, then inside the line the source term is dominant and outside the line the first $I_{\nu,0} e^{-\tau_\nu}$ term dominates. Therefore, if $T > T_0$ we will see an emission line, and if $T < T_0$ we will see an absorption line. This approach describes line emission in the blackbody limit; for more complicated SED shapes it is necessary to construct simple model atoms.

3.1.2 The Two Level Atom

The two level atom formalism is well described by Mihalas (1978).

3.1.2.1 Einstein Coefficients

Within the two level atom, the rate equation between the two levels in LTE can be written by invoking detailed balance, such that

$$B_{lu}\bar{J}_{ul}n_l = B_{ul}\bar{J}_{ul}n_u + A_{ul}n_u, \quad (3.9)$$

where B_{ul} , B_{2ul} and A_{ul} are the *Einstein coefficients* for absorption, stimulated emission and spontaneous emission respectively. The ‘mean intensity in the line’, \bar{J}_{ul} , is given by

$$\bar{J}_{ul} = \int \phi(\nu) J_\nu d\nu. \quad (3.10)$$

In LTE, the level populations obey Boltzmann statistics, and thus we can also write

$$\frac{n_l}{n_u} = \frac{g_l}{g_u} \exp(h\nu_{ul}/k_B T) \quad (3.11)$$

We can then rearrange equation 3.9 in terms of the mean intensity, and use the fact that, in LTE, $\bar{J}_{ul} = B_\nu(T)$ to write

$$\bar{J}_{ul} = (2h\nu_{ul}^3)/c^2. \quad (3.12)$$

Since this must be true at all values of T we can also show that

$$A_{ul}/B_{ul} = (2h\nu_{ul}^3) \quad B_{lu}/B_{ul} = g_u/g_l \quad (3.13)$$

3.1.2.2 Collision Strengths

As well as radiative excitation and de-excitation, bound electrons can also interact with the thermal pool of free electrons, meaning that collisional rates also affect

3.1.3 The Sobolev Approximation

The Sobolev approximation (SA) is a useful limit originally developed. It is used to treat line transfer in fast-moving flows. Originally the theory was mostly applied to Stellar winds, although since then a wide variety of astrophysical objects have been modelled using Sobolev treatments, such as accreting systems (this work) and Supernovae.

The Sobolev limit is when the local bulk velocity gradients in a flow dominate other any thermal broadening. In the presence of these steep velocity gradients, one can assume that the interaction of a ray with a bound-bound transition takes place over a small resonant zone, known as a ‘Sobolev surface’. The length of this zone is defined by

$$l_s = \frac{v_{th}}{dv/ds}. \quad (3.14)$$

It is important that the physical conditions of the c do not change on this scale. If this is the case, then we can assume that all line interactions for a given frequency will occur at a single ‘resonant’ point. The location at which a given photon will interact with a line of frequency ν_{lu} is then given, in velocity space, by

$$v = c \left(\frac{\nu}{\nu_{lu}} + 1 \right). \quad (3.15)$$

The Sobolev optical depth is then

$$d\tau = \frac{\pi e^2}{mc} \left(n_l - n_u \frac{g_l}{g_u} \right) \frac{f_{lu} \lambda_{lu}}{c|dv/ds|}. \quad (3.16)$$

We can see that the physical quantities determining line opacity are therefore the level populations in the plasma, the velocity gradient and the atomic physics associated with the bound-bound transition.

3.1.3.1 Escape Probabilities

3.1.4 Monte Carlo approaches

Simple radiation transfer problems can be solved analytically, but with more complicated geometries it is necessary to use Monte Carlo techniques, which are easily solved with modern computing approaches and are intuitively parallelisable problems. I will describe one specific Monte Carlo radiative transfer (MCRT) code, which has been used for the majority of the work in this thesis.

3.2 PYTHON: A Monte Carlo Ionization and Radiative Transfer Code

PYTHON¹ is a Monte Carlo ionization and radiative transfer code. The code has already been described extensively by LK02, SDL05 and Higginbottom et al. (2013; hereafter H13), so here we provide only a brief summary of its operation, focusing particularly on new aspects of our implementation of macro-atoms into the code.

3.2.1 Basics

PYTHON operates in three distinct stages, shown in figure 3.2. First, the user specifies the photon sources, geometry and kinematics of the system, normally with a similar parameterisation to the SV93 model described in section ???. The outflow is then discretised into a logarithmic grid with a user-specified resolution, and the density and velocity in each cell is calculated.

Once the basic setup process has been carried out, the ionization state, level populations and temperature structure are calculated. This is done via an iterative process, by

¹Named c. 1995, predating the inexorable rise of a certain widely used programming language.

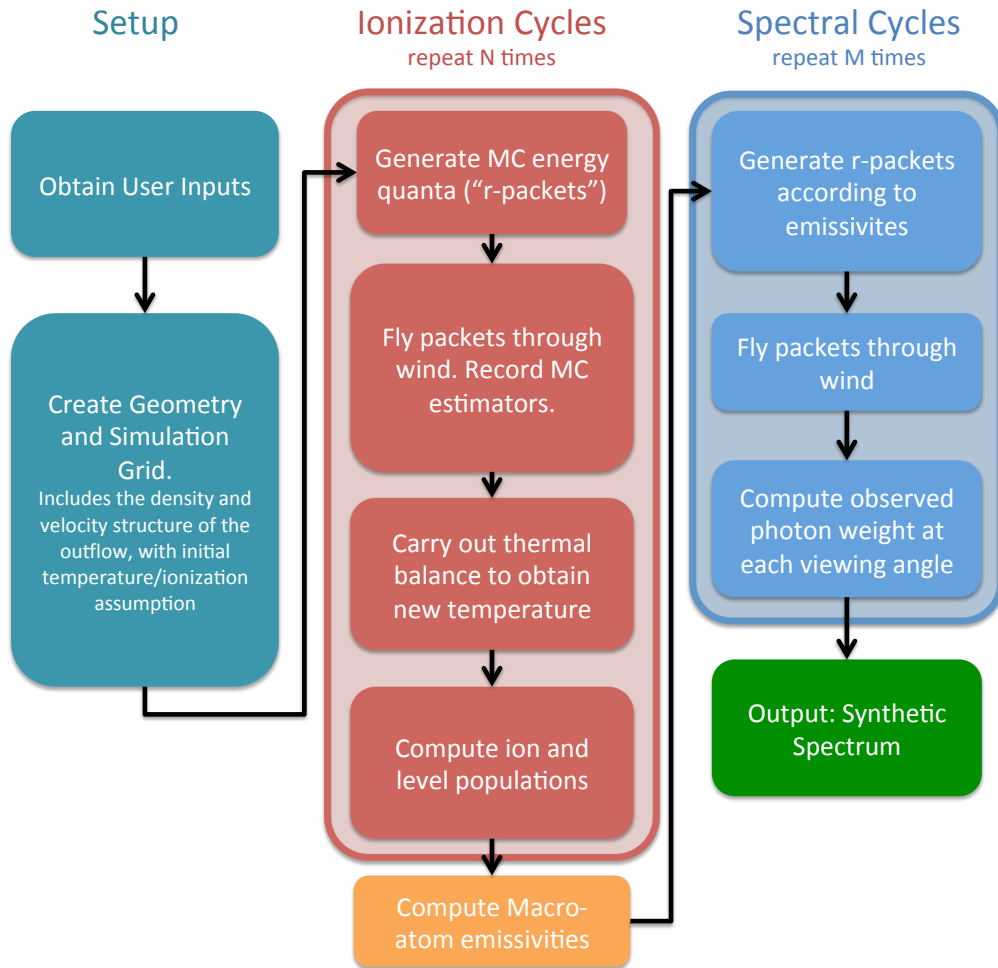


FIGURE 3.2: A flowchart showing the basic operation of PYTHON.

transporting several populations of Monte Carlo energy quanta ('photons' or 'r-packets) through the outflow. This process is repeated until the code converges. In each of these iterations ('ionization cycles'), the code records estimators that characterize the radiation field in each grid cell. At the end of each ionization cycle, a new electron temperature is calculated that more closely balances heating and cooling in the plasma. The radiative estimators and updated electron temperature are then used to revise the ionization state of the wind, and a new ionization cycle is started. The process is repeated until heating and cooling are balanced throughout the wind.

This converged model as the basis for the second set of iterations ('spectral cycles'), in order to compute the synthetic spectrum based on the MC estimators record during the ionization cycles. The emergent spectrum over the desired spectral range is synthesized by tracking populations of energy packets through the wind and computing the emergent spectra at a number of user-specified viewing angles.

PYTHON is designed to operate in a number of different regimes, both in terms of the scale of the system and in terms of the characteristics of the underlying radiation field. It was originally developed by LK02 in order to model the UV spectra of CVs with a simple biconical disc wind model. SDL05 used the code to model Brackett and Pfund line profiles of H in young-stellar objects (YSOs). As part of this effort, they implemented a ‘macro-atom’ mode (see below) in order to correctly treat H recombination lines with PYTHON. Finally, H13 used PYTHON to model broad absorption line (BAL) QSOs. For this application, an improved treatment of ionization was implemented, so that the code is now capable of dealing with arbitrary photo-ionizing SEDs, including non-thermal and multi-component ones.

3.3 Macro-atoms

The macro-atom scheme was created by Leon Lucy and is outlined in his 2002/03 papers. It was implemented in PYTHON by Stuart Sim, initially for the study of recombination lines in YSO (Sim et al. 2005).

Lucy (2002, 2003; hereafter L02, L03) has shown that it is possible to calculate the emissivity of a gas in statistical equilibrium without approximation for problems with large departures from LTE. His macro-atom scheme allows for all possible transition paths from a given level, dispending with the two-level approximation, and provides a full non-local thermodynamic equilibrium (NLTE) solution for the level populations based on Monte Carlo estimators. The macro-atom technique has already been used to model Wolf-Rayet star winds (Sim 2004), AGN disc winds (Sim et al. 2008; Tatum et al. 2012), supernovae (Kromer and Sim 2009; Kerzendorf and Sim 2014) and YSOs (SDL05). A full description of the approach can be found in L02 and L03.

The fundamental approach here requires somewhat of a philosophical shift. Normally MCRT is described in the most intuitive way- that is, we imagine real photons striking atoms and scattering, or photoionizing and depositing energy in a plasma. With Lucy’s scheme one should instead reimagine the MC quanta as a packets of quantised energy flow, and the scheme as a *statistical* one. The amount of time a given energy quanta spends in a specific atomic level or thermal pool is then somewhat analogous to the absolute energy contained therein.

Following L02, let us consider an atomic species interacting with a radiation field. If the quantity ϵ_j represents the ionization plus excitation energy of a level i then the rates at which the level j absorbs and emits radiant energy are given by

$$\dot{A}_j^R = R_{\ell j} \epsilon_{j\ell'} \quad \text{and} \quad \dot{E}_i^R = R_{j\ell'} \epsilon_{j\ell'} \quad , \quad (3.17)$$

Where we adopt Lucy's convention in which the subscript ℓ' denotes a summation over all lower states. Similarly, the rates corresponding to *kinetic* energy transport can then be written as

$$\dot{A}_j^C = C_{\ell' j} \epsilon_{j\ell'} \quad \text{and} \quad \dot{E}_j^C = C_{j\ell'} \epsilon_{j\ell'} \quad , \quad (3.18)$$

If we now impose statistical equilibrium

$$(\mathcal{R}_{\ell' j} - \mathcal{R}_{j\ell}) + (\mathcal{R}_{uj} - \mathcal{R}_{ju}) = 0 \quad . \quad (3.19)$$

we can then obtain

$$\begin{aligned} & \dot{E}_j^R + \dot{E}_j^C + \mathcal{R}_{ju} \epsilon_i + \mathcal{R}_{j\ell} \epsilon_\ell \\ &= \dot{A}_j^R + \dot{A}_j^C + \mathcal{R}_{uj} \epsilon_i + \mathcal{R}_{\ell j} \epsilon_\ell. \end{aligned} \quad (3.20)$$

This equation is the starting point for the macro-atom scheme. It shows that, when assuming only radiative equilibrium, the energy flows through a system depend only on the transition probabilities and atomic physics associated with the levels the energy flow interacts with. By quantising this energy flow into radiant (r-) and kinetic (k-) packets, we can simulate the energy transport through a plasma discretised into volume elements (“macro-atoms”), whose associated transition probabilities govern the interaction of radiant and kinetic energy with the ionization and excitation energy associated with the ions of the plasma.

Although equation 3.20 assumes strict radiative equilibrium, it is trivial to adjust it to include non-radiative source and sink terms. For example, in an expanding parcel of plasma, adiabatic cooling may be included with a simple modification to the RHS of equation 3.20.

3.3.1 Macro-Atom Estimators

3.3.1.1 Radiation Field Estimators

One of the most important estimators is the ‘mean intensity in the line’, \bar{J}_{lu} , which is defined by equation 3.10.

3.3.1.2 Heating And Cooling Estimators

3.3.2 Ionization Fractions and Level Populations

3.4 Simple-atoms

3.5 Heating And Cooling

3.5.1 Heating And Cooling Balance

3.5.2 Heating And Cooling Estimators

Here I’ve tried to use Lucy’s notation for macro-atom estimators. Take a three level system, in which l and u represent lower and upper levels, and κ represents the continuum level or upper ion. q is the ‘absorption fraction’ derived below, and q_{ul} and q_{lu} are the collisional rate coefficients.

3.5.2.1 Macro-atoms

In the macro-atom approach, we basically treat two communication pathways. bound-free transitions represent a way for radiant energy to communicate with the thermal pool and bound-bound transitions represent a way for excitation energy to communicate with the thermal pool.

The heating and cooling rates for macro-atom bound-bound transitions are the rates of collisional excitations and de-excitations - i.e. the rate at which thermal energy is converted into bound-bound excitation energy and vice versa.

$$C_{bb,matoms} = \sum_{lines} q_{lu} n_l n_e h \nu_{ul} V \quad (3.21)$$

$$H_{bb,matoms} = \sum_{lines} q_{ul} n_u n_e h\nu_{ul} V \quad (3.22)$$

For bound-free transitions, we define the normal photoionization and recombination rate coefficients γ and α , where α includes stimulated recombination as we do in the code. Note this differs to the approach in Lucy (2003), where it is instead included as a negative photoionization term, hence the notation $\tilde{\gamma}$. We also need to define two ‘modified rate coefficients’ which are the rates at which b-f transitions add and remove energy to the radiation field. These are denoted γ^E and α^E .

The rate at which recombinations convert thermal *and* ionization energy into radiant energy is then $\alpha^E h\nu_{\kappa l} n_\kappa n_e$, where $h\nu_{\kappa l}$ is the potential of the b-f transition, or the energy difference between continuum κ and the level l we are recombining too. The amount of this energy which is removed from the actual thermal pool therefore needs a quantity $\alpha h\nu_{\kappa l} n_\kappa n_e$ subtracted from it, giving

$$C_{bf,matoms} = \sum_{bfjumps} (\alpha^E - \alpha) n_e n_\kappa \nu_{\kappa l} V \quad (3.23)$$

where here I have also included stimulated recombination as we do in the code. Note this differs to the approach in Lucy (2003), where it is instead included as a negative photoionization term, hence the notation $\tilde{\gamma}$. For photoionizations, we write a similar expression. The rate of at which a level l absorbs energy by b-f transitions is given by $\gamma^E h\nu_{\kappa l} n_\kappa n_e$, but the amount $\gamma h\nu_{\kappa l} n_l$ goes into ionization energy, giving

$$H_{bf,matoms} = \sum_{bfjumps} (\gamma^E - \gamma) n_l h\nu_{\kappa l} V \quad (3.24)$$

as the rate at which radiant energy heats the plasma via b-f transitions.

3.5.2.2 Simple-atoms

In simple-ions it is in some ways a little more complicated. First we define q which will be different for each b-b transition, following Nick’s thesis, which is given by (NB: I don’t actually know how to derive this)

$$q = \frac{q_{ul} n_e (1 - e^{-h\nu/kT_e})}{\beta_{ul} A_{ul} + q_{ul} n_e (1 - e^{-h\nu/kT_e})} \quad (3.25)$$

where β_{ul} is the angle-averaged escape probability. q represents *the probability that an excited bound electron will collisionally de-excite*. Our b-b heating rate is computed during the photon propagation and is a sum over photons which come into resonance

with each line, given by

$$H_{bb, simple} = \sum_{photons\ lines} \sum (1-q)(1-e^{-\tau_s}) w_{photon} \quad (3.26)$$

And our bound bound cooling rate is given by

$$C_{bb, simple} = \sum_{lines} q \left(n_l \frac{g_u}{g_l} - n_u \right) q_{ul} n_e \frac{(1-e^{-h\nu/kT_e})}{(e^{h\nu/kT_e} - 1)} h\nu_{ul} \quad (3.27)$$

The bound-free heating rate is given by

$$H_{bf, simple} = \sum_{photons\ bf\ jumps} \sum w_{photon} e^{-\tau} \frac{\nu - \nu_0}{\nu} \quad (3.28)$$

where ν here is the frequency of the photon in question, and ν_0 . The bound-free cooling rate is then

$$C_{bf, simple} = ?? \quad (3.29)$$

3.6 Spectral Synthesis

The primary output from PYTHON is a synthetic spectrum across a range of viewing angles. The code utilises a variance reduction technique in order to minimise the amount of time spent in the portion of the code. This technique is based on a similar method implemented by ([Woods 1991](#)).

A comparison between the two methods is shown in figure [3.3](#).

3.7 Atomic Data

One of the big challenges in building reliable photoionization and radiative transfer lies in the acquisition of accurate and complete atomic datasets. All of the rates described so far contain a term, such as the oscillator strength or dimensionless collision strength, that is dependent purely on the atomic physics associated with the transition. These quantities can be measured in laboratory experiments, or predicted from atomic structure codes which derive the atomic physics from quantum theory.

Photoionization cross-sections are obtained from two sources. Where possible, we use TOPBASE photoionization cross-sections. For macro-atoms, these cross-sections are

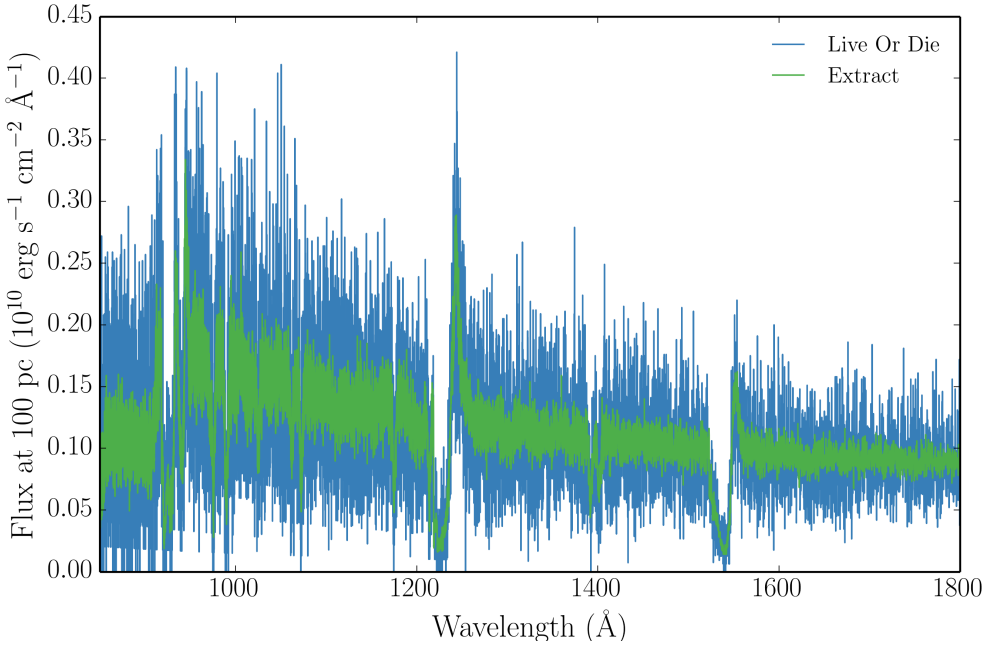


FIGURE 3.3: A Synthetic spectrum after 30 spectral cycles with 100,000 photons from simple CV wind model at a 60° viewing angle. Spectra produced with both the extract and live or die modes are shown. The effectiveness of the extract variance reduction technique can be clearly seen, and we can see that the spectral shape is unaltered.

partial and represent the cross-section for a photoionization from a given *level*. We neglect photoionizations to excited configurations of the upper ion. For simple-atoms they are from the ground state. The TOPBASE cross-sections have two major drawbacks in that

3.8 Clumping

3.8.1 Motivation

As described in section ??, observational evidence for inhomogeneities in outflows is widespread. Clumping a plasma can have a significant effect on its ionization, emission and absorption characteristics. Clearly, the interplay between these effects will be somewhat complex

A number of different implementations of clumping have been explored in previous studies, mostly in the stellar winds community. Perhaps the simplest method is when one assumes that the individual clumps are both optically and geometrically thin; this is known as *microclumping* (e.g. Hamann and Koesterke 1998; Hillier and Miller 1999;

([Hamann et al. 2008](#)). This technique has been particularly successful in reconciling discrepant mass-loss estimates. It was found that one would obtain different mass-loss rates depending on whether they were calculated from (i) UV resonance scattering of continuum photons (which scales linearly with density; a ‘ ρ -diagnostic’) or (ii) recombination and free-free emission process (which scale with the square of density; ‘ ρ^2 -diagnostics’). A clumped outflow would have enhanced densities in certain regions, and would thus mean that ρ^2 -diagnostics tend to overestimate the total mass-loss rates. Microclumping has helped verify this hypothesis with radiative transfer modelling (REFs). These clumpy models also provide better fits to the electron scattering wings of emission lines in stellar winds (?).

The second-generation of stellar wind codes went on step further by addressing the issue of *porosity*; that clumps will have a finite size, and thus gaps between the clumps may affect the emergent radiation field. This approach is known as *macroclumping*.

Describe macroclumping with references.

Implementing a treatment of clumping in accretion disc wind models is challenging, for two main reasons. First, the physical scale lengths and density contrasts in disc winds are not well-constrained from observations, especially in AGN. Second, there are significant computational difficulties associated with adequately resolving and realistically modelling a series of small scale, high density regions with a MCRT code. Given the lack of knowledge about the actual type of clumping, we incorporated the simpler microclumping approach into our code. This is partly because our primary concern was the ionization and emission characteristics of the flow, and porosity was a secondary concern.

3.8.2 Microclumping

To take account of clumping in our outflow we adopt a simple parameterization used in stellar wind modelling. The key assumption here is that typical clump sizes are much smaller than the typical photon mean free path, and thus the clumps are both geometrically and optically thin. This approach is typically known as microclumping and allows one to introduce a ‘filling factor’, f , which is the fraction of the volume of the plasma filled by clumps. We can then introduce the ‘density enhancement’, D , which is simply

$$D = \frac{1}{f} \quad (3.30)$$

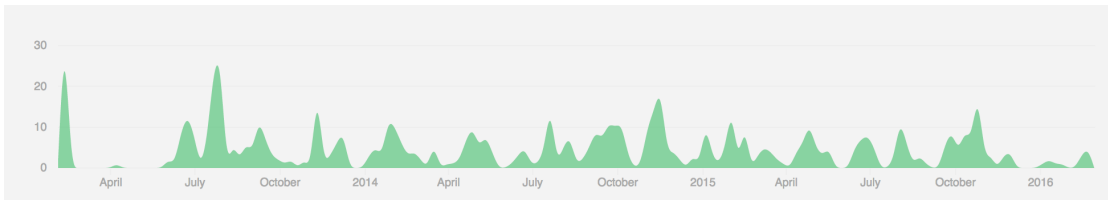


FIGURE 3.4: Commit history from Feb 3, 2013 to Feb 29, 2016, showing the regular code development that makes version control such a necessity to a collaborative code project. Produced using the Github API and plotting capability.

The densities in the model are then multiplied by this factor. This has the effect of enhancing ‘ ρ^2 ’ processes such as recombination or collisional excitation, and

3.9 Code Validation

The main challenge for high performance scientific computing can be elegantly summarised by Ferland’s (2002) epitaph, ‘*Reliability in the face of complexity*’. I have already delved into some of the complexity in this case, so it is important to assess whether the code is also reliable before I present results.

3.9.1 Testing against Cloudy

3.9.2 Testing against Tardis

3.10 Code Maintenance and Version Control

As part of the expansion of the team working on PYTHON I was responsible for bringing the code under the auspices of a robust version control system. Thanks to these efforts, the code is now hosted on GitHub at <https://github.com/agnwinds/python/>. Our team uses a Pull & Fork model for collaborative code development, in which major changes are made in a forked repository before the developer submits a ‘Pull request’ to the main repository. To test the code, we use a combination of Travis CI build tests – run per commit to the upstream repo – and our own test suite which is run every night on a multi-core server.

3.10.1 Parallelisation

Chapter 4

The Impact of Accretion Disc Winds on the Optical Spectra of Cataclysmic Variables

This chapter is based on the publication of the same title, published in MNRAS in August 2015 (Matthews et al. 2015).

4.1 Introduction

It has been known for a long time that winds emanating from the accretion disc are important in shaping the ultraviolet (UV) spectra of high-state CVs ([Heap et al. 1978](#); [Greenstein and Oke 1982](#)). The most spectacular evidence for such outflows are the P-Cygni-like profiles seen in UV resonance lines such as C IV $\lambda 1550$ (see e.g. [Cordova & Mason 1982](#)). Considerable effort has been spent over the years on understanding and modelling these UV features (e.g. [Drew & Verbunt 1985](#); [Mauche & Raymond 1987](#); [Drew 1987](#); [Shlosman & Vitello 1993](#); [hereafter SV93]; [Knigge, Woods & Drew 1995](#); [Knigge & Drew 1997](#); [Knigge et al. 1997](#); [Long & Knigge 2002](#) [hereafter LK02], [Noebauer et al. 2010](#); [Puebla et al. 2011](#)). The basic picture emerging from these efforts is of a slowly accelerating, moderately collimated bipolar outflow that carries away $\simeq 1\% - 10\%$ of the accreting material. State-of-the-art simulations of line formation in this type of disc wind can produce UV line profiles that are remarkably similar to observations.

Much less is known about the effect of these outflows on the optical spectra of high-state CVs. These spectra are typically characterized by H and He emission lines superposed

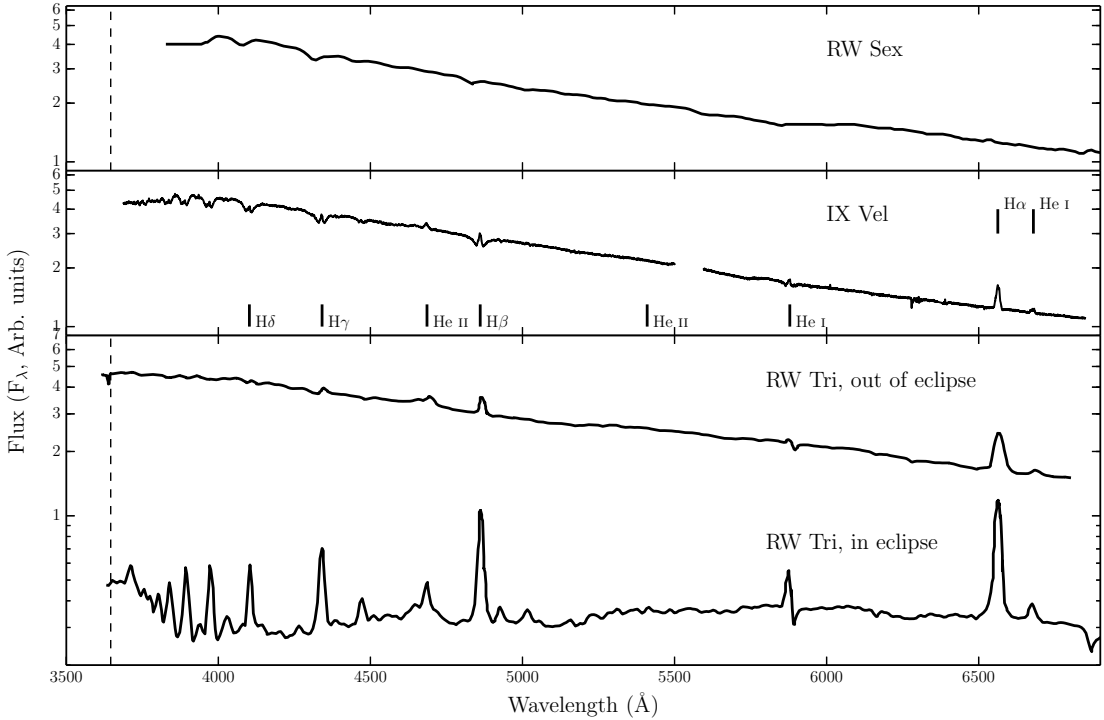


FIGURE 4.1: Optical spectra of three nova-like variables: RW Sex (top; Beuermann et al. 1992), IX Vel (top middle; A. F. Pala & B. T. Gaensicke, private communication) and RW Tri in and out of eclipse (bottom two panels; Groot et al. 2004). The data for RW Sex and RW Tri were digitized from the respective publications, and the IX Vel spectrum was obtained using the XSHOOTER spectrograph on the Very Large Telescope on 2014 October 10. These systems have approximate inclinations of 30° , 60° and 80° (see section 5.4) respectively. The trend of increasing Balmer line emission with inclination can be seen. In RW Tri strong single-peaked emission in the Balmer lines is seen even in eclipse, indicating that the lines may be formed in a spatially extensive disc wind, and there is even a suggestion of a (potentially wind-formed) recombination continuum in the eclipsed spectrum. We have attempted to show each spectrum over a similar dynamic range.

on a blue continuum. In many cases, and particularly in the SW Sex subclass of NLs (Honeycutt et al. 1986; Dhillon and Rutten 1995), these lines are single-peaked. This is contrary to theoretical expectations for lines formed in accretion discs, which are predicted to be double-peaked (Smak 1981; Horne and Marsh 1986). *Low-state* CVs (dwarf novae in quiescence) do, in fact, exhibit such double-peaked lines (Marsh and Horne 1990).

Murray & Chiang (1996, 1997; hereafter referred to collectively as MC96) have shown that the presence of disc winds may offer a natural explanation for the single-peaked optical emission lines in high-state CVs, since they can strongly affect the radiative transfer of line photons. Strong support for a significant wind contribution to the optical emission lines comes from observations of eclipsing systems. There, the single-peaked lines are often only weakly eclipsed, and a significant fraction of the line flux remains visible even near mid-eclipse (e.g. Baptista et al. 2000; Groot et al. 2004). This points to

line formation in a spatially extended region, such as a disc wind (see Fig. 4.1). Further evidence for a wind contribution to the optical lines comes from isolated observations of P-Cygni-like line profiles even in optical lines, such as H α and He I λ 5876 (Patterson et al. 1996; Ringwald and Naylor 1998; Kafka and Honeycutt 2004).

Could disc winds also have an impact on the UV/optical *continuum* of high-state CVs? This continuum is usually thought to be dominated by the accretion disc and modelled by splitting the disc into a set of concentric, optically thick, non-interacting annuli following the standard $T_{eff}(R) \propto R^{-3/4}$ radial temperature distribution (Shakura and Sunyaev 1973). In such models, each annulus is taken to emit either as a blackbody or, perhaps more realistically, as a stellar/disc atmosphere model (Schwarzenberg-Czerny and Rózyczka 1977; Wade 1984, 1988). In the latter case, the local surface gravity, $\log g(R)$, is assumed to be set solely by the accreting WD, since self-gravity is negligible in CV discs.

Attempts to fit the observed spectral energy distributions (SEDs) of high-state CVs with such models have met with mixed success. In particular, the SEDs predicted by most stellar/disc atmosphere models are too blue in the UV (Wade 1988; Long et al. 1991, 1994; Knigge et al. 1998a) and exhibit stronger-than-observed Balmer jumps in absorption (Wade 1984; Haug 1987; La Dous 1989a; Knigge et al. 1998a). One possible explanation for these problems is that these models fail to capture all of the relevant physics. Indeed, it has been argued that a self-consistent treatment can produce better agreement with observational data (e.g. Shaviv et al. 1991; but see also Idan et al. 2010). However, an alternative explanation, suggested by Knigge et al. (1998b; see also Hassall et al. 1985), is that recombination continuum emission from the base of the disc wind might fill in the disc's Balmer absorption edge and flatten the UV spectrum.

Here, we carry out Monte Carlo radiative transfer simulations in order to assess the likely impact of accretion disc winds on the optical spectra of high-state CVs. More specifically, our goal is to test whether disc winds of the type developed to account for the UV resonance lines would also naturally produce significant amounts of optical line and/or continuum emission. In order to achieve this, we have implemented the ‘macro-atom’ approach developed by Lucy (2002, 2003) into the Monte Carlo ionization and radiative transfer code described by LK02 (a process initiated by Sim et al. 2005; hereafter SDL05). With this upgrade, the code is able to deal correctly with processes involving excited levels, such as the recombination emission produced by CV winds.

The remainder of this paper is organized as follows. In Section 2, we briefly describe the code and the newly implemented macro-atom approach. In Section 3, we describe the kinematics and geometry of our disc wind model. In Section 4, we present spectra simulated from the benchmark model employed by LK02, and, in Section 5, we present

a revised model optimized for the optical waveband. In Section 6, we summarize our findings.

4.2 PYTHON: A MONTE CARLO IONIZATION AND RADIATIVE TRANSFER CODE

PYTHON is a Monte Carlo ionization and radiative transfer code which uses the Sobolev approximation to treat line transfer (e.g. Sobolev 1957, 1960; Rybicki and Hummer 1978). The code has already been described extensively by LK02, SDL05 and Higginbottom et al. (2013; hereafter H13), so here we provide only a brief summary of its operation, focusing particularly on new aspects of our implementation of macro-atoms into the code.

4.2.1 Basics

PYTHON operates in two distinct stages. First, the ionization state, level populations and temperature structure are calculated. This is done iteratively, by propagating several populations of Monte Carlo energy quanta ('photons') through a model wind. The geometric and kinematic properties of the outflow are specified on a pre-defined spatial grid. In each of these iterations ('ionization cycles'), the code records estimators that characterize the radiation field in each grid cell. At the end of each ionization cycle, a new electron temperature is calculated that more closely balances heating and cooling in the plasma. The radiative estimators and updated electron temperature are then used to revise the ionization state of the wind, and a new ionization cycle is started. The process is repeated until heating and cooling are balanced throughout the wind.

This converged model is then used as the basis for the second set of iterations ('spectral cycles'). In these, the emergent spectrum over the desired spectral range is synthesized by tracking populations of energy packets through the wind and computing the emergent spectra at a number of user-specified viewing angles.

PYTHON is designed to operate in a number of different regimes, both in terms of the scale of the system and in terms of the characteristics of the underlying radiation field. It was originally developed by LK02 in order to model the UV spectra of CVs with a simple biconical disc wind model. SDL05 used the code to model Brackett and Pfund line profiles of H in young-stellar objects (YSOs). As part of this effort, they implemented a 'macro-atom' mode (see below) in order to correctly treat H recombination lines with PYTHON. Finally, H13 used PYTHON to model broad absorption line (BAL) QSOs. For

this application, an improved treatment of ionization was implemented, so that the code is now capable of dealing with arbitrary photo-ionizing SEDs, including non-thermal and multi-component ones.

4.2.2 Ionization and Excitation: ‘Simple Atoms’

Prior to SDL05, the relative ionization fractions for all atomic species were estimated via the modified Saha equation (Mazzali & Lucy 1993)

$$\frac{n_{j+1}n_e}{n_j} = W[\xi + W(1 - \xi)] \left(\frac{T_e}{T_R}\right)^{1/2} \left(\frac{n_{j+1}n_e}{n_j}\right)_{T_R}^*. \quad (4.1)$$

Here, the ‘starred’ term on the right represents abundances computed with the Saha equation at temperature T_R , but using partition functions from the dilute blackbody approximation. W is an effective dilution factor, ξ is the fraction of recombinations going directly to the ground state, and T_R and T_e are the radiation and electron temperatures, respectively. This simple ionization scheme produces reasonable results when the photoionizing SED can be approximated by a dilute blackbody. This is the case for high-state CVs. (As noted above, an improved, but more complex treatment of ionization that is appropriate for more complex SEDs is described in H13.)

Similarly, the relative excitation fractions within each ionization stage of a given species were estimated via a modified (dilute) Boltzmann equation,

$$\frac{n_{jk}}{n_j} = \frac{Wg_k}{z_j(T_R)} \exp(-E_k/kT_R), \quad (4.2)$$

where n_{jk} is the population of level k in ionic stage j , E_k is the energy difference between level k and the ground state, g_k is the statistical weight of level k and $z_j(T_R)$ is the partition function of ionic stage j .

Finally, PYTHON originally modelled all bound-bound processes as transitions within a simple two-level atom (e.g. Mihalas 1982). This framework was used for the treatment of line transfer and also for the line heating and cooling calculations (see LK02). The approximation works reasonably well for resonance lines, such as C IV $\lambda 1550$, in which the lower level is the ground state. However, it is a poor approximation for many other transitions, particularly those where the upper level is primarily populated from above. Thus an improved method for estimating excited level populations and simulating line transfer is needed in order to model recombination lines and continua.

4.2.3 Ionization and Excitation: Macro-Atoms

Lucy (2002, 2003; hereafter L02, L03) has shown that it is possible to calculate the emissivity of a gas in statistical equilibrium accurately by quantising matter into ‘macro-atoms’, and radiant and kinetic energy into indivisible energy packets (r- and k- packets, respectively). His macro-atom scheme allows for all possible transition paths from a given level and provides a full non-local thermodynamic equilibrium (NLTE) solution for the level populations based on Monte Carlo estimators. The macro-atom technique has already been used to model Wolf-Rayet star winds (Sim 2004), AGN disc winds (Sim et al. 2008; Tatum et al. 2012), supernovae (Kromer and Sim 2009; Kerzendorf and Sim 2014) and YSOs (SDL05). A full description of the approach can be found in L02 and L03.

Briefly, macro-atom NLTE level populations and ionization fractions are calculated by solving the statistical equilibrium equations between each pair of levels. In the framework of the Sobolev escape probability formalism (Rybicki & Hummer 1978; L02; Sim 2004), the bound-bound excitation rate, \mathcal{R}_{lu} , in an ion is given by

$$\mathcal{R}_{lu} = B_{lu} n_l J_{est} + C_{lu} n_l n_e, \quad (4.3)$$

where u and l denote the upper and lower levels, C represents the collisional rate coefficients, and B is the usual Einstein coefficient. J_{est} is the Monte Carlo estimator for the mean intensity impinging on the Sobolev region, weighted by an angle-dependent escape probability, given by (Sim 2004)

$$J_{est} = \frac{c}{4\pi\nu_0 V} \sum_i w_i \frac{1 - e^{-\tau_{s,i}}}{\tau_{s,i}} \frac{1}{(dv/ds)_i}. \quad (4.4)$$

Here w is the photon weight (in luminosity units), ν_0 is the line frequency, dv/ds is the velocity gradient and τ_s is the Sobolev optical depth. The sum is over all photons that come into resonance with the line, and thus represents an integral over solid angle. The corresponding de-excitation rate is then

$$\mathcal{R}_{ul} = \beta_{lu} A_{ul} n_u + B_{ul} n_u J_{est} + C_{ul} n_u n_e, \quad (4.5)$$

where A is the usual Einstein coefficient. The quantity β_{lu} is the *angle-averaged* probability that a given line photon will escape the Sobolev region.

In our implementation of the macro-atom approach, we also explicitly take into account the photoionization and collisional ionization rates between a lower level, l , and the continuum (or, in the case of ions with more than one bound electron, the ground state

of the upper ion), κ ,

$$\mathcal{R}_{l\kappa} = n_l \int_{\nu_0}^{\infty} \frac{4\pi J_{\nu} \sigma_{\nu}}{h\nu} d\nu + C_{l\kappa} n_l n_e. \quad (4.6)$$

Here, σ_{ν} is the photoionization cross section, and J_{ν} is the mean intensity. The corresponding recombination rate is given by

$$\mathcal{R}_{\kappa l} = \alpha_{\kappa l} n_{\kappa} n_e + C_{\kappa l} n_{\kappa} n_e, \quad (4.7)$$

where $\alpha_{\kappa l}$ is the radiative recombination coefficient to level l . This treatment means that radiative and collisional rates to and from all levels are considered when calculating both the ionization state and the level populations, although we neglect ionization directly to excited levels of the upper ion. The [van Regemorter \(1962\)](#) approximation is used for collisional transitions. This means that collisions between radiatively forbidden transitions are not taken into account when one splits levels into l - and s -subshells, as well as principal quantum number, n (as we have done with He I; see section 4.2.5). Although this approximation is, in general, a poor one, the effect is second order in the physical regime where recombination lines are formed in our models. This is because bound-free processes are dominant in determining level populations and emissivities. We have verified that this is indeed the case in the He I emission regions in our models.

4.2.4 Ionization and Excitation: A Hybrid Approach

SDL05 implemented a macro-atom treatment of H in PYTHON and used this to predict the observable properties of a pure H wind model for YSOs. Our goal here is to simultaneously model the optical and ultraviolet spectra of high-state CVs. Since the optical spectra are dominated by H and He recombination lines, both of these species need to be treated as macro-atoms. The UV spectra, on the other hand, are dominated by resonance lines associated with metals. This means we need to include these species in our models, but they can be treated with our (much faster) simple-atom approach. We have therefore implemented a hybrid ionization and excitation scheme into PYTHON. Any atomic species can now be treated either in our simple-atom approximation or with the full macro-atom machinery. In our CV models, we treat H and He as macro-atoms and all metals as simple-atoms. Species treated with either method are fully taken into account as sources of both bound-free opacity and line opacity, and contribute to the heating and cooling balance of the plasma.

4.2.5 Atomic Data

We generally use the same atomic data as H13, which is an updated version of that described by LK02. In addition, we follow SDL05 in treating H as a 20-level atom, where each level is defined by the principal quantum number, n . For the macro-atom treatment of He, we have added the additional level and line information required from TOPBASE ([Badnell et al. 2005](#)). He II is treated in much the same way as H, but with 10 levels. He I has larger energy differentials between different l-subshells and triplet and singlet states. Thus, we still include levels up to $n = 10$, but explicitly treat the l and s sub-orbitals as distinct levels instead of assuming they are perfectly ‘l-mixed’. This allows us to model the singlet and triplet He I lines that are ubiquitous in the optical spectra of CVs (e.g. [Dhillon 1996](#)).

4.2.6 Code Validation and Testing

PYTHON has been tested against a number of radiative transfer and photoionization codes. LK02 and H13 conducted comparisons of ionization balance with CLOUDY ([Ferland et al. 2013](#)), demonstrating excellent agreement. We have also carried out comparisons of ionization and spectral synthesis with the supernova code TARDIS. TARDIS is described by [Kerzendorf and Sim \(2014\)](#), and the spectral comparisons can be found therein. For the effort reported here, we have additionally carried out tests of the macro-atom scheme in PYTHON. Fig. 4.2 shows two of these tests. In the top panel, we compare the Balmer series emissivities as predicted by PYTHON in the l-mixed Case B limit against the analytical calculations by [Seaton \(1959\)](#). In the bottom panel, we compare PYTHON and TARDIS predictions of He I level populations for a particular test case. Agreement is excellent for both H and He.

4.3 Describing the System and its Outflow

PYTHON includes several different kinematic models of accretion disc winds, as well as different options for describing the physical and radiative properties of the wind-driving system under consideration. Most of these features have already been discussed by LK02 and H13, so below we only briefly recount the key aspects of the particular system and wind model used in the present study.

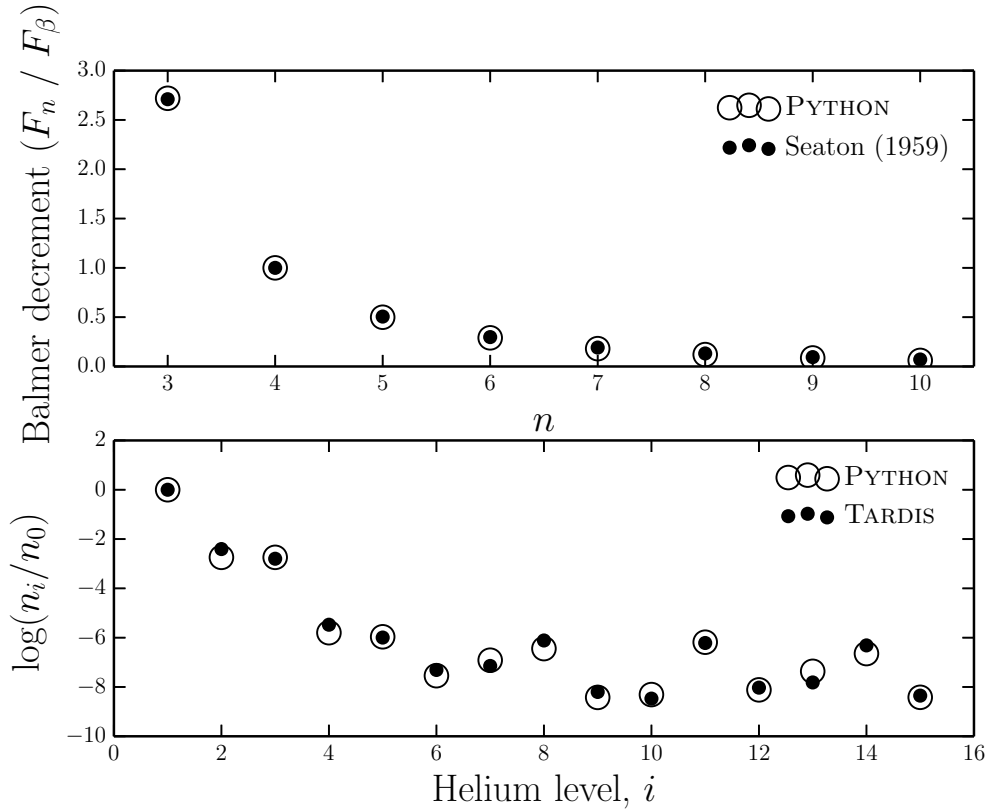


FIGURE 4.2: *Top Panel:* ‘Case B’ Balmer decrements computed with PYTHON compared to analytic calculations by Seaton (1959). Both calculations are calculated at $T_e = 10,000\text{K}$. (see Osterbrock 1989 for a discussion of this commonly used approximation). *Bottom Panel:* a comparison of He I level populations (the most complex ion we currently treat as a macro-atom) between PYTHON and TARDIS models. The calculation is conducted with physical parameters of $n_e = 5.96 \times 10^4 \text{ cm}^{-3}$, $T_e = 30,600\text{K}$, $T_R = 43,482\text{K}$ and $W = 9.65 \times 10^{-5}$. Considering the two codes use different atomic data and TARDIS, unlike PYTHON, currently has a complete treatment of collisions between radiatively forbidden transitions, the factor of < 2 agreement is encouraging.

4.3.1 Wind Geometry and Kinematics

We adopt the kinematic disc wind model developed by SV93. A schematic of this model is shown in Fig. 4.3. In this parametrization, a smooth, biconical disc wind emanates from the accretion disc between radii r_{min} and r_{max} . The covering fraction of the outflow is also controlled by the inner and outer opening angles of the wind, θ_{min} and θ_{max} , and the launch angle of the other streamlines is given by

$$\theta(r_0) = \theta_{min} + (\theta_{max} - \theta_{min}) \left(\frac{r_0 - r_{min}}{r_{max} - r_{min}} \right)^\gamma, \quad (4.8)$$

where r_0 is the launch radius of the streamline.

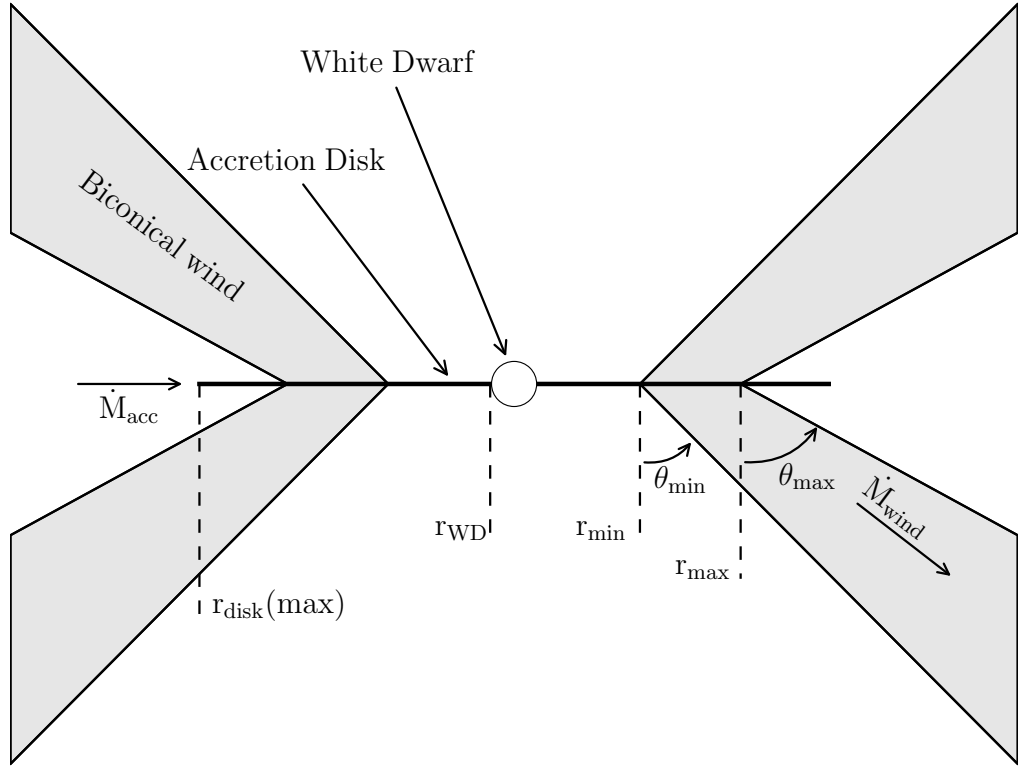


FIGURE 4.3: Cartoon illustrating the geometry and kinematics of the benchmark CV wind model.

The poloidal (non-rotational) velocity field of the wind, v_l , is given by

$$v_l = v_0 + [v_\infty(r_0) - v_0] \frac{(l/R_v)^\alpha}{(l/R_v)^\alpha + 1}, \quad (4.9)$$

where l is the poloidal distance along a particular wind streamline. The terminal velocity along a streamline, v_∞ , is set to a fixed multiple of v_{esc} , the escape velocity at the launch point. The launch velocity from the disc surface, v_0 , is assumed to be constant (set to 6 km s^{-1}). Once the wind is launched, it accelerates, reaching half of its terminal velocity at $l = R_v$. The velocity law exponent α controls how quickly the wind accelerates. Larger values of α cause the main region of acceleration to occur close to R_v , whereas smaller values correspond to fast acceleration close to the disc (see Fig. 4.4). The rotational velocity v_ϕ is Keplerian at the base of the streamline and we assume conservation of specific angular momentum, such that

$$v_\phi r = v_k r_0, \quad (4.10)$$

where $v_k = (GM_{WD}/r_0)^{1/2}$.

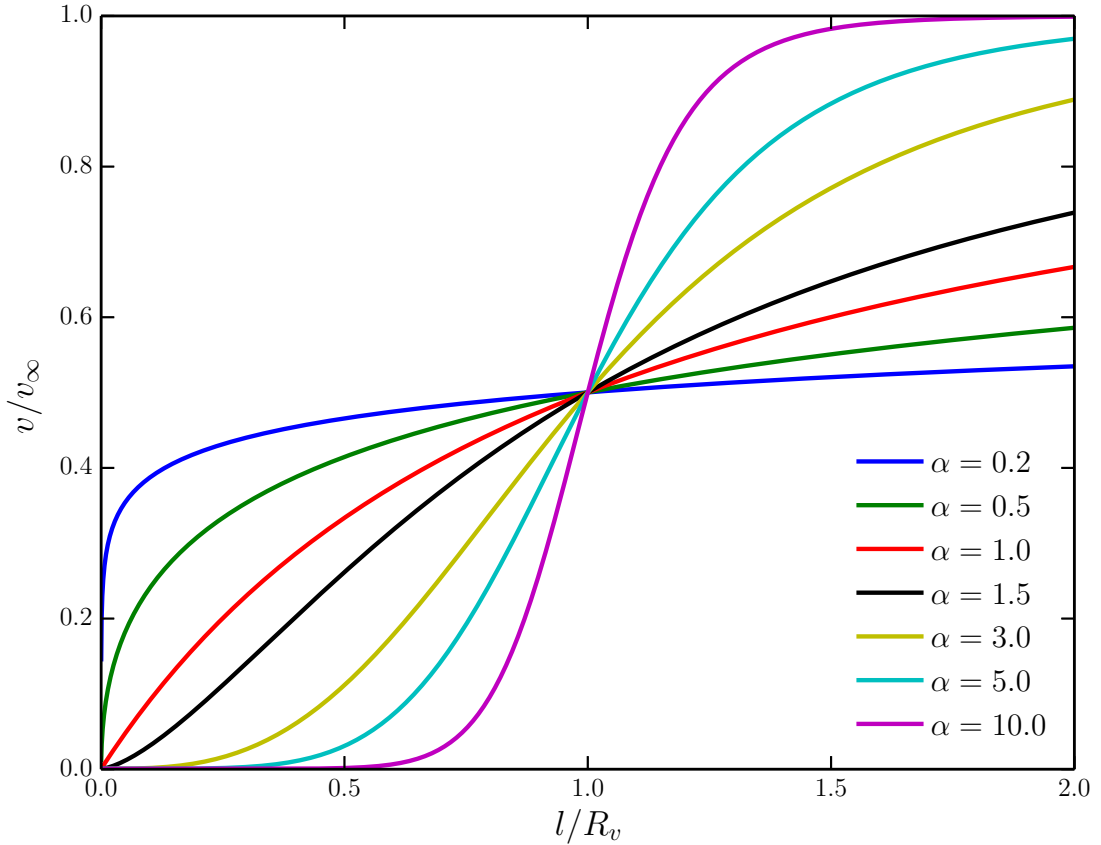


FIGURE 4.4: The adopted poloidal velocity law for various values of the acceleration exponent, α .

The density at position (r, z) in the wind, $\rho(r, z)$, is calculated from the mass continuity equation, yielding

$$\rho(r, z) = \frac{r_0}{r} \frac{dr_0}{dr} \frac{\phi(r_0)}{v_z(r, z)}. \quad (4.11)$$

Here, v_z is the vertical velocity component and, following SV93, $\phi(r_0)$ is the local mass-loss rate per unit area at r_0 , defined as

$$\phi(r_0) \propto \dot{M}_{wind} r_0^\lambda \cos[\theta(r_0)]. \quad (4.12)$$

We adopt $\lambda = 0$ and normalize $\phi(r_0)$ by matching its integral over both sides of the disc to the user-specified total mass-loss rate, \dot{M}_{wind} .

4.3.2 Sources and Sinks of Radiation

The net photon sources in our CV model are the accretion disc, the WD and, in principle, a boundary layer with user-defined temperature and luminosity. All of these radiating bodies are taken to be optically thick, and photons striking them are assumed to be destroyed instantaneously. The secondary star is not included as a radiation source, but

is included as an occulting body. This allows us to model eclipses. Finally, emission from the wind itself is also accounted for, but note that we assume the outflow to be in radiative equilibrium. Thus all of the heating of the wind, as well as its emission, is ultimately powered by the radiation field of the net photon sources in the simulation. In the following sections, we will describe our treatment of these system components in slightly more detail.

4.3.2.1 Accretion disc

PYTHON has some flexibility when treating the accretion disc as a source of photons. The disc is broken down into annuli such that each annulus contributes an equal amount to the bolometric luminosity. We take the disc to be geometrically thin, but optically thick, and thus adopt the temperature profile of a standard [Shakura and Sunyaev \(1973\)](#) α -disc. An annulus can then be treated either as a blackbody with the corresponding effective temperature or as a stellar atmosphere model with the appropriate surface gravity and effective temperature. Here, we use blackbodies during the ionization cycles and to compute our Monte Carlo estimators. However, during the spectral synthesis stage of the simulation we use stellar atmosphere models. This produces more realistic model spectra and allows us to test if recombination emission from the wind base can fill in the Balmer jump, which is always in absorption in these models. Our synthetic stellar atmosphere spectra are calculated with SYNSPEC¹ from either Kurucz ([Kurucz 1991](#)) atmospheres (for $T_{eff} \leq 50,000$ K) or from TLUSTY ([Hubeny and Lanz 1995](#)) models (for $T_{eff} > 50,000$ K).

4.3.2.2 White Dwarf

The WD at the center of the disc is always present as a spherical occulting body with radius R_{WD} in PYTHON CV models, but it can also be included as a source of radiation. In the models presented here, we treat the WD as a blackbody radiator with temperature T_{WD} and luminosity $L_{WD} = 4\pi R_{WD}^2 \sigma T_{WD}^4$.

4.3.2.3 Boundary Layer

It is possible to include radiation from a boundary layer (BL) between the disc and the WD. In PYTHON, the BL is described as a blackbody with a user-specified effective temperature and luminosity. In the models presented here, we have followed LK02 in setting the BL luminosity to zero. However, we have confirmed that the addition of an

¹<http://nova.astro.umd.edu/Synspec43/synspec.html>

Parameter	Model Parameters	
	Model A	Model B
M_{WD}	$0.8 M_{\odot}$	
R_{WD}	7×10^8 cm	
T_{WD}	40,000 K	
M_2	-	$0.6 M_{\odot}$
q	-	0.75
P_{orb}	-	5.57 hr
a	-	$194.4 R_{WD}$
R_2	-	$69.0 R_{WD}$
\dot{M}_{acc}	$10^{-8} M_{\odot} yr^{-1}$	
\dot{M}_{wind}	$10^{-9} M_{\odot} yr^{-1}$	
r_{min}	$4 R_{WD}$	
r_{max}	$12 R_{WD}$	
$r_{disc}(\text{max})$	$34.3 R_{WD}$	
θ_{min}	20.0°	
θ_{max}	65.0°	
γ	1	
v_{∞}	$3 v_{esc}$	
R_v	$100 R_{WD}$	$142.9 R_{WD}$
α	1.5	4

TABLE 4.1: Parameters used for the geometry and kinematics of the benchmark CV model (model A), which is optimized for the UV band, and a model which is optimized for the optical band and described in section 5 (model B). For model B, only parameters which are altered are given - otherwise the model A parameter is used. P_{orb} is the orbital period (the value for RW Tri from Walker 1963 is adopted, see section 5.4) and R_2 is the radius of a sphere with the volume of the secondary's Roche lobe. Other quantities are defined in the text or Fig. 4.3. Secondary star parameters are only quoted for model B as we do not show eclipses with the benchmark model (see section 5.4).

isotropic BL with $L_{BL} = 0.5L_{acc}$ and temperatures in the range $80 \text{ kK} \leq T_{BL} \leq 200 \text{ kK}$ would not change any of our main conclusions.

4.3.2.4 Secondary Star

The donor star is included in the system as a pure radiation sink, i.e. it does not emit photons, but absorbs any photons that strike its surface. The secondary is assumed to be Roche-lobe filling, so its shape and relative size are defined by setting the mass ratio of the system, $q = M_2/M_{WD}$. The inclusion of the donor star as an occulting body allows us to model eclipses of the disc and the wind. For this purpose, we assume a circular orbit with a semi-major axis a and specify orbital phase such that $\Phi_{orb} = 0$ is the inferior conjunction of the secondary (i.e. mid-eclipse for $i \simeq 90^\circ$).

4.4 A Benchmark disc Wind Model

Our main goal is to test whether the type of disc wind model that has been successful in explaining the UV spectra of CVs could also have a significant impact on the optical continuum and emission line spectra of these systems. In order to set a benchmark, we therefore begin by investigating one of the fiducial CV wind models that was used by SV93 and LK02 to simulate the UV spectrum of a typical high-state system. The specific parameters for this model (model A) are listed in Table 1. A key point is that the wind mass-loss rate in this model is set to 10% of the accretion rate through the disc. We follow SV93 in setting the inner edge of the wind (r_{min}) to $4 R_{WD}$. The sensitivity to some of these parameters is briefly discussed in section 5.

4.4.1 Physical Structure and Ionization State

Fig. 4.5 shows the physical and ionization structure of the benchmark disc wind model. The ionization parameter shown in the bottom right panel is given by

$$U = \frac{4\pi}{n_H c} \int_{13.6\text{eV}}^{\infty} \frac{J_{\nu} d\nu}{h\nu}, \quad (4.13)$$

where n_H is the local number density of H, and ν denotes photon frequency. The ionization parameter is a useful measure of the ionization state of a plasma, as it evaluates the ratio of the number density of ionizing photons to the local H density.

There is an obvious drop-off in density and temperature with distance away from the disc, so any line formation process that scales as ρ^2 – i.e. recombination and collisionally excited emission – should be expected to operate primarily in the dense base of the outflow. Moreover, a comparison of the rotational and poloidal velocity fields shows that rotation dominates in the near-disc regime, while outflow dominates further out in the wind.

The ionization equation used in the ‘simple atom’ approach used by LK02 (see section 4.2.2) should be a reasonable approximation to the photoionization equilibrium in the benchmark wind model. Even though the macro-atom treatment of H and He does affect the computation of the overall ionization equilibrium, we would expect the resulting ionization state of the wind to be quite similar to that found by LK02. The bottom panels in Fig. 4.5 confirm that this is the case. In particular, He is fully ionized throughout most of the outflow, except for a small region near the base of the wind, which is shielded from the photons produced by the hot inner disc. In line with the results of LK02, we also find that CIV is the dominant C ion throughout the wind, resulting in

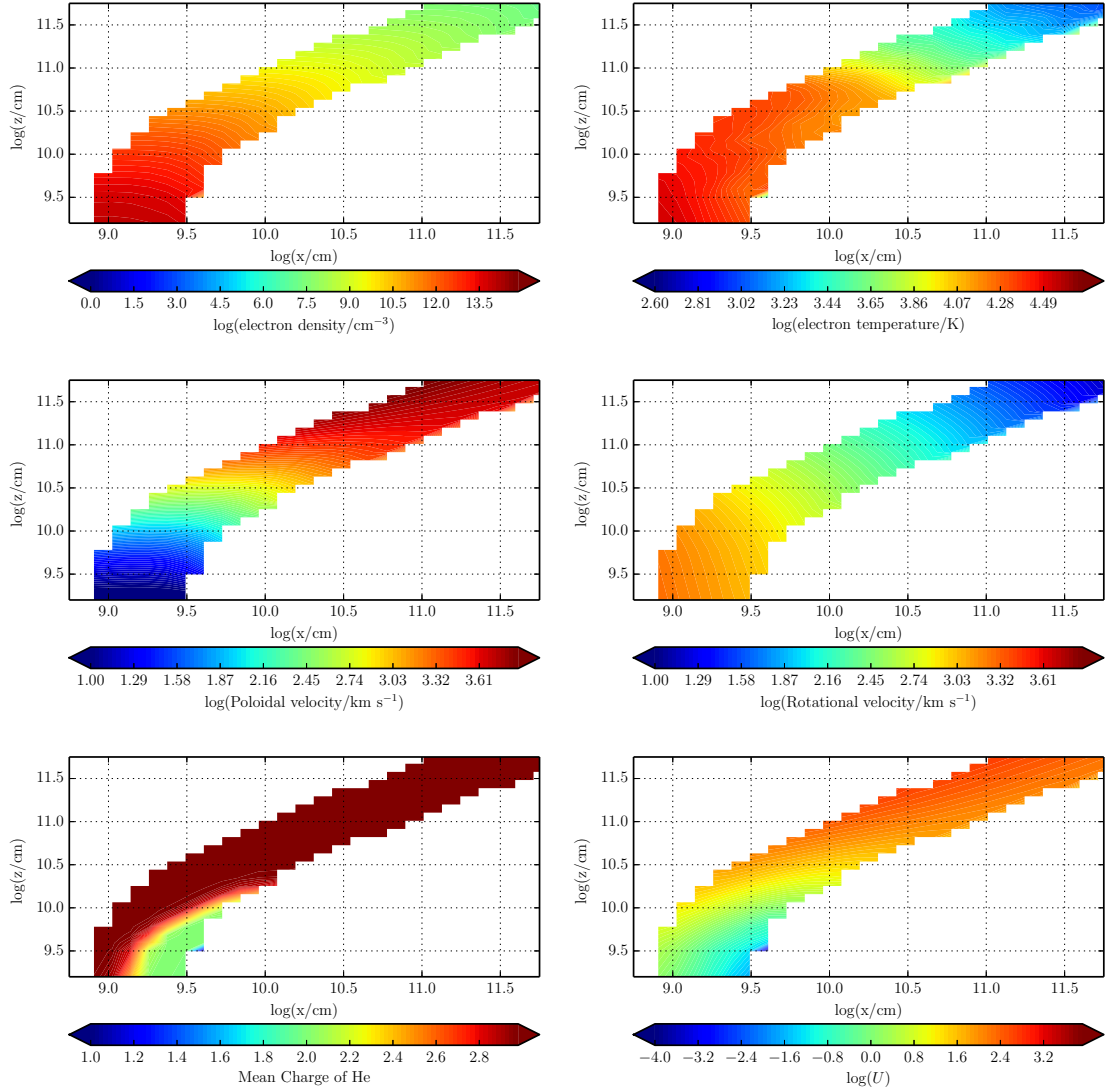


FIGURE 4.5: The physical properties of the wind – note the logarithmic scale. Near the disc plane the wind is dense, with low poloidal velocities. As the wind accelerates it becomes less dense and more highly ionized. The dominant He ion is almost always He III, apart from in a small portion of the wind at the base, which is partially shielded from the inner disc.

a substantial absorbing column across a large range of velocities. As we shall see, this produces the broad, deep and blue-shifted CIV $\lambda 1550$ absorption line that is usually the most prominent wind-formed feature in the UV spectra of low-inclination nova-like CVs.

4.4.2 Synthetic Spectra

We begin by verifying that the benchmark model still produces UV spectra that resemble those observed in CVs. We do expect this to be the case, since the ionization state of the wind has not changed significantly from that computed by LK02 (see section 4.4.1). The left column of panels in Fig. 4.6 shows that this expectation is met: all of the strong

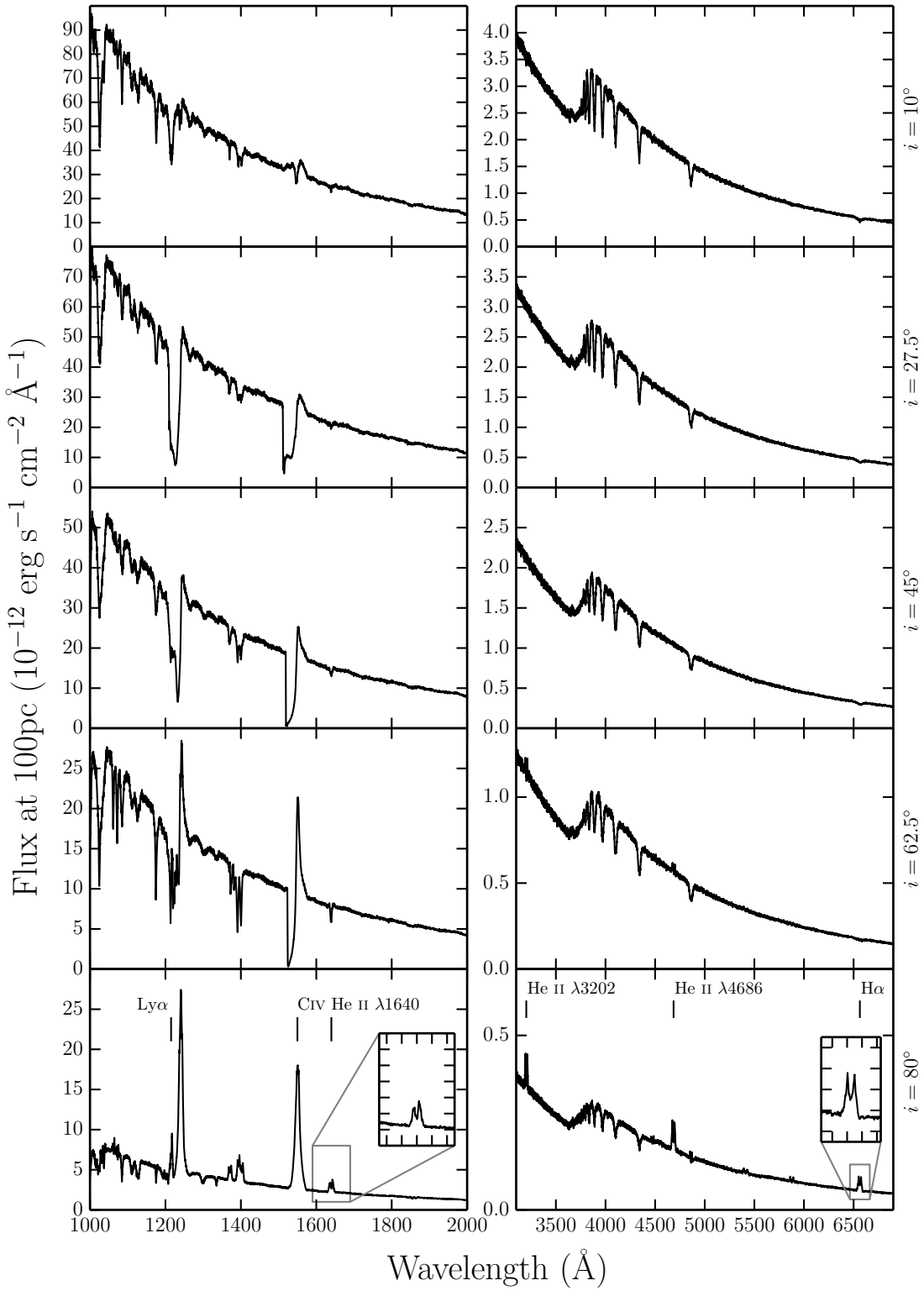


FIGURE 4.6: UV (left) and optical (right) synthetic spectra for model A, our benchmark model, computed at sightlines of 10, 27.5, 45, 62.5 and 80 degrees. The inset plots show zoomed-in line profiles for He II $\lambda 1640$ and H α . Double-peaked line emission can be seen in He II $\lambda 1640$, He II $\lambda 4686$, H α and some He I lines, but the line emission is not always sufficient to overcome the absorption cores from the stellar atmosphere models.

The model also produces a prominent He II $\lambda 3202$ line at high inclinations.

metal resonance lines – notably N V λ 1240, Si IV λ 1400 and C IV λ 1550 – are present and exhibit clear P-Cygni profiles at intermediate inclinations. In addition, however, we now also find that the wind produces significant Ly α and He II λ 1640 emission lines.

Fig. 4.6 (right-hand panel) and Fig. 4.7 show the corresponding optical spectra produced for the benchmark model, and these do exhibit some emission lines associated with H and He. We see a general trend from absorption lines to emission lines with increasing inclination, as one might expect from our wind geometry. This trend is consistent with observations, as can be seen in Fig. 1. However, it is clear that this particular model does not produce all of the lines seen in observations of high-state CVs. The higher-order Balmer series lines are too weak to overcome the intrinsic absorption from the disc atmosphere, and the wind fails to produce any observable emission at low and intermediate inclinations. This contrasts with the fact that emission lines are seen in the optical spectra of (for example) V3885 Sgr (Hartley et al. 2005) and IX Vel (Beuermann and Thomas 1990, see also Fig. 1).

The emissivity of these recombination features scales as ρ^2 , meaning that they form almost entirely in the dense base of the wind, just above the accretion disc. Here, the velocity field of the wind is still dominated by rotation, rather than outflow, which accounts for the double-peaked shape of the lines. In principle, lines formed in this region can still be single peaked, since the existence of a poloidal velocity *gradient* changes the local escape probabilities (MC96). However, as discussed further in section 5.3, the radial velocity shear in our models is not high enough for this radiative transfer effect to dominate the line shapes.

The Balmer jump is in absorption at all inclinations for our benchmark model. This is due to the stellar atmospheres we have used to model the disc spectrum; it is not a result of photoabsorption in the wind. In fact, the wind spectrum exhibits the Balmer jump in *emission*, but this is not strong enough to overcome the intrinsic absorption edge in the disc spectrum. This is illustrated in Fig. 4.8, which shows the angle-integrated spectrum of the system, i.e. the spectrum formed by all escaping photons, separated into the disc and wind contributions. Even though the wind-formed Balmer recombination continuum does not completely fill in the Balmer absorption edge in this model, it does already contribute significantly to the total spectrum. This suggests that modest changes to the outflow kinematics might boost the wind continuum and produce emergent spectra with weak or absent Balmer absorption edges.

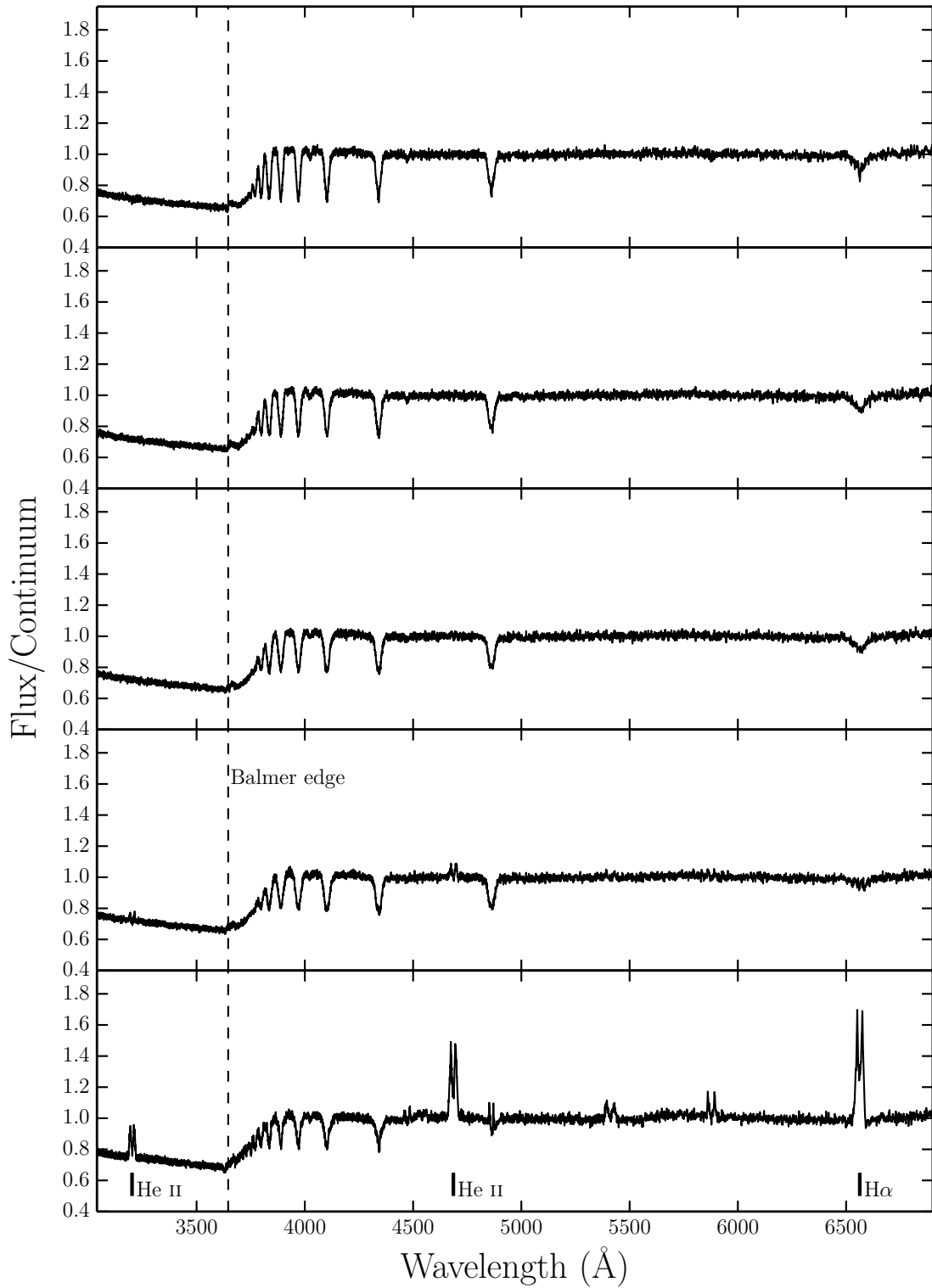


FIGURE 4.7: Synthetic optical spectra from model A computed for sightlines of 10, 27.5, 45, 62.5 and 80 degrees. In these plots the flux is divided by a polynomial fit to the underlying continuum redward of the Balmer edge, so that line-to-continuum ratios and the true depth of the Balmer jump can be shown.

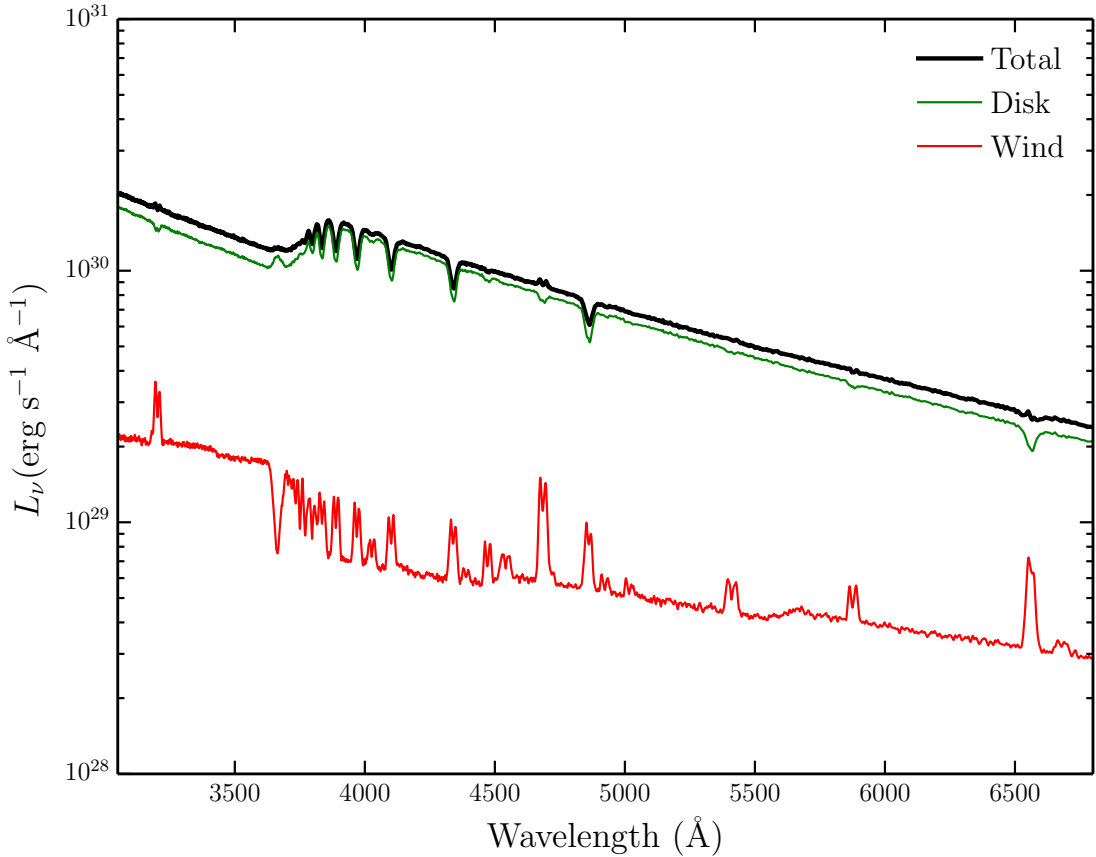


FIGURE 4.8: Total packet-binned spectra across all viewing angles, in units of monochromatic luminosity. The thick black line shows the total integrated escaping spectrum, while the green line shows disc photons which escape without being reprocessed by the wind. The red line show the contributions from reprocessed photons. Recombination continuum emission blueward of the Balmer edge is already prominent relative to other wind continuum processes, but is not sufficient to fill in the Balmer jump in this specific model

4.5 A Revised Model Optimized for Optical Wavelengths

The benchmark model discussed in section 4.4 was originally designed to reproduce the wind-formed lines seen in the UV spectra of high-state CVs. As we have seen, this model does produce some observable optical emission. We can now attempt to construct a model that more closely matches the observed optical spectra of CVs.

Specifically, we aim to assess whether a revised model can:

- account for all of the lines we see in optical spectra of CVs while preserving the UV behaviour;
- produce single-peaked Balmer emission lines;

- generate enough of a wind-formed recombination continuum to completely fill in the disc's Balmer absorption edge for reasonable outflow parameters.

The emission measure of a plasma is directly proportional to its density. The simplest way to simultaneously affect the density in the wind (for fixed mass-loss rate), as well as the velocity gradients, is by modifying the poloidal velocity law. Therefore, we focus on just two kinematic variables (section 4.3.1):

- the acceleration length, R_v , which controls the distance over which the wind accelerates to $\frac{1}{2} v_\infty$;
- the acceleration exponent, α , which controls the rate at which the poloidal velocity changes near R_v .

The general behaviour we might expect is that outflows with denser regions near the wind base – i.e. winds with larger R_v and/or larger α – will produce stronger optical emission signatures. However, this behaviour may be moderated by the effect of the increasing optical depth through this region, which can also affect the line profile shapes. In addition, modifying R_v also increases the emission *volume*. Based on a preliminary exploration of models with different kinematics, we adopt the parameters listed in table 4.1 for our ‘optically optimized’ model (model B).

4.5.1 Synthetic Spectra

Fig. 4.9 shows the UV and optical spectra for the optically optimized model for the full range of inclinations. As expected, the trend from absorption to emission in the optical is again present, but in this revised model we produce emission lines in the entire Balmer series at high inclinations, as well as the observed lines in He II and He I. This can be seen more clearly in the continuum-normalized spectrum in Fig. 4.10.

Two other features are worth noting in the optical spectrum. First, the collisionally excited Ca II emission line at 3934 Å becomes quite prominent in our densest models. Second, our model predicts a detectable He II recombination line at 3202 Å. This is the He equivalent of Paschen β and should be expected in all systems that feature a strong He II $\lambda 4686$ line (the He equivalent of Paschen α). This line is somewhat unfamiliar observationally, because it lies bluewards of the atmospheric cut-off, but also redwards of most ultraviolet spectra.

Our models do not exhibit P-Cygni profiles in the optical lines. This is perhaps not surprising. LK02 and SV93 originally designed such models to reproduce the UV line

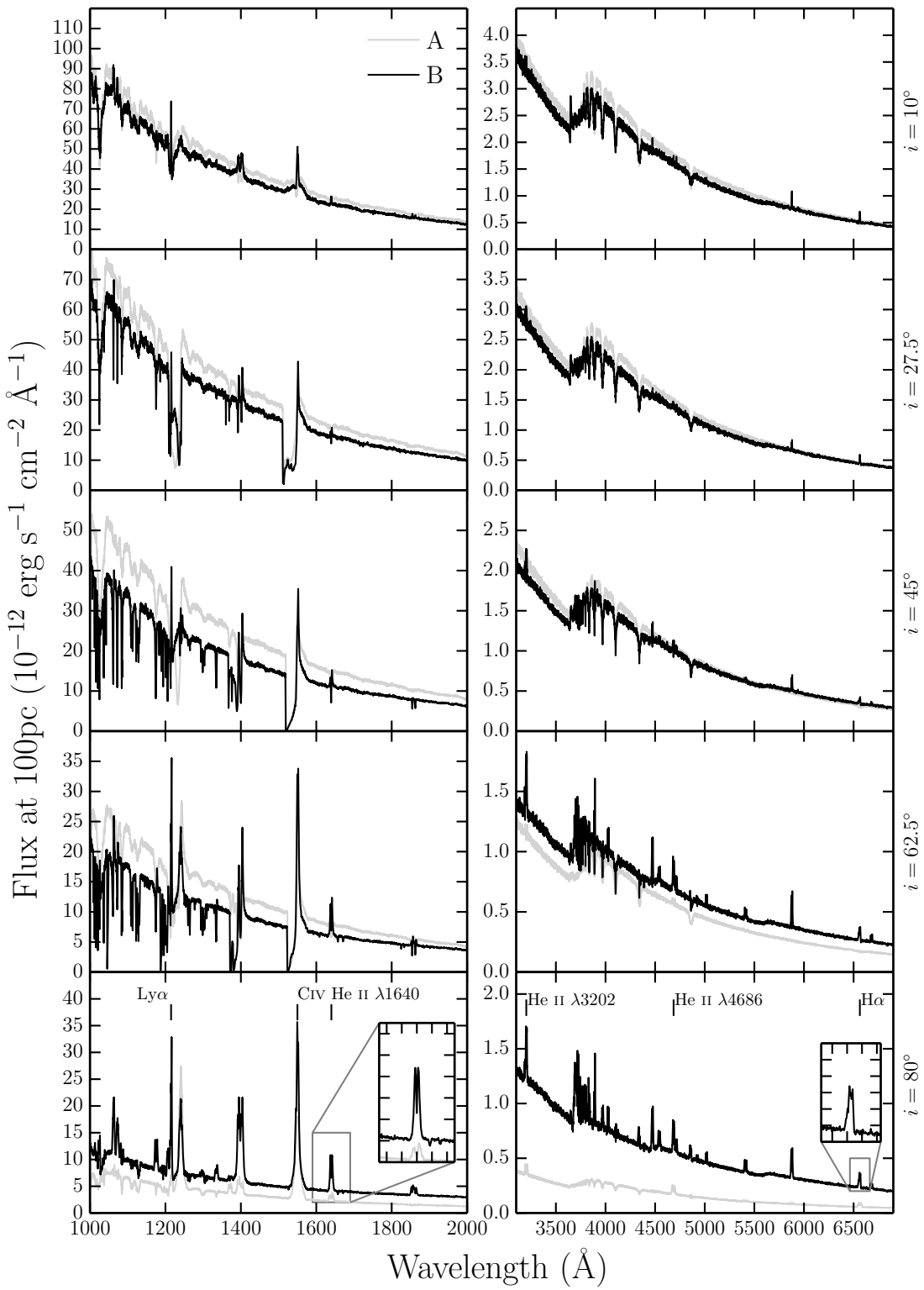


FIGURE 4.9: UV (left) and optical (right) synthetic spectra for model B computed at sightlines of 10, 27.5, 45, 62.5 and 80 degrees. Model A is shown in grey for comparison. The inset plots show zoomed-in line profiles for He II $\lambda 1640$ and H α . The Balmer and He are double-peaked, albeit with narrower profiles. Strong He II $\lambda 4686$ emission can be seen, as well as a trend of a deeper Balmer jump with decreasing inclination.

profiles. Thus, most of the wind has an ionization parameter of $\log U \sim 2$ (see Fig. 4.5). This means H and He are fully ionized throughout much of the wind and are successful in producing recombination features. However, the line opacity throughout the wind is too low to produce noticeable blue shifted absorption. We suspect that the systems that exhibit such profiles must possess a higher degree of ionization stratification, although the lack of contemporary observations means it is not known for certain if the P-Cygni profiles in UV resonance lines and optical H and He lines exist simultaneously. Ionization stratification could be caused by a clumpy flow, in which the ionization state changes due to small scale density fluctuations, or a stratification in density and ionizing radiation field over larger scales. Invoking clumpiness in these outflows is not an unreasonable hypothesis. Theories of line-driven winds predict an unstable flow (MacGregor et al. 1979; Owocki and Rybicki 1984, 1985), and simulations of CV disc winds also produce density inhomogeneities (Proga et al. 1998, 2002). Tentative evidence for clumping being directly related to P-Cygni optical lines comes from the fact that Prinja et al. (2000) found the dwarf nova BZ Cam’s outflow to be unsteady and highly mass-loaded in outburst, based on observations of the UV resonance lines. This system has also exhibited P-Cygni profiles in He I $\lambda 5876$ and H α when in a high-state (Patterson et al. 1996; Ringwald and Naylor 1998). The degree of ionization and density variation and subsequent line opacities may be affected by our model parameters and the specific parameterisation we have adopted.

In the UV, the model still produces all the observed lines, and deep P-Cygni profiles are produced in the normal resonance lines, as discussed in section 4.2. However, the UV spectra also display what is perhaps the biggest problem with this revised model, namely the strength of resonance line emission at low and intermediate inclinations. In order to generate strong optical wind signatures, we have adopted wind parameters that lead to very high densities at the base of the wind ($n_e \sim 10^{13} - 10^{14} \text{ cm}^{-3}$). This produces the desired optical recombination emission, but also increases the role of collisional excitation in the formation of the UV resonance lines. This explains the pronounced increase in the emission component of the CIV $\lambda 1550$ resonance line, for example, relative to what was seen in the benchmark model (compare Figures 4.6 and 4.9). The strength of this component in the revised model is probably somewhat too high to be consistent with UV observations of high-state CVs (see e.g. Long et al. 1991, 1994; Noebauer et al. 2010).

4.5.2 Continuum Shape and the Balmer Jump

The wind now also has a clear effect on the continuum shape, as shown by Fig. 4.11. In fact, the majority of the escaping spectrum has been reprocessed in some way by

the wind, either by electron scattering (the wind is now moderately Thomson-thick), or by bound-free processes. This is demonstrated by the flatter spectral shape and the slight He photoabsorption edge present in the optical spectrum (marked in Fig. 4.10). This reprocessing is also responsible for the change in continuum level between models A and B. In addition, Figures 4.9, 4.10 and 4.11 clearly demonstrate that the wind produces a recombination continuum sufficient to completely fill in the Balmer jump at high inclinations.² This might suggest that Balmer continuum emission from a wind can be important in shaping the Balmer jump region, as originally suggested by Knigge et al. (1998b; see also Hassall et al. 1985).

It should be acknowledged, however, that the Balmer jump in high-state CVs would naturally weaken at high inclinations due to limb darkening effects (La Dous 1989b,a). Although we include a simple limb darkening law which affects the emergent flux at each inclination, we do not include it as a *frequency dependent* opacity in our model. As a result, the efficiency of filling in the Balmer jump should really be judged at low and medium inclinations, where, although prominent, the recombination continuum does not overcome the disc atmosphere absorption. In addition, this effect could mean that any model which successfully fills in the jump at low inclinations could lead to a Balmer jump in emission at high inclinations. In any case, to properly understand this phenomenon, a fully self-consistent radiative transfer calculation of both the disc atmosphere and connected wind is required.

4.5.3 Line Profile Shapes: Producing Single-Peaked Emission

Fig. 4.12 shows how the H α profile changes with the kinematics of the wind for an inclination of 80°. The main prediction is that dense, slowly accelerating wind models produce narrower emission lines. This is *not* due to radial velocity shear. As stated by MC96, that mechanism can only work if poloidal and rotational velocity gradients satisfy $(dv_l/dr)/(dv_\phi/dr) \gtrsim 1$; in our models, this ratio is always $\lesssim 0.1$. Instead, the narrow lines predicted by our denser wind models can be traced to the base of the outflow becoming optically thick in the continuum, such that the line emission from the base of the wind cannot escape to the observer. In such models, the ‘line photosphere’ (the $\tau \simeq 1$ surface of the line-forming region) moves outwards, towards larger vertical and cylindrical distances. This reduces the predicted line widths, since the rotational velocities – which normally provide the main line broadening mechanism at high inclination – drop off as $1/r$. This is not to say that the MC96 mechanism could not be at work in CV winds. For example, it would be worth investigating alternative prescriptions

²Note that the apparent absorption feature just redward of the Balmer jump in these models is artificial. It is caused by residual line blanketing in the stellar atmospheres, which our models cannot fill in since they employ a 20-level H atom.

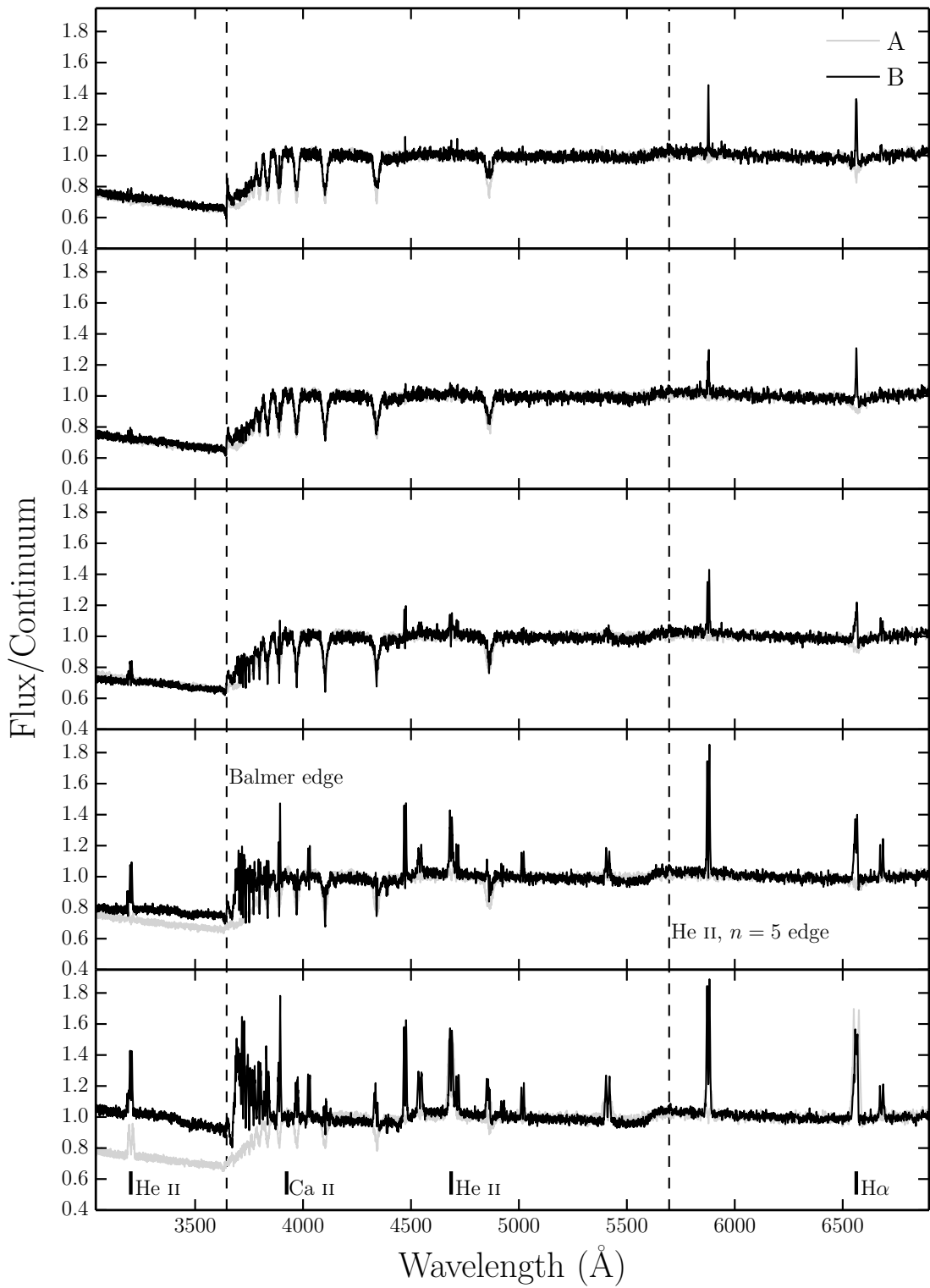


FIGURE 4.10: Synthetic optical spectra from model B computed for sightlines of 10, 27.5, 45, 62.5 and 80 degrees. Model A is shown in grey for comparison. In these plots the flux is divided by a polynomial fit to the underlying continuum redward of the Balmer edge, so that line-to-continuum ratios and the true depth of the Balmer jump can be shown.

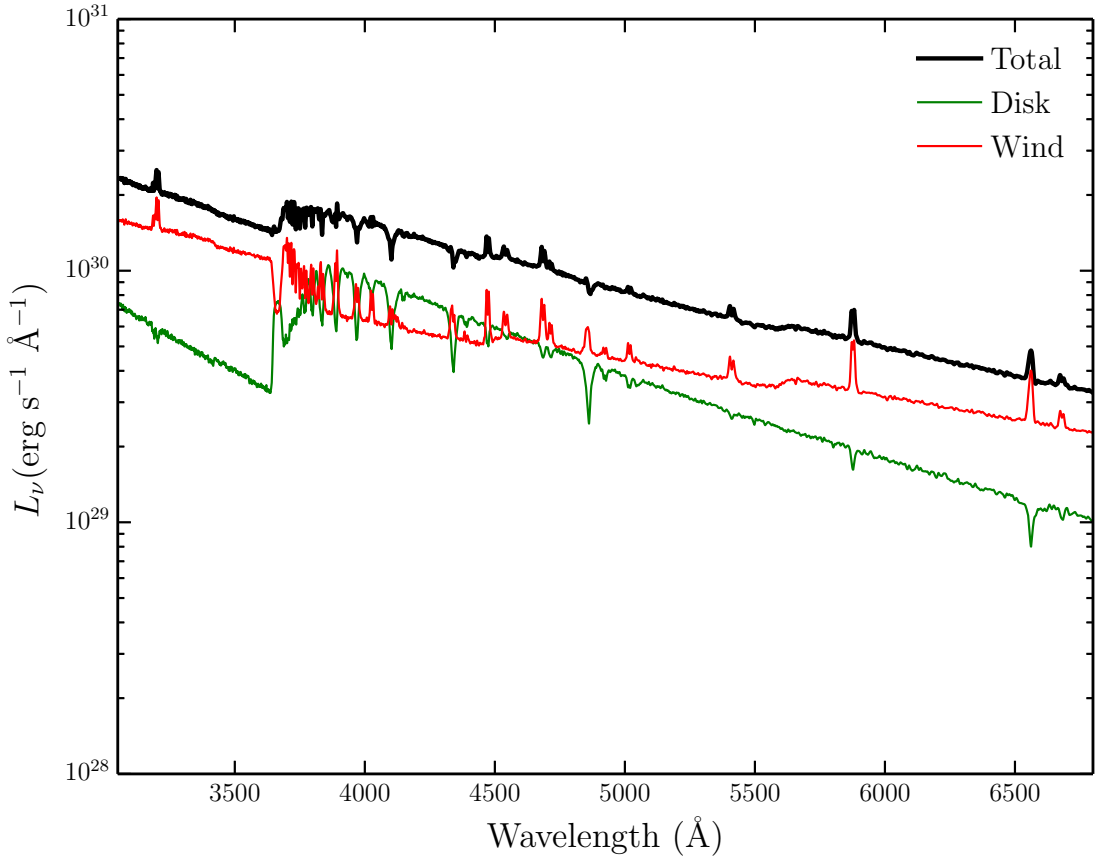


FIGURE 4.11: Total packet-binned spectra across all viewing angles, in units of monochromatic luminosity. The thick black line shows the total integrated escaping spectrum, while the green line shows disc photons which escape without being reprocessed by the wind. The red line show the contributions from reprocessed photons. In this denser model the reprocessed contribution is significant compared to the escaping disc spectrum. The Balmer continuum emission is prominent, and the wind has a clear effect on the overall spectral shape.

for the wind velocity field, as well as the possibility that the outflows may be clumped. An inhomogeneous flow (which has been predicted in CVs; see section 5.2) might allow large radial velocity shears to exist while still maintaining the high densities needed to produce the required level of emission. However, such an investigation is beyond the scope of the present paper.

In our models, single-peaked line profiles are produced once the line forming region has been pushed up to $\sim 10^{11}$ cm ($\sim 150 R_{WD}$) above the disc plane. This number may seem unrealistically large, but the vertical extent of the emission region is actually not well constrained observationally. In fact, multiple observations of eclipsing NLs show that the H α line is only moderately eclipsed compared to the continuum (e.g. Baptista et al. 2000; Groot et al. 2004; see also section 5.4), implying a significant vertical extent for the line-forming region. This type of model should therefore not be ruled out *a*

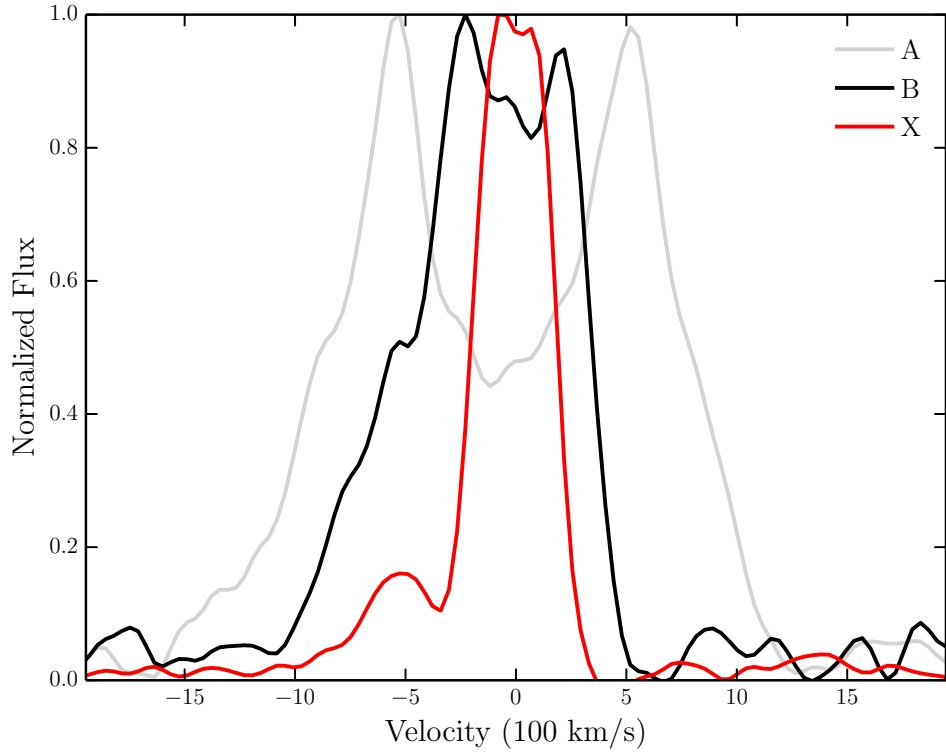


FIGURE 4.12: $\text{H}\alpha$ line profiles, normalized to 1, plotted in velocity space for three models with varying kinematic properties, computed at an inclination of 80° . The benchmark model and the improved optical model described in section 6 are labeled as A and B respectively, and a third model (X) which has an increased acceleration length of $R_v = 283.8 R_{WD}$, and $\alpha = 4$ is also shown. The x -axis limits correspond to the Keplerian velocity at $4R_{WD}$, the inner edge of the wind. We observe a narrowing of the lines, and a single-peaked line in model X. This is not due to radial velocity shear (see section 5.3).

a priori, but this specific model was not adopted as our optically optimized model due to its unrealistically high continuum level in eclipse.

4.5.4 Sensitivity to Model Parameters

This revised model demonstrates that one can achieve a more realistic optical spectrum by altering just two kinematic parameters. However, it may also be possible to achieve this by modifying other free parameters such as \dot{M}_{wind} , the opening angles of the wind and the inner and outer launch radii. For example, increasing the mass-loss rate of the wind increases the amount of recombination emission (which scales as ρ^2), as well as lowering the ionization parameter and increasing the optical depth through the wind. Larger launching regions and covering factors tend to lead to a larger emitting volume, but this is moderated by a decrease in density for a fixed mass-loss rate. We also note that the inner radius of $4 R_{WD}$ adopted by SV93 affects the emergent UV spectrum seen

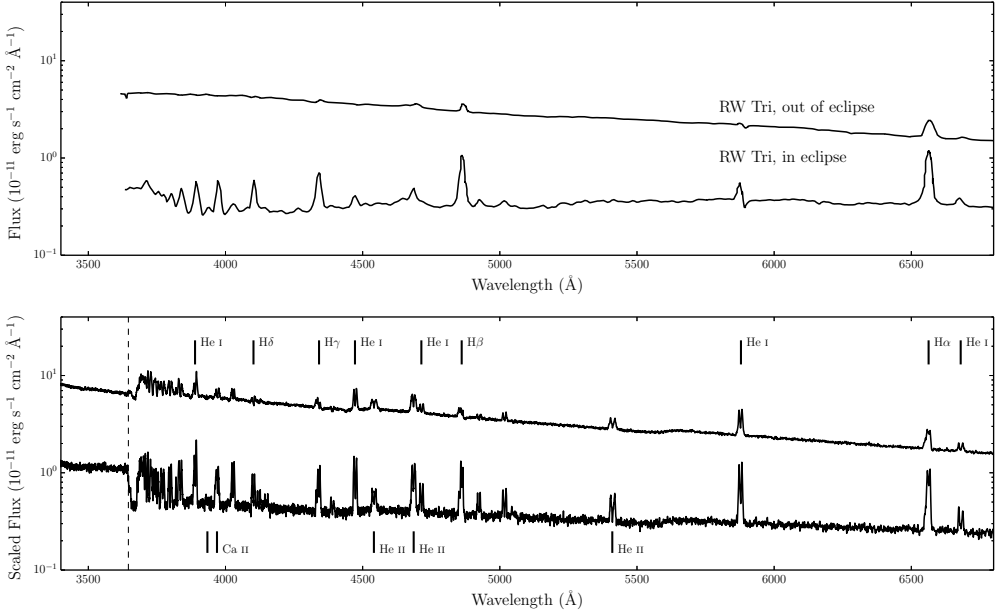


FIGURE 4.13: *Top Panel:* In and out of eclipse spectra of the high inclination NL RW Tri. *Bottom Panel:* In and out of eclipse synthetic spectra from model B. The artificial ‘absorption’ feature just redward of the Balmer jump is caused for the reasons described in section 5.2.

at inclinations $< \theta_{min}$ as the inner disc is uncovered. This causes less absorption in the UV resonance lines, but the effect on the optical spectrum is negligible. We have verified this general behaviour, but we suggest that future work should investigate the effect of these parameters in more detail, as well as incorporating a treatment of clumping. If a wind really does produce the line and continuum emission seen in optical spectra of high-state CVs, then understanding the true mass-loss rate and geometry of the outflow is clearly important.

4.5.5 Comparison to RW Tri

Fig. 4.13 shows a comparison of the predicted out-of-eclipse and mid-eclipse spectra against observations of the high-inclination nova-like RW Tri. The inclination of RW Tri is somewhat uncertain, with estimates including 70.5° (Smak 1995), 75° (Groot et al. 2004), 80° (Longmore et al. 1981) and 82° (Frank and King 1981). Here, we adopt $i = 80^\circ$, but our qualitative conclusions are not particularly sensitive to this choice. We follow LK02 is setting the value of r_{disc} (the maximum radius of the accretion disc) to $34.3 R_{WD}$. When compared to the semi-major axis of RW Tri, this value is perhaps lower than one might typically expect for NLs (Harrop-Allin and Warner 1996). However, it is consistent with values inferred by Rutten et al. (1992). We emphasize that this model is in no sense a fit to this – or any other – data set.

The similarity between the synthetic and observed spectra is striking. In particular, the revised model produces strong emission in all the Balmer lines, with line-to-continuum ratios comparable to those seen in RW Tri. Moreover, the line-to-continuum contrast increases during eclipse, as expected for emission produced in a disc wind. This trend is in line with the observations of RW Tri, and it has also been seen in other NLs, including members of the SW Sex class (Neustroev et al. 2011). As noted in section 5.2, the majority of the escaping radiation has been reprocessed by the wind in some way (particularly the eclipsed light).

However, there are also interesting differences between the revised model and the RW Tri data set. For example, the model exhibits considerably stronger He II features than the observations, which suggests that the overall ionization state of the model is somewhat too high. As discussed in section 5.3, the optical lines are narrow, but double-peaked. This is in contrast to what is generally seen in observations of NLs, although the relatively low resolution of the RW Tri spectrum makes a specific comparison difficult. In order to demonstrate the double-peaked nature of the narrower lines, we choose not to smooth the synthesized data to the resolution of the RW Tri dataset. If the data was smoothed, the H α line would appear single-peaked.

4.6 Conclusions

We have investigated whether a disc wind model designed to reproduce the UV spectra of high-state CVs would also have a significant effect on the optical spectra of these systems. We find that this is indeed the case. In particular, the model wind produces H and He recombination lines, as well as a recombination continuum blueward of the Balmer edge. We do not produce P-Cygni profiles in the optical H and He lines, which are seen in a small fraction of CV optical spectra. Possible reasons for this are briefly discussed in section 5.2.

We have also constructed a revised benchmark model which is designed to more closely match the optical spectra of high-state CVs. This optically optimized model produces all the prominent optical lines in and out of eclipse, and achieves reasonable verisimilitude with the observed optical spectra of RW Tri. However, this model also has significant shortcomings. In particular, it predicts stronger-than-observed He II lines in the optical region and too much of a collisionally excited contribution to the UV resonance lines.

Based on this, we argue that recombination emission from outflows with sufficiently high densities and/or optical depths might produce the optical lines observed in CVs, and may also fill in the Balmer absorption edge in the spectrum of the accretion disc,

thus accounting for the absence of a strong edge in observed CV spectra. In section 5.3, we demonstrate that although the double peaked lines narrow and single-peaked emission can be formed in our densest models, this is not due to the radial velocity shear mechanism proposed by MC96. We suggest that ‘clumpy’ line-driven winds or a different wind parameterization may nevertheless allow this mechanism to work. We also note the possibility that, as in our denser models, the single-peaked lines are formed well above the disc, where rotational velocities are lower.

It is not yet clear whether a wind model such as this can explain all of the observed optical features of high-state CVs – further effort is required on both the observational and modelling fronts. However, our work demonstrates that *disc winds matter*. They are not just responsible for creating the blue-shifted absorption and P-Cygni profiles seen in the UV resonance lines of high-state CVs, but can also have a strong effect on the optical appearance of these systems. In fact, most of the optical features characteristic of CVs are likely to be affected – and possibly even dominated – by their disc winds. Given that optical spectroscopy plays the central role in observational studies of CVs, it is critical to know where and how these spectra are actually formed. We believe it is high time for a renewed effort to understand the formation of spectra in accretion discs and associated outflows.

Chapter 5

Testing Quasar Unification: Radiative Transfer In Clumpy Winds

This chapter is based on the publication of the same title, published in MNRAS in August 2015 (Matthews et al. 2015).

5.1 Introduction

The spectra of quasars and luminous active galactic nuclei (AGN) typically exhibit a series of strong emission lines with an underlying blue continuum - the so-called ‘big blue bump’ (BBB). The BBB is often attributed to emission from a geometrically thin, optically thick accretion disc surrounding the central black hole (BH), similar to that described by [Shakura and Sunyaev \(1973\)](#). In addition to the *inflowing* accreting material, *outflows* are ubiquitous in AGN and quasars ([Kellermann et al. 1989](#); [Ganguly and Brotherton 2008](#)). These outflows can take the form of highly collimated radio jets (e.g. [Hazard et al. 1963](#); [Potash and Wardle 1980](#); [Perley et al. 1984](#); [Marscher 2006](#)), or mass-loaded ‘winds’ emanating from the accretion disc ([Weymann et al. 1991](#); [Turner and Miller 2009](#)). Outflows in AGN offer a potential feedback mechanism through which the central source can affect its environment ([King 2003, 2005](#); [Fabian 2012](#)) – feedback that is required in models of galaxy evolution ([Springel et al. 2005](#)) and may explain the ‘ $M - \sigma$ ’ relation ([Silk and Rees 1998](#); [Häring and Rix 2004](#)).

Perhaps the clearest evidence of outflows in AGN is the blueshifted ($\sim 0.1c$) broad absorption lines (BALs) in the ultraviolet seen in approximately 20% of quasars ([Weymann](#)

et al. 1991; Knigge et al. 2008; Allen et al. 2011). The simplest explanation for the incidence of BAL quasars (BALQSOs) is in terms of an accretion disc wind. According to this paradigm, a biconical wind rises from the accretion disc and the BALQSO fraction is associated with the covering factor of the outflow. Polarisation studies suggest that the wind is roughly equatorial (Goodrich and Miller 1995; Cohen et al. 1995), although there is also evidence for polar BAL outflows in radio-loud (RL) sources (Zhou et al. 2006; Ghosh and Punsly 2007).

Due to their ubiquitous nature, disc winds offer a natural way to *unify* much of the diverse phenomenology of luminous AGN and quasars (e.g. Murray et al. 1995; Elvis 2000). Depending on viewing angle, an observer may see a BALQSO or normal ‘Type 1’ quasar. Within this geometric unification framework, the broad-line region (BLR) can correspond either to the dense wind base or clumps embedded in the outflow. A biconical wind model can also readily explain the various sub-classifications of BALQSOs: HiBALQSOs, which only exhibit high ionization line absorption; LoBALQSOs, which also show absorption in lower ionization state species such as Mg II and Al III; and FeLoBALQSOs, which show further absorption in Fe II and III. In unified geometric models, this is generally attributed to ionization stratification of the outflow (e.g. Elvis 2000).

Despite the importance of disc winds in shaping quasar and AGN spectra, much of the underlying outflow physics remains uncertain. Several driving mechanisms have been proposed, including thermal pressure (Weymann et al. 1982; Begelman et al. 1991), magnetocentrifugal forces (Blandford and Payne 1982; Pelletier and Pudritz 1992) and radiation pressure on spectral lines (‘line-driving’; Lucy and Solomon 1970; Shlosman et al. 1985; Murray et al. 1995). Of these, line-driving is possibly the most attractive, as strong absorption lines are already seen in BALQSOs and the X-ray spectra of AGN (Reeves et al. 2003; Pounds and Reeves 2009; Tombesi et al. 2010). The efficiency of line-driving is crucially dependent on the ionization state of the outflowing plasma, meaning that it is difficult to prevent the wind becoming over-ionized and ‘failing’ in the presence of strong X-rays. Murray et al. (1995) proposed a potential solution: a region of ‘hitchhiking gas’ that could shield the wind from the central X-ray source. An additional or alternative solution is that the wind is clumped (e.g. Hamann et al. 2013) possibly on multiple scale lengths. Local density enhancements could lower the ionization parameter of the plasma while still maintaining the same mass-loss rate and column density.

Evidence for dense substructures in AGN winds is widespread. BALQSOs show complex absorption line profiles (Ganguly et al. 2006; Simon and Hamann 2010) and exhibit variability in these profile shapes (Capellupo et al. 2011, 2012, 2014). AGN generally

show variability in X-ray absorption components (e.g. Risaliti et al. 2002) and many models for the BLR consist of clumps embedded in an outflow (Krolik et al. 1981; Emmering et al. 1992; de Kool and Begelman 1995; Cassidy and Raine 1996). Clumping can be caused by magnetic confinement (de Kool and Begelman 1995), or the instabilities inherent to line-driven winds (Lucy and Solomon 1970; MacGregor et al. 1979; Carlberg 1980; Owocki and Rybicki 1984, 1985). Additionally, clumping is required to explain the electron scattering wings of emission lines formed in line-driven hot star winds (Hillier 1991). Complex substructures are also produced in simulations of line-driven outflows in AGN, although on very different scales to line-driven instabilities (Proga et al. 2000; Proga and Kallman 2004; Proga and Kurosawa 2010; Proga et al. 2014). In summary, clumpy winds offer an observationally motivated and theoretically predicted way to lower the ionization state of a plasma, possibly in tandem with a shielding scenario.

We have been engaged in a project to determine whether it is possible to simulate the properties of the spectra of AGN, including BALQSOs, using simple kinematic prescriptions for biconical disc winds. To address this question, we use a Monte Carlo radiative transfer (MCRT) code that calculates the ionization structure of the wind and simulates the spectra from such a system (Sim et al. 2008, 2010; Higginbottom et al. 2013, 2014, hereafter H13 and H14). The results have been encouraging in the sense that in H13, we showed we could produce simulated spectra that resembled that of BALQSOs, as long as the luminosity of the X-ray source was relatively low, of order 10^{43} erg s $^{-1}$ and the mass loss rate was relatively high, of order the mass accretion rate. However, at higher X-ray luminosities, the wind was so ionized that UV absorption lines were not produced. In addition, and in part due to limitations in our radiative transfer code, the model failed to produce spectra with strong emission lines at any inclination angle.

Here we attempt to address both of these issues, by introducing clumping into our model and a more complete treatment of H and He into our radiative transfer calculations. The remainder of this paper is organized as follows: In section 2, we describe some of the important photoionization and MCRT aspects of the code. We then outline the model in section 3, including a description of our clumping implementation and success criteria. Section 4 contains the results from a clumped model, with comparisons to observational data, as well as some discussion. Finally, we summarise our findings in section 5.

5.2 Ionization and Radiative Transfer

For this study, we use the MCRT code `PYTHON`¹ we have developed to carry out our radiative transfer and photoionization simulations in non-local-thermodynamic-equilibrium (non-LTE). The code can be used to model a variety of disc-wind systems; applications have included accreting white dwarfs (Long & Knigge 2002, hereafter LK02; Noebauer et al. 2010; Matthews et al. 2015, hereafter M15), young-stellar objects (Sim et al. 2005) and quasars/AGN (H13, H14).

The code operates as follows: This outflow is discretized into $n_x \times n_z$ cells in a 2.5D cylindrical geometry with azimuthal symmetry. From some initial conditions in each cell (typically $T_e \sim 40,000\text{K}$ in AGN, with dilute LTE abundances), the code first calculates the ionization structure of the wind in a series of iterations. Each iteration in an “ionization cycle” consists of generating photons, actually photon packets, from an accretion disc and central object, and calculating how these photon bundles scatter through the wind (eventually escaping the outflow or hitting the disk). The ionization and temperature structure is updated based on the properties of the radiation field in each cell, and the process is repeated. The radiative transfer and thermal balance is carried out according to the principle of radiative equilibrium, which assumes both statistical equilibrium and that radiative heating balances radiative cooling. Once the ionization structure has converged, it is held fixed, and synthetic spectra are generated at specific inclination angles in a series of ”spectral cycles”. LK02 provide a more detailed description of the original code; various improvements have been made since then and are described by Sim et al. (2005), H13 and M15. We focus here on the specific changes made for this study intended to improve the ionization calculation of H and He and to allow for clumping in the wind.

5.2.1 Line transfer

Our approach to line transfer is based upon the macro-atom implementation developed by Lucy (2002, 2003), in which the energy flows through the system are described in terms of indivisible energy quanta of radiant or kinetic energy (‘ r -packets’ and ‘ k -packets’ respectively; see also section 5.3.1), which are reprocessed by ‘macro-atoms’ with associated transition probabilities. We use the Sobolev approximation (e.g. Sobolev 1957, 1960; Rybicki and Hummer 1978) to compute the location of line interactions. In our case, for reasons of computational efficiency, we adopt the hybrid macro-atom scheme described by M15. In this scheme, the energy packets interact with either two-level ‘simple atoms’ or full macro-atoms. This allows one to treat non-LTE line transfer

¹Named c. 1995, predating the inexorable rise of a certain programming language.

in radiative equilibrium without approximation for elements that are identified as full macro-atoms, while maintaining the fast ‘two-level’ treatment of resonance lines when elements are identified as simple atoms (see M15). In this study, only H and He are treated as macro-atoms, because the process is computationally intensive, and we expect recombination to be particularly important in determining their level populations and resultant line emission. We are also especially interested in the contribution to AGN spectra of Lyman α . H13 treated all atoms in a two-level approximation.

5.2.2 Ionization and Excitation Treatment

Macro-atoms have their ion and level populations derived from MC rate estimators as described by Lucy (2002,2003). Previously (LK02, H13, M15), we used a modified Saha approach to calculate the ionization fractions of simple-ions. As part of this effort, we have now improved PYTHON to explicitly solve the rate equations between ions in non-LTE. This dispenses with a number of small assumptions made in the modified Saha approach, is more numerically stable, and prepares for a more accurate treatment of other physical processes in future.

In order to calculate the photoionization rate, we model the SED in a grid cell using the technique described by H13. In this scheme, the mean intensity, J_ν in a series of n bands is modeled as either a power law or exponential in frequency ν , with the fit parameters deduced from band-limited radiation field estimators. This allows the calculation of a photoionization rate estimator. Ion abundances are then calculated by solving the rate equations between ions. We include collisional ionization and photoionization balanced with radiative, dielectronic and collisional (three-body) recombination. As in M15, we use a dilute Boltzmann approximation to calculate the populations of levels for simple-ions. This dilute approximation is not required for macro-atom levels.

5.2.3 Physical Processes

We include free-free, bound-free and bound-bound heating and cooling processes in the model. For radiative transfer purposes we treat electron scattering in the Thomson limit, but take full account of Compton heating and cooling when calculating the thermal balance of the plasma (see H13). Adiabatic cooling is included, but is insignificant in most of the outflow.

5.2.4 Atomic Data

We use the same atomic data described by LK02 as updated by H13 and M15, with the addition of direct (collisional) ionization and recombination data from Dere (2007). Photoionization cross-sections are from TOPBASE (Cunto et al. 1993) and Verner et al. (1996). Radiative recombination rate coefficients are taken from the CHIANTI database version 7.0 (Dere et al. 1997; Landi et al. 2012). We use ground state recombination rates from Badnell (2006) where available, and otherwise default to calculating recombination rates from the Milne relation. Free-free Gaunt factors are from Sutherland (1998).

5.3 A Clumpy Biconical Disk Wind Model for Quasars

Our kinematic prescription for a biconical disc wind model follows Shlosman and Vitello (1993), and is described further by LK02, H13 and M15. A schematic is shown in Fig. 5.1, with key aspects marked. The general biconical geometry is similar to that invoked by Murray et al. (1995) and Elvis (2000) to explain the phenomenology of quasars and BALQSOs.

5.3.1 Photon Sources

We include two sources of r-packets in our model: An accretion disc and a central X-ray source. The accretion disc is assumed to be geometrically thin, but optically thick. Accordingly, we treat the disc as an ensemble of blackbodies with a Shakura and Sunyaev (1973) effective temperature profile. The emergent SED is then determined by the specified accretion rate (\dot{m}) and central BH mass (M_{BH}). All photon sources in our model are opaque, meaning that r-packets that strike them are destroyed. The inner radius of the disc extends to the innermost stable circular orbit (ISCO) of the BH. We assume a Schwarzschild BH with an ISCO at $6 r_G$, where $r_G = GM_{BH}/c^2$ is the gravitational radius. For a $10^9 M_\odot$ BH, this is equal to 8.8×10^{14} cm or $\sim 10^{-4}$ pc.

The X-ray source is treated as an isotropic sphere at the ISCO, which emits r-packets according to a power law in flux with index α_X , of the form

$$F_X(\nu) = K_X \nu^{\alpha_X}. \quad (5.1)$$

The normalisation, K_X of this power law is such that it produces the specified 2-10 keV luminosity, L_X . Photons, or r-packets, produced by the accretion disc and central X-ray source are reprocessed by the wind. This reprocessing is dealt with by enforcing strict

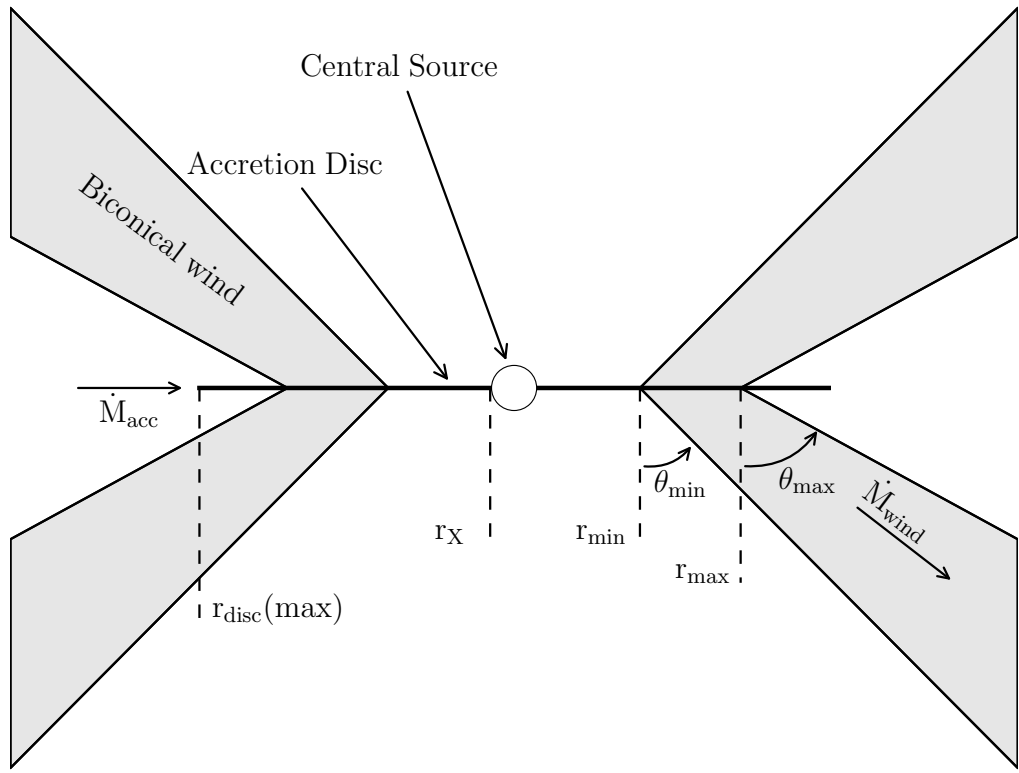


FIGURE 5.1: A cartoon showing the geometry and some key parameters of our biconical wind model.

radiative equilibrium (*modulo* adiabatic cooling; see section 2.3) via an indivisible energy packet constraint (see Lucy 2002, M15).

5.3.2 Kinematics and Geometry

In the SV93 model, a biconical disc wind rises from the accretion disc between launch radii r_{\min} and r_{\max} . The opening angles of the wind are set to θ_{\min} and θ_{\max} . The poloidal velocity along each individual streamline at a poloidal distance l is then given by

$$v_l = v_0 + [v_\infty(r_0) - v_0] \frac{(l/R_v)^\alpha}{(l/R_v)^\alpha + 1}, \quad (5.2)$$

where v_0 is the velocity at the base of the streamline, α is an exponent governing how quickly the wind accelerates and R_v is the ‘acceleration length’, defined as the distance at which the outflow reaches half of its terminal velocity, v_∞ . The terminal velocity is set to a fixed multiple of the escape velocity, v_{esc} , at the base of the streamline (radius r_0). The rotational velocity, v_ϕ , is initially Keplerian ($v_k = [GM/r_0]^{1/2}$), and the wind

conserves specific angular momentum, such that

$$v_\phi r = v_k r_0. \quad (5.3)$$

The velocity law is crucial in determining the output spectra, as it affects not only the projected velocities along the line of sight, but also the density and ionization state of the outflow. A wind that accelerates more slowly will have a denser wind base with correspondingly different ionization and emission characteristics.

5.3.3 A Simple Approximation for Clumping

In our previous modelling efforts, we assumed a smooth outflow, in which the density at a given point was determined only by the kinematic parameters and mass loss rate. However, as already discussed, AGN winds exhibit significant substructure – the outflow is expected to be *clumpy*, rather than smooth, and probably on a variety of scales. A clumpy outflow offers a possible solution to the so-called ‘over-ionization problem’ in quasar and AGN outflows ([Hamann et al. 2013](#)). This is the main motivation for incorporating clumping into our model.

Implementing a treatment of clumping is challenging, for two main reasons. First, the physical scale lengths and density contrasts in AGN outflows are not well-constrained from observations. Second, there are significant computational difficulties associated with adequately resolving and realistically modelling a series of small scale, high density regions with a MCRT code. Given the lack of knowledge about the actual type of clumping, we have adopted a simple approximation used successfully in stellar wind modelling, known as *microclumping* (e.g. [Hamann and Koesterke 1998](#); [Hillier and Miller 1999](#); [Hamann et al. 2008](#)). The underlying assumption of microclumping is that clump sizes are much smaller than the typical photon mean free path, and thus the clumps are both geometrically and optically thin. This approach allows one to introduce a ‘volume filling factor’, f_V . The intra-clump medium is assumed to be a vacuum, so the density of the clumps is then multiplied by the “density enhancement” $D = 1/f_V$. Opacities, κ , and emissivities, ϵ , can then be expressed as

$$\kappa = f_V \kappa_C(D); \quad \epsilon = f_V \epsilon_C(D). \quad (5.4)$$

Here the subscript C denotes that the quantity is calculated using the enhanced density in the clump. The resultant effect is that, *for fixed temperature*, processes that are linear in density, such as electron scattering, are unchanged, as f_V and D will cancel out. However, any quantity that scales with the square of density, such as collisional excitation or recombination, will increase by a factor of D .

In our models, the temperature is not fixed, and is instead set by balancing heating and cooling in a given cell. In the presence of an X-ray source, this thermal balance is generally dominated by bound-free heating and line cooling. The main effect of including clumping in our modelling is that it moderates the ionization state due to the increased density. This allows an increase in the ionizing luminosity, amplifying the amount of bound-free heating and also increasing the competing line cooling term (thermal line emission). Our clumping treatment is necessarily simple; it does not adequately represent the complex substructures and stratifications in ionization state we expect in AGN outflows. Nevertheless, this parameterization allows simple estimates of the effect clumping has on the ionization state and emergent line emission.

5.3.4 The Simulation Grid

Using this prescription, we conducted a limited parameter search over a 5-dimensional parameter space involving the variables r_{min} , θ_{min} , f_V , α and R_v . The grid points are shown in Table 1. The aim here was to first fix M_{BH} and \dot{m} to their H13 values, and increase L_X to 10^{45} erg s $^{-1}$ (a more realistic value for a quasar of $10^9 M_\odot$ and an Eddington fraction of 0.2; see section 5.4.3).

We then evaluated these models based on how closely their synthetic spectra reproduced the following properties of quasars and BALQSOs:

- UV absorption lines with $BI > 0$ at $\sim 20\%$ of viewing angles (e.g. Knigge et al. 2010);
- Line emission emerging at low inclinations, with $EW \sim 40\text{\AA}$ in C IV 1550\text{\AA} (e.g. Shen et al. 2011);
- H recombination lines with $EW \sim 50\text{\AA}$ in Ly α (e.g. Shen et al. 2011);
- Mg II and Al III (LoBAL) absorption features with $BI > 0$ at a subset of BAL viewing angles;
- Verisimilitude with quasar composite spectra.

Here BI is the ‘Balnicity Index’ (Weymann et al. 1991), given by

$$BI = \int_{3000 \text{ km s}^{-1}}^{25000 \text{ km s}^{-1}} \left(1 - \frac{f(v)}{0.9}\right) dv. \quad (5.5)$$

The constant $C = 0$ everywhere, unless the normalized flux has satisfied $f(v) < 0.9$ continuously for at least 2000 km s $^{-1}$, whereby C is set to 1.

Parameter	Grid Point Values		
r_{min}	$60r_g$	$180r_g$	$300r_g$
θ_{min}	55°	70°	
R_v	10^{18}cm	10^{19}cm	
α	0.5	0.6	0.75
f_V	0.01	0.1	

TABLE 5.1: The grid points used in the parameter search. The sensitivity to some of these parameters is discussed further in section 5.4.5

In the next section, we present one of the most promising models, which we refer to as the fiducial model, and discuss the various successes and failures with respect to the above criteria. This allows us to gain insight into fundamental geometrical and physical constraints and assess the potential for unification. We then discuss the sensitivity to key parameters in section 5.4.5. The full grid, including output synthetic spectra and plots can be found at jhmatthews.github.io/quasar-wind-grid/.

5.4 Results and Discussion From A Fiducial Model

Here we describe the results from a fiducial model, and discuss these results in the context of the criteria presented in section 3.4. The parameters of this model are shown in Table 2. Parameters differing from the benchmark model of H13 are highlighted with an asterisk. In this section, we examine the physical conditions of the flow, and present the synthetic spectra, before comparing the X-ray properties of this particular model to samples of quasars and luminous AGN.

5.4.1 Physical Conditions and Ionization State

Fig. 5.2 shows the physical properties of the wind. The wind rises slowly from the disc at first, with densities within clumps of $n_H \sim 10^{11} \text{ cm}^{-3}$ close to the disc plane, where n_H is the local number density of H. The flow then accelerates over a scale length of $R_V = 10^{19} \text{ cm}$ up to a terminal velocity equal to the escape velocity at the streamline base ($\sim 10,000 \text{ km s}^{-1}$). This gradual acceleration results in a wind that exhibits a stratified ionization structure, with low ionization material in the base of the wind giving way to highly ionized plasma further out. This is illustrated in Fig. 5.2 by the panels showing the ion fraction $F = n_j/n_{tot}$ of some important ions. With a clumped wind, we are able to produce the range of ionization states observed in quasars and BALQSOs, while adopting a realistic 2 – 10 keV X-ray luminosity of $L_X = 10^{45} \text{ erg s}^{-1}$. Without clumping, this wind would be over-ionized to the extent that opacities in e.g., C IV would be entirely negligible (see H13).

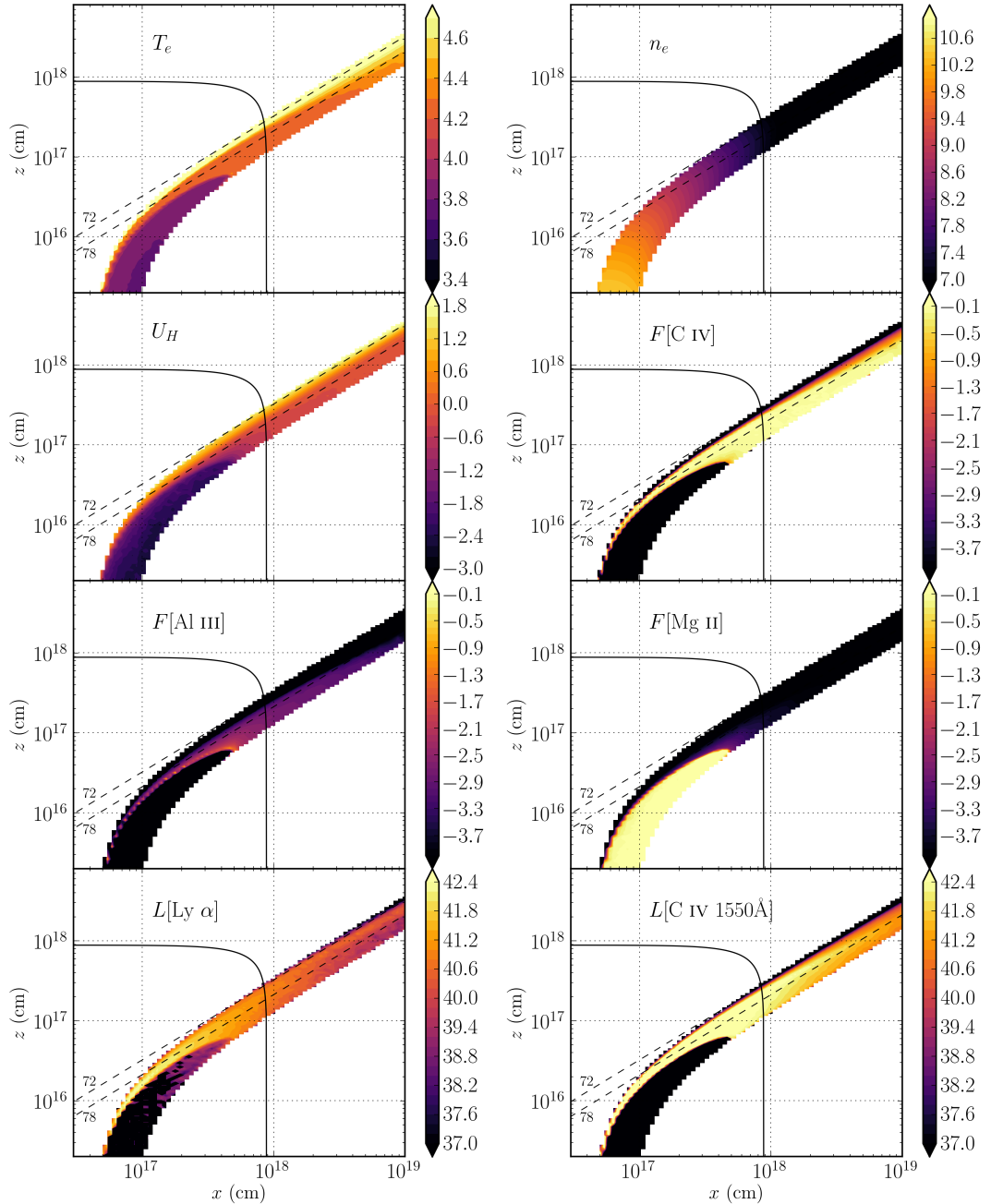


FIGURE 5.2: Contour plots showing the logarithm of some important physical properties of the outflow. The spatial scales are logarithmic and the x and z scales are not the same. Symbols are defined in the text. The solid black line marks a sphere at $1000 r_G$. The dotted lines show the 72° and 78° sightlines to the centre of the system, and illustrate that different sightlines intersect material of different ionization states. The line luminosities, L , represent the luminosity of photons escaping the Sobolev region for each line. These photons do not necessarily escape to infinity.

Fiducial Parameters	Model Value
M_{BH}	$1 \times 10^9 M_\odot$
\dot{m}_{acc}	$5 M_\odot yr^{-1} \simeq 0.2 \dot{M}_{Edd}$
α_X	-0.9
L_X	$10^{45} \text{ erg s}^{-1}$ *
$r_{disc}(\min) = r_X$	$6r_g = 8.8 \times 10^{14} \text{ cm}$
$r_{disc}(\max)$	$3400r_g = 5 \times 10^{17} \text{ cm}$
\dot{m}_{wind}	$5 M_\odot yr^{-1}$
r_{min}	$300r_g = 4.4 \times 10^{16} \text{ cm}$
r_{max}	$600r_g = 8.8 \times 10^{16} \text{ cm}$
θ_{min}	70.0°
θ_{max}	82.0°
$v_\infty(r_0)$	$v_{esc}(r_0)$
R_v	10^{19} cm^*
α	0.5*
f_V	0.01*
n_x	100
n_z	200

TABLE 5.2: Wind geometry parameters used in the fiducial model, as defined in the text and figure 1. Parameters differing from the benchmark model of H13 are highlighted with an asterisk.

One common way to quantify the ionization state of a plasma is through the ionization parameter, U_H , given by

$$U_H = \frac{4\pi}{n_H c} \int_{13.6 \text{ eV}/h}^{\infty} \frac{J_\nu d\nu}{h\nu}. \quad (5.6)$$

where ν denotes photon frequency. Shown in Fig. 5.2, the ionization parameter is a useful measure of the global ionization state, as it represents the ratio of the number density of H ionizing photons to the local H density. It is, however, a poor representation of the ionization state of species such as C IV as it encodes no information about the shape of the SED. In our case, the X-ray photons are dominant in the photoionization of the UV resonance line ions. This explains why a factor of 100 increase in X-ray luminosity requires a clumping factor of 0.01, even though the value of U_H decreases by only a factor of ~ 10 compared to H13.

The total line luminosity also increases dramatically compared to the unclumped model described by H13. This is because the denser outflow can absorb the increased X-ray luminosity without becoming over-ionized, leading to a hot plasma which produces strong collisionally excited line emission. This line emission typically emerges on the edge of the wind nearest the central source. The location of the line emitting regions is dependent on the ionization state, as well as the incident X-rays. The radii of these emitting regions is important, and can be compared to observations. The line luminosities, L , shown in the figure correspond to the luminosity in erg s^{-1} of photons escaping the

Sobolev region for each line. As shown in Fig. 5.2, the C IV 1550Å line in the fiducial model is typically formed between $100 - 1000 r_G$ ($\sim 10^{17} - 10^{18}$ cm). This is in rough agreement with the reverberation mapping results of Kaspi (2000) for the $2.6 \times 10^9 M_\odot$ quasar S5 0836+71, and also compares favourably with microlensing measurements of the size of the C IV 1550Å emission line region in the BALQSO H1413+117 (O'Dowd et al. 2015).

5.4.2 Synthetic Spectra: Comparison to Observations

Fig. 5.3 shows the synthetic spectrum in the UV from the fiducial model. To assess the ability of the synthetic spectra to match real quasar spectra, we also show *Sloan Digital Sky Survey* (SDSS) quasar composites from Reichard et al. (2003), normalised to the flux at 2000Å for low inclinations. Unfortunately, the wide variety of line profile shapes and internal trough structure in BALQSOs tends to ‘wash out’ BAL troughs in composite spectra to the extent that BALQSO composites do not resemble typical BALQSOs. Because of this, we instead compare to a *Hubble Space Telescope* STIS spectrum of the high BALnicity BALQSO PG0946+301 (Arav et al. 2000), and an SDSS spectrum of the LoBAL quasar SDSS J162901.63+453406.0, for the angles of 73° and 76° , respectively. We show a cartoon illustrating how geometric effects determine the output spectra in Fig. 5.4.

5.4.2.1 Broad absorption lines (‘BALQSO-like’ angles)

The UV spectrum is characterised by strong BAL profiles at high inclinations ($> 70^\circ$). This highlights the first success of our model: clumping allows the correct ionization state to be maintained in the presence of strong X-rays, resulting in large resonance line opacities. At the highest inclinations, the cooler, low ionization material at the base of the wind starts to intersect the line of sight. This produces multiple absorption lines in species such as Mg II, Al III and Fe II. The potential links to LoBALQSOs and FeLoBALQSOs are discussed in section 2.4.

The high ionization BAL profiles are often saturated, and the location in velocity space of the strongest absorption in the profile varies with inclination. At the lowest inclination BAL sight lines, the strongest absorption occurs at the red edge, whereas at higher inclinations (and for the strongest BALs) the trough has a sharp edge at the terminal velocity. This offers one potential explanation for the wide range of BALQSO absorption line shapes (see e.g. Trump et al. 2006; Knigge et al. 2008, Filiz Ak et al. 2014).

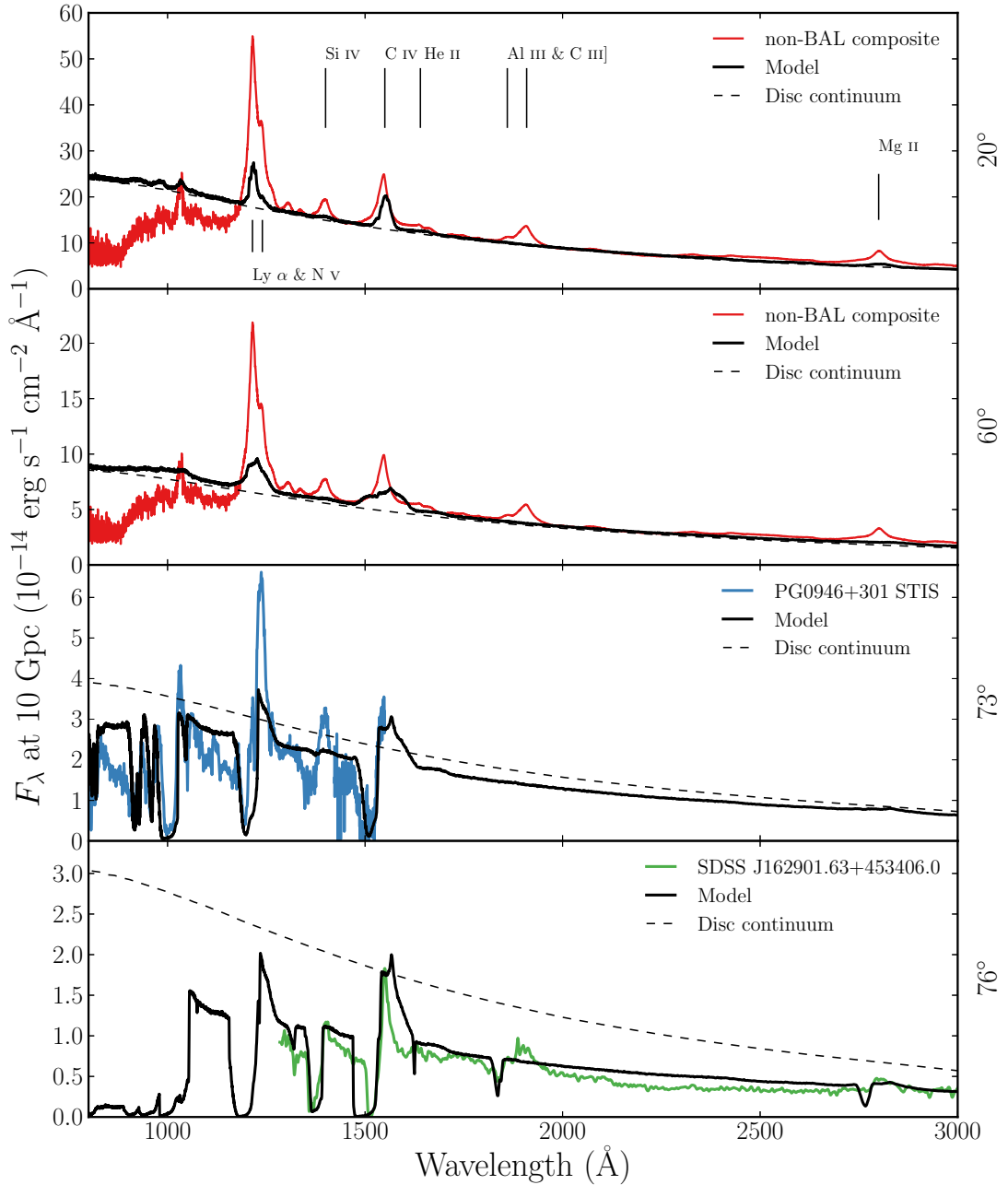


FIGURE 5.3: Synthetic spectra at four viewing angles for the fiducial model. At 20° and 60° we show a comparison to an SDSS quasar composite from Recihard et al. (2003). At 73° and 76° we show a comparison to an *HST* STIS spectrum of the high BALnicity BALQSO PG0946+301 (Arav et al. 2000), and an SDSS spectrum of the LoBAL quasar SDSS J162901.63+453406.0, respectively. The dotted line shows a disc only continuum to show the effect of the outflow on the continuum level. All the spectra are scaled to the model flux at 2000\AA , except for the *HST* STIS spectrum of PG0946+301, which is scaled to 1350\AA due to the incomplete wavelength coverage.

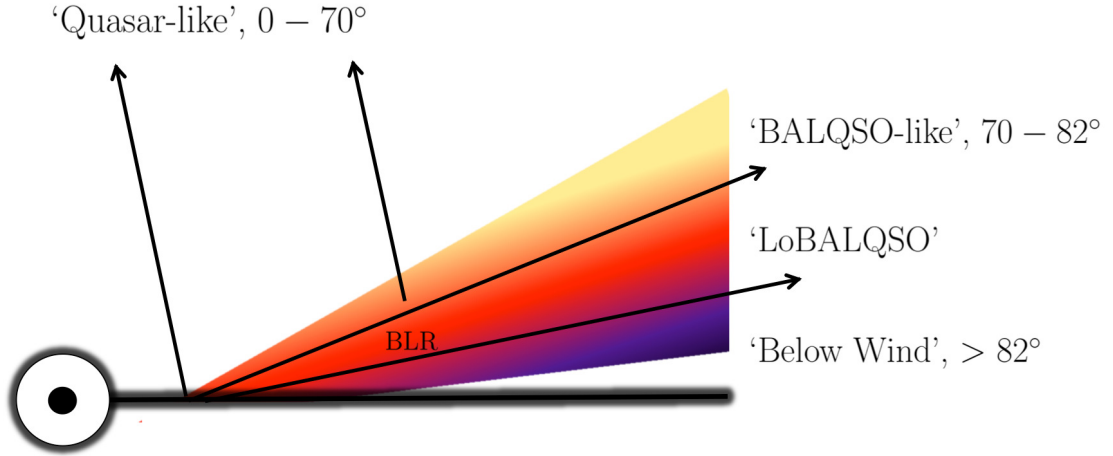


FIGURE 5.4: A cartoon describing the broad classes of sightline in the fiducial model, illustrating how geometric effects lead to the different emergent spectra. The colour gradient is approximate, but indicates the stratified ionization structure, from highly ionized (yellow) to low ionization (purple) material.

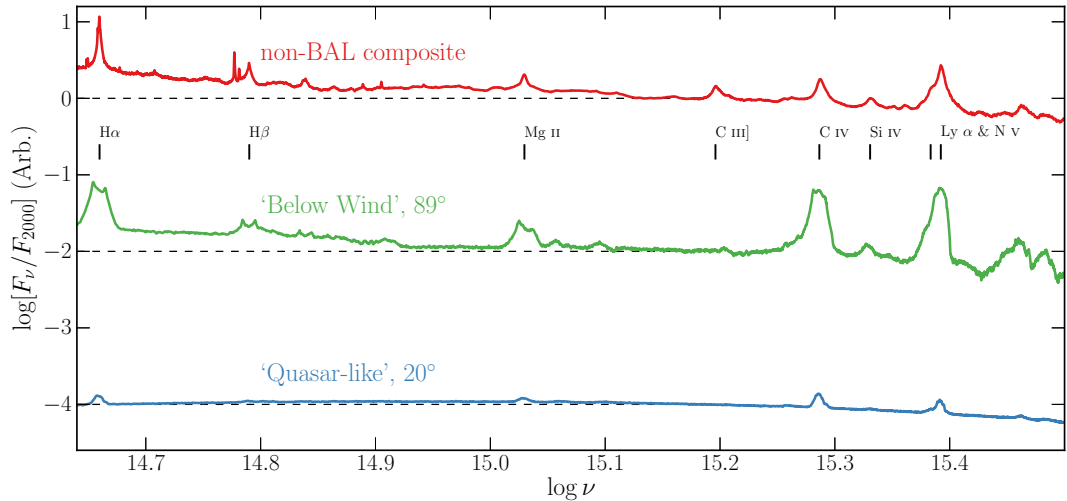


FIGURE 5.5: Synthetic spectra at two viewing angles, this time in frequency space and including the optical band, compared to the non-BAL SDSS quasar composite. The spectra are normalised to the flux at 2000Å, then an offset of 2 is applied per spectrum for clarity – the dotted lines show the zero point of $F_\nu/F_{2000\text{\AA}}$ in each case.

Property	Synthetic, 20°	Observed (S11)
$\log L[\text{C IV}]$	44.60	44.42 ± 0.32
$\log L[\text{Mg II}]$	43.92	43.54 ± 0.28
$\log(\nu L_\nu)_{1350}$	46.42	46.01 ± 0.30
$\log(\nu L_\nu)_{3000}$	46.18	45.79 ± 0.30

TABLE 5.3: Some derived spectral properties of the fiducial model, at 20°, compared to observations. The observed values are taken from the Shen et al. (2011) SDSS DR7 Quasar catalog, and correspond to mean values with standard deviations in log space from a subsample with $8.5 > \log(M_{BH}) < 9.5$ and $1.5 < \log(L_{bol}/L_{Edd}) < 0$, where the BH mass is a C IV virial estimate. Units are logarithms of values in erg s⁻¹.

The absorption profiles seen in BALQSOs are often non-black, but saturated, with flat bases to the absorption troughs (Arav et al. 1999a,b). This is usually explained either as partial covering of the continuum source or by scattered contributions to the BAL troughs, necessarily from an opacity source not co-spatial with the BAL forming region. The scattered light explanation is supported by spectropolarimetry results (Lamy and Hutsemékers 2000). Our spectra do not show non-black, saturated profiles. We find black, saturated troughs at angles $i > 73^\circ$, and the BALs are non-saturated at lower inclinations. The reasons for this are inherent in the construction of our model. First, the microclumping assumption does not allow for porosity in the wind, meaning that it does not naturally produce a partial covering absorber. To allow this, an alternative approach such as *macroclumping* would be required (e.g. Hamann et al. 2008; Šurlan et al. 2012). Second, our wind does not have a significant scattering contribution along sightlines which do not pass through the BAL region, meaning that any scattered component to the BAL troughs is absorbed by line opacity. This suggests that either the scattering cross-section of the wind must be increased (with higher mass loss rates or covering factors), or that an additional source of electron opacity is required, potentially in a polar direction above the disc. We note the scattering contribution from plasma in polar regions is significant in some ‘outflow-from-inflow’ simulations (Kurosawa and Proga 2009; Sim et al. 2012).

5.4.2.2 Broad emission lines (‘quasar-like’ angles)

Unlike H13, we now find significant collisionally excited line emission emerges at low inclinations in the synthetic spectra, particular in the C IV and N V lines. We also find a strong Ly α line and weak He II 1640Å line as a result of our improved treatment of recombination using macro-atoms. In the context of unification, this is a promising result, and shows that a biconical wind can produce significant emission at ‘quasar-like’ angles. To demonstrate this further, we show line luminosities and monochromatic continuum luminosities from the synthetic spectra in Table 5.3. These are compared

to mean values from a subsample of the SDSS DR7 quasar catalog (Shen et al. 2011) with BH mass and Eddington fraction estimates similar to the fiducial model values (see caption). The spectra do not contain the strong C III] 1909Å line seen in the quasar composite spectra, but this is due to a limitation of our current treatment of C; semi-forbidden (intercombination) lines are not included in our modelling.

In Fig. 5.5, we show an F_ν spectrum with broader waveband coverage that includes the optical, showing that our synthetic spectra also exhibit H α and H β emission. In this panel, we include a low inclination and also a very high inclination spectrum, which looks underneath the wind cone. This model shows strong line emission with very similar widths and line ratios to the quasar composites, and the Balmer lines are double peaked, due to velocity projection effects. Such double-peaked lines are seen in so-called ‘disc emitter’ systems (e.g. Eracleous and Halpern 1994) but not the majority of AGN. The line equivalent widths (EWs) increase at high inclination due to a weakened continuum from wind attenuation, disc foreshortening and limb darkening. This effect also leads to a redder continuum slope, as seen in quasars, which is due to Balmer continuum and Balmer and Fe II line emission. This extreme 89° viewing angle cannot represent a typical quasar within a unified model, but does show that a model such as this can naturally reproduce quasar emission lines if the emissivity of the wind is increased *with respect to the disc continuum*. In addition, it neatly demonstrates how a stratified outflow can naturally reproduce the range of ionization states seen in quasars.

Despite a number of successes, there are some properties of the synthetic spectra that are at odds with the observations. First, the ratios of the EW of the Ly α and Mg II 2800Å lines to the EW of C IV 1550Å are much lower than in the composite spectra. Similar problems have also been seen in simpler photoionization models for the BLR (Netzer 1990). It may be that a larger region of very dense ($n_e \sim 10^{10}\text{cm}^{-3}$) material is needed, which could correspond to a disc atmosphere or ‘transition region’ (see e.g. Murray et al. 1995; Knigge et al. 1997). While modest changes to geometry may permit this, the initial grid search did not find a parameter space in which the Ly α or Mg II EWs were significantly higher (see section 5.4.5). Second, we find that EWs increase with inclination (see Fig. 5.3 and Fig. 5.5; also Fig. 5.7), to the extent that, even though significantly denser models can match the line EWs fairly well at low inclinations, they will then possess overly strong red wings to the BAL P-Cygni profiles at high inclinations. The fact that the EW increase in our model are directly related to limb-darkening and foreshortening of the continuum. This appears to contradict observations, which show remarkably uniform emission line properties in quasars and BALQSOs (Weymann et al. 1991; DiPompeo et al. 2012). The angular distribution of the disc continuum and line emission is clearly crucially important in determining the

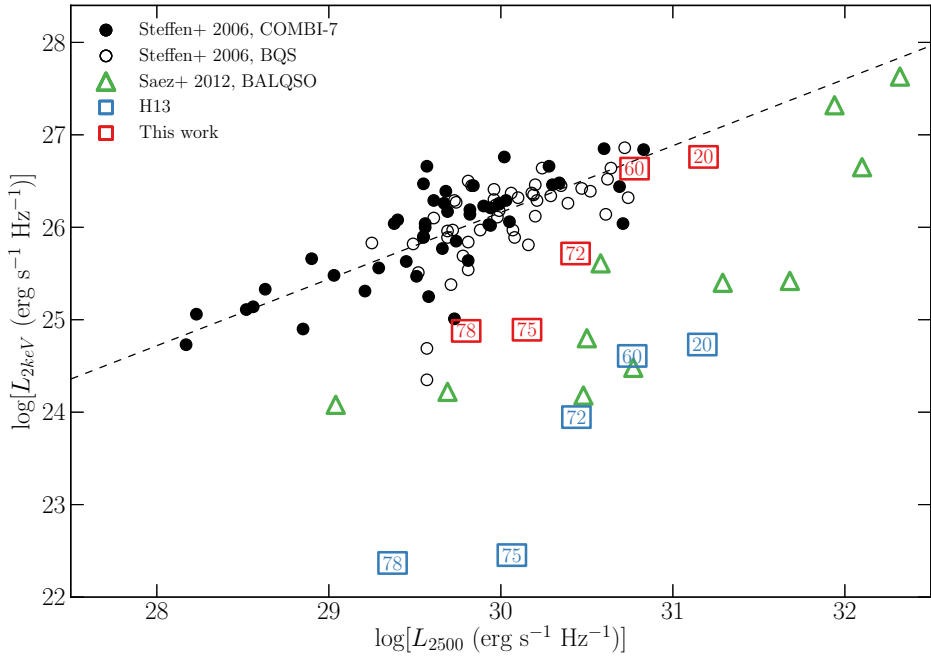


FIGURE 5.6: X-ray (2 keV) luminosity of the our clumped model (red squares) and the H13 model (blue squares), plotted against monochromatic luminosity at 2500Å. The points are labeled according to inclination; angles $> 70^\circ$ correspond to BALs in our scheme (see figure 4). Also plotted are measurements from the COMBI-7 AGN and the BQS samples (Steffen et al. 2006) and the Saez et al. (2012) sample of BALQSOs. The dotted line shows the best fit relation for non-BALQSOs from Steffen et al. (2006).

emergent broad line EWs, as suggested by, e.g., the analysis of Risaliti et al. (2011). We shall explore this question further in a future study.

5.4.3 X-ray Properties

The main motivation for adding clumping to the model was to avoid over-ionization of the wind in the presence of strong X-rays. Having verified that strong BALs appear in the synthetic spectra, it is also important to assess whether the X-ray properties of this fiducial model agree well with quasar and BALQSO samples for the relevant inclinations.

Fig. 5.6 shows the emergent monochromatic luminosity (L_ν) at 2 keV and plotted against L_ν at 2500Å for a number of different viewing angles in our model. The monochromatic luminosities are calculated from the synthetic spectra and thus include the effects of wind reprocessing and attenuation. In addition to model outputs, we also show the BALQSO sample of Saez et al. (2012) and luminous AGN and quasar samples from Steffen et al. (2006). The best fit relation from Steffen et al. (2006) is also shown. For low inclination, ‘quasar-like’ viewing angles, we now find excellent agreement with AGN

samples. The slight gradient from 20° to 60° in our models is caused by a combination of disc foreshortening and limb-darkening (resulting in a lower L_{2500} for higher inclinations), and the fact that the disk is opaque, and thus the X-ray source subtends a smaller solid angle at high inclinations (resulting in a lower L_{2keV} for higher inclinations).

The high inclination, ‘BALQSO-like’ viewing angles show moderate agreement with the data, and are X-ray weak due to bound-free absorption and electron scattering in the wind. Typically, BALQSOs show strong X-ray absorption with columns of $N_H \sim 10^{23} \text{ cm}^{-2}$ (Green and Mathur 1996; Mathur et al. 2000; Green et al. 2001; Grupe et al. 2003). This is often cited as evidence that the BAL outflow is shielded from the X-ray source, especially as sources with strong X-ray absorption tend to exhibit deep BAL troughs and high outflow velocities (Brandt et al. 2000; Laor and Brandt 2002; Gallagher et al. 2006). Our results imply that the clumpy BAL outflow itself can be responsible for the strong X-ray absorption, and supports Hamann et al.’s (2013) suggestion that geometric effects explain the weaker X-ray absorption in mini-BALs compared to BALQSOs.

5.4.4 LoBALs and Ionization Stratification

At high inclinations, the synthetic spectra exhibit blue-shifted BALs in Al III and Mg II—the absorption lines seen in LoBALQSOs, and we even see absorption in Fe II at the highest inclinations. Line profiles in velocity space for C IV, Al III and Mg II, are shown in Fig. 5.7 for a range of BALQSO viewing angles. We find that ionization stratification of the wind causes lower ionization material to have a smaller covering factor, as demonstrated by figures 5.2 and 5.7. This confirms the behaviour expected from a unification model such as Elvis (2000). LoBALs are only present at viewing angles close to edge-on ($i > 75^\circ$), as predicted by polarisation results (Brotherton et al. 1997). As observed in a BALQSO sample by Filiz Ak et al. (2014), we find that BAL troughs are wider and deeper when low ionization absorption features are present, and high ionization lines have higher blue-edge velocities than the low ionization species. There is also a correlation between the strength of LoBAL features and the amount of continuum attenuation at that sightline, particularly blueward of the Lyman edge as the low ionization base intersects the line-of-sight. A model such as this therefore predicts that LoBALQSOs and FeLoBALQSOs have stronger Lyman edge absorption and are more Compton-thick than HiBALQSOs and Type 1 quasars. An edge-on scenario also offers a potential explanation for the rarity of LoBAL and FeLoBAL quasars, due to a foreshortened and attenuated continuum, although BAL fraction inferences are fraught with complex selection effects (Goodrich 1997; Krolik and Voit 1998).

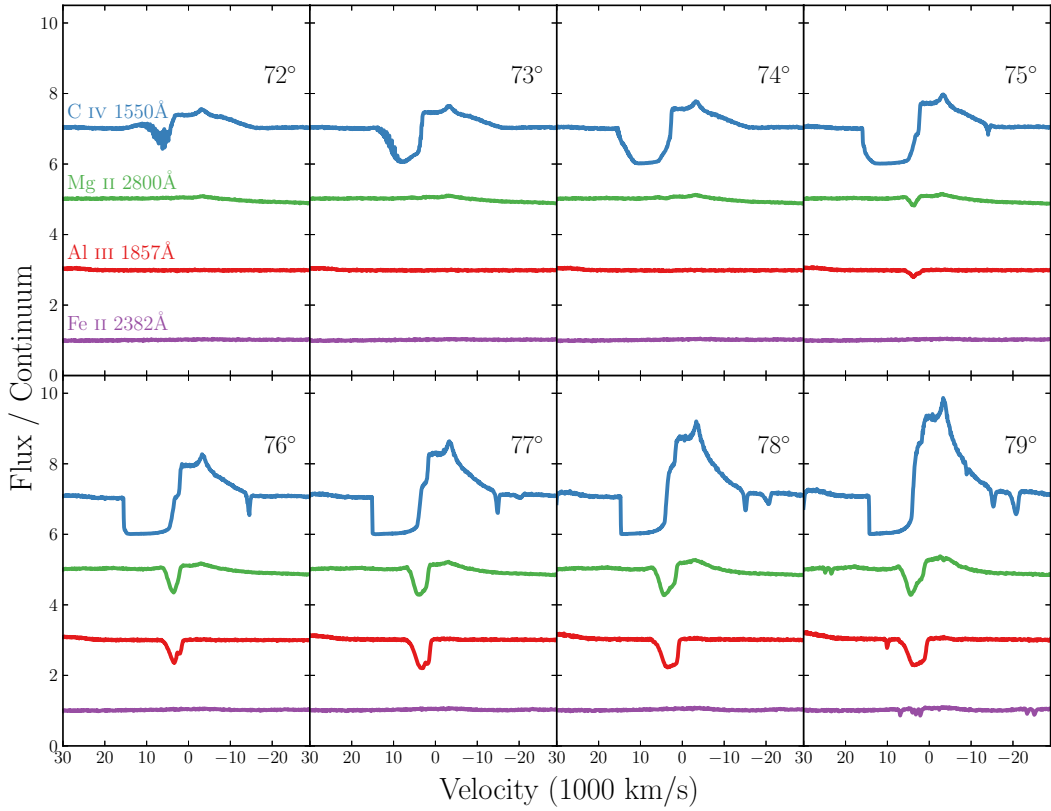


FIGURE 5.7: C IV, Mg II, Al III and Fe II line profiles for viewing angles from $72 - 79^\circ$. The profiles are plotted relative to the local continuum with an offset applied for clarity. Lower ionization profiles appear at a subset of high inclinations, compared to the ubiquitous C IV profile.

5.4.5 Parameter Sensitivity

Having selected an individual fiducial model from the simulation grid, it is important to briefly explore how specialised this model is, and how small parameter changes can affect the synthetic spectra. Fig. 5.8 shows the EW at a low inclination, and *BI* at a high inclination for the simulation grid. A few conclusions can be drawn from this plot straight away. First, we find that almost all the models with $f_V = 0.1$ are over-ionized, and fail to produce strong C IV BALs or emission lines. Second, we find that it is difficult to significantly increase line emission while keeping the luminosity and mass loss rate of the system fixed. We show an additional point on figure 7 corresponding to a model with an order of magnitude higher X-ray luminosity and double the mass loss rate. As expected, this results in far higher line EWs, but fails to produce BALs because the collisionally excited emission swamps the BAL profile. In addition, this model would lie well above the expected $L_{2kev} - L_{2500}$ relation in figure 5. Such a high X-ray luminosity could therefore not be the cause of the strong line emission seen in *all* Type 1 quasars.

The parameter search presented here is by no means exhaustive, and we may be limited

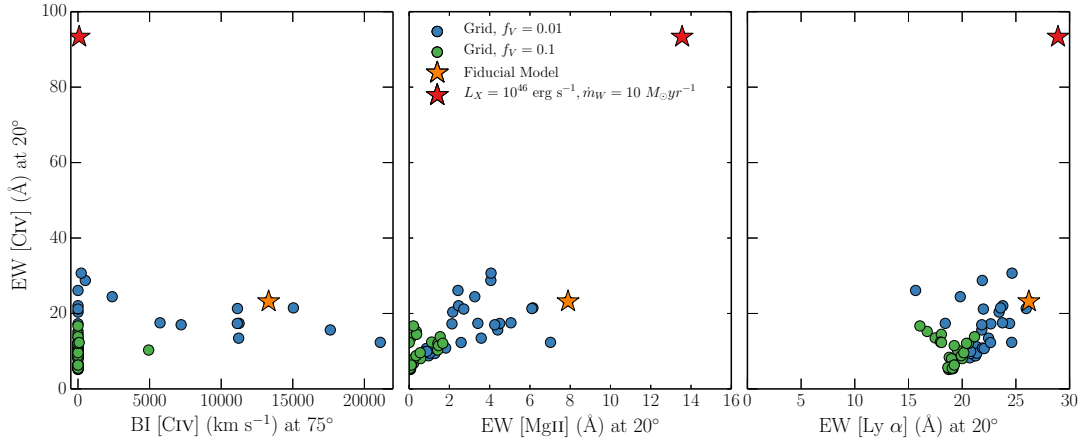


FIGURE 5.8: The EW of the C IV 1550Å line at 20° plotted against a) the BI of C IV 1550Å at 75°, b) the EW of the Mg II 2800Å line at 20° and c) the EW of Ly α at 20°. The circles correspond to the simulation grid for two different values of f_V , and the fiducial model is marked with an orange star. We also show a higher X-ray luminosity model and a higher mass loss rate with a red star.

by the specific parameterisation of the outflow kinematics we have used. Nevertheless, we suggest that the angular distribution of both the line and continuum emission is perhaps the crucial aspect to understand. With this in mind, obtaining reliable orientation indicators appears to be a crucial observational task if we are to further our understanding of BAL outflows and their connection, or lack thereof, to the broad line region.

5.5 Summary And Conclusions

We have carried out MCRT simulations using a simple prescription for a biconical disc wind, with the aim of expanding on the work of H13. To do this, we introduced two main improvements: First, we included a simple treatment of clumping, and second, we improved the modelling of recombination lines by treating H and He as ‘macro-atoms’. Having selected a fiducial model from an initial simulation grid, we assessed the viability of such a model for geometric unification of quasars, and found the following main points:

1. Clumping moderates the ionization state sufficiently to allow for the formation of strong UV BALs while agreeing well with the X-ray properties of luminous AGN and quasars.
2. A clumpy outflow model naturally reproduces the range of ionization states expected in quasars, due to its stratified density and temperature structure. LoBAL line profiles are seen at a subset of viewing angles, and Fe II absorption is seen at particularly high inclinations.

3. The synthetic spectra show Ly α line and weak He II 1640Å line as a result of our improved treatment of recombination using macro-atoms. We also see Balmer emission lines and a Balmer recombination continuum in the optical spectrum, but this is only really significant at high inclination where the continuum is suppressed.
4. The higher X-ray luminosity causes a significant increase in the strength of the collisionally excited emission lines produced by the model. However, the equivalent-width ratios of the emission lines do not match observations, suggesting that a greater volume of dense ($n_e \sim 10^{10} \text{ cm}^{-3}$) material may be required.
5. The line EWs in the synthetic spectra increase with inclination. BAL and non-BAL quasar composites have comparable EWs, so our model fails to reproduce this behaviour. If the BLR emits fairly isotropically from a foreshortened, limb-darkened accretion disc it is not possible to achieve line ratios at low inclinations that are comparable to those at high inclinations. We suggest that understanding the angular distribution of line and continuum emission is a crucial question for theoretical models.

Our work confirms a number of expected outcomes from a geometric unification model, and suggests that a simple biconical geometry such as this can come close to explaining much of the phenomenology of quasars. However, our conclusions pose some challenges to a picture in which BALQSOs are explained by an *equatorial* wind rising from a classical thin disc, and suggest the angular distribution of emission is important to understand if this geometry is to be refuted or confirmed. We suggest that obtaining reliable observational orientation indicators and exploring a wider parameter space of outflow geometries in simulations are obvious avenues for future work.

Bibliography

- Allen, J. T., P. C. Hewett, N. Maddox, G. T. Richards, and V. Belokurov
2011. A strong redshift dependence of the broad absorption line quasar fraction.
MNRAS, 410:860–884.
- Antonucci, R. R. J. and J. S. Miller
1985. Spectropolarimetry and the nature of NGC 1068. *ApJ*, 297:621–632.
- Arav, N., R. H. Becker, S. A. Laurent-Muehleisen, M. D. Gregg, R. L. White, M. S. Brotherton, and M. de Kool
1999a. What Determines the Depth of Broad Absorption Lines? Keck HIRES Observations of BALQSO 1603+3002. *ApJ*, 524:566–571.
- Arav, N., K. T. Korista, M. de Kool, V. T. Junkkarinen, and M. C. Begelman
1999b. Hubble Space Telescope Observations of the Broad Absorption Line Quasar PG 0946+301. *ApJ*, 516:27–46.
- Arévalo, P. and P. Uttley
2006. Investigating a fluctuating-accretion model for the spectral-timing properties of accreting black hole systems. *MNRAS*, 367:801–814.
- Badnell, N. R.
2006. Radiative Recombination Data for Modeling Dynamic Finite-Density Plasmas. *ApJs*, 167:334–342.
- Badnell, N. R., M. A. Bautista, K. Butler, F. Delahaye, C. Mendoza, P. Palmeri, C. J. Zeippen, and M. J. Seaton
2005. Updated opacities from the Opacity Project. *MNRAS*, 360:458–464.
- Baptista, R., C. Silveira, J. E. Steiner, and K. Horne
2000. Spatially resolved spectra of the accretion disc of the nova-like variable UU Aquarii. *MNRAS*, 314:713–726.
- Bartlett, E.
2013. *High mass X-ray binaries in the Milky Way and beyond: a multiwavelength temporal and spectroscopic study*. PhD thesis, University of Southampton.

- Begelman, M., M. de Kool, and M. Sikora
1991. Outflows driven by cosmic-ray pressure in broad absorption line QSOs. *ApJ*, 382:416–432.
- Begelman, M. C., C. F. McKee, and G. A. Shields
1983. Compton heated winds and coronae above accretion disks. I Dynamics. *ApJ*, 271:70–88.
- Belloni, T., ed.
2010. *The Jet Paradigm*, volume 794 of *Lecture Notes in Physics*, Berlin Springer Verlag.
- Benz, A. O., E. Fuerst, and A. L. Kiplinger
1983. First detection of radio emission from a dwarf nova. *Nature*, 302:45.
- Beuermann, K., U. Stasiewski, and A. D. Schwope
1992. Phase-resolved spectroscopy of the novalike cataclysmic variable RW Sextantis. *A&A*, 256:433–437.
- Beuermann, K. and H.-C. Thomas
1990. Detection of emission lines from the secondary star in IX Velorum (=CPD-48 deg 1577). *A&A*, 230:326–338.
- Blandford, R. D. and D. G. Payne
1982. Hydromagnetic flows from accretion discs and the production of radio jets. *MNRAS*, 199:883–903.
- Bondi, H.
1952. On spherically symmetrical accretion. *MNRAS*, 112:195.
- Bondi, H. and F. Hoyle
1944. On the mechanism of accretion by stars. *MNRAS*, 104:273.
- Brandt, W. N., A. Laor, and B. J. Wills
2000. On the Nature of Soft X-Ray Weak Quasi-stellar Objects. *ApJ*, 528:637–649.
- Brotherton, M. S., H. D. Tran, W. van Breugel, A. Dey, and R. Antonucci
1997. Spectropolarimetry of FIRST Broad Absorption Line Quasars. *ApJ Letters*, 487:L113–L116.
- Capellupo, D. M., F. Hamann, and T. A. Barlow
2014. A variable P v broad absorption line and quasar outflow energetics. *MNRAS*, 444:1893–1900.

- Capellupo, D. M., F. Hamann, J. C. Shields, P. Rodríguez Hidalgo, and T. A. Barlow
2011. Variability in quasar broad absorption line outflows - I. Trends in the short-term
versus long-term data. *MNRAS*, 413:908–920.
- Capellupo, D. M., F. Hamann, J. C. Shields, P. Rodríguez Hidalgo, and T. A. Barlow
2012. Variability in quasar broad absorption line outflows - II. Multi-epoch monitoring
of Si IV and C IV broad absorption line variability. *MNRAS*, 422:3249–3267.
- Carlberg, R. G.
1980. The instability of radiation-driven stellar winds. *ApJ*, 241:1131–1140.
- Cassidy, I. and D. J. Raine
1996. The broad line regions of NGC 4151. *A&A*, 310:49–65.
- Cassinelli, J. P.
1979. Stellar winds. *ARAA*, 17:275–308.
- Cohen, M. H., P. M. Ogle, H. D. Tran, R. C. Vermeulen, J. S. Miller, R. W. Goodrich,
and A. R. Martel
1995. Spectropolarimetry of Two Broad Absorption Line Quasars with the W. M.
Keck Telescope. *ApJ Letters*, 448:L77.
- Cohen, R. D., R. C. Puetter, R. J. Rudy, T. B. Ake, and C. B. Foltz
1986. Variability of Markarian 1018 - Seyfert 1.9 to Seyfert 1. *ApJ*, 311:135–141.
- Coppejans, D. L., E. G. Körding, J. C. A. Miller-Jones, M. P. Rupen, C. Knigge, G. R.
Sivakoff, and P. J. Groot
2015. Novalike cataclysmic variables are significant radio emitters. *MNRAS*, 451:3801–
3813.
- Cordova, F. A. and K. O. Mason
1982. High-velocity winds from a dwarf nova during outburst. *ApJ*, 260:716–721.
- Cunto, W., C. Mendoza, F. Ochsenbein, and C. J. Zeippen
1993. Topbase at the CDS. *A&A*, 275:L5.
- de Kool, M. and M. C. Begelman
1995. Radiation Pressure–driven Magnetic Disk Winds in Broad Absorption Line
Quasi-stellar Objects. *ApJ*, 455:448.
- Denney, K. D., G. De Rosa, K. Croxall, A. Gupta, M. C. Bentz, M. M. Fausnaugh, C. J.
Grier, P. Martini, S. Mathur, B. M. Peterson, R. W. Pogge, and B. J. Shappee
2014. The Typecasting of Active Galactic Nuclei: Mrk 590 no Longer Fits the Role.
ApJ, 796:134.

- Dere, K. P.
2007. Ionization rate coefficients for the elements hydrogen through zinc. *A&A*, 466:771–792.
- Dere, K. P., E. Landi, H. E. Mason, B. C. Monsignori Fossi, and P. R. Young
1997. CHIANTI - an atomic database for emission lines. *A&As*, 125:149–173.
- Dhillon, V. S.
1996. The Nova-like variables. In *IAU Colloq. 158: Cataclysmic Variables and Related Objects*, A. Evans and J. H. Wood, eds., volume 208 of *Astrophysics and Space Science Library*, P. 3.
- Dhillon, V. S. and R. G. M. Rutten
1995. Spectropolarimetry of the nova-like variable V 1315 Aquilae. *MNRAS*, 277:777–780.
- DiPompeo, M. A., M. S. Brotherton, S. L. Cales, and J. C. Runnoe
2012. The rest-frame ultraviolet properties of radio-loud broad absorption line quasars. *MNRAS*, 427:1135–1152.
- Drew, J. and F. Verbunt
1985. Investigation of a wind model for cataclysmic variable ultraviolet resonance line emission. *MNRAS*, 213:191–213.
- Edelson, R., J. M. Gelbord, K. Horne, I. M. McHardy, B. M. Peterson, P. Arévalo, A. A. Breeveld, G. De Rosa, P. A. Evans, M. R. Goad, G. A. Kriss, W. N. Brandt, N. Gehrels, D. Grupe, J. A. Kennea, C. S. Kochanek, J. A. Nousek, I. Papadakis, M. Siegel, D. Starkey, P. Uttley, S. Vaughan, S. Young, A. J. Barth, M. C. Bentz, B. J. Brewer, D. M. Crenshaw, E. Dalla Bontà, A. De Lorenzo-Cáceres, K. D. Denney, M. Dietrich, J. Ely, M. M. Fausnaugh, C. J. Grier, P. B. Hall, J. Kaastra, B. C. Kelly, K. T. Korista, P. Lira, S. Mathur, H. Netzer, A. Pancoast, L. Pei, R. W. Pogge, J. S. Schimoia, T. Treu, M. Vestergaard, C. Villforth, H. Yan, and Y. Zu
2015. Space Telescope and Optical Reverberation Mapping Project. II. Swift and HST Reverberation Mapping of the Accretion Disk of NGC 5548. *ApJ*, 806:129.
- Edge, D. O., J. R. Shakeshaft, W. B. McAdam, J. E. Baldwin, and S. Archer
1959. A survey of radio sources at a frequency of 159 Mc/s. *MmRA*, 68:37–60.
- Ehman, J. R., R. S. Dixon, and J. D. Kraus
1970. The Ohio survey between declinations of 0 and 36 south. *AJ*, 75:351–506.
- Ekers, J. A.
1969. The Parkes catalogue of radio sources, declination zone +20 to -90 . *Australian Journal of Physics Astrophysical Supplement*, 7.

- Elitzur, M.
2012. On the Unification of Active Galactic Nuclei. *ApJ Letters*, 747:L33.
- Elitzur, M., L. C. Ho, and J. R. Trump
2014. Evolution of broad-line emission from active galactic nuclei. *MNRAS*, 438:3340–3351.
- Elvis, M.
2000. A Structure for Quasars. *ApJ*, 545:63–76.
- Emmering, R. T., R. D. Blandford, and I. Shlosman
1992. Magnetic acceleration of broad emission-line clouds in active galactic nuclei. *ApJ*, 385:460–477.
- Eracleous, M. and J. P. Halpern
1994. Doubled-peaked emission lines in active galactic nuclei. *ApJs*, 90:1–30.
- Fabian, A. C.
2012. Observational Evidence of Active Galactic Nuclei Feedback. *ARA&A*, 50:455–489.
- Fath, E. A.
1909. The spectra of some spiral nebulae and globular star clusters. *Lick Observatory Bulletin*, 5:71–77.
- Fender, R. P.
2001. Powerful jets from black hole X-ray binaries in low/hard X-ray states. *MNRAS*, 322:31–42.
- Ferland, G. J., R. L. Porter, P. A. M. van Hoof, R. J. R. Williams, N. P. Abel, M. L. Lykins, G. Shaw, W. J. Henney, and P. C. Stancil
2013. The 2013 Release of Cloudy. *RMXAA*, 49:137–163.
- Filiz Ak, N., W. N. Brandt, P. B. Hall, D. P. Schneider, J. R. Trump, S. F. Anderson, F. Hamann, A. D. Myers, I. Pâris, P. Petitjean, N. P. Ross, Y. Shen, and D. York
2014. The Dependence of C IV Broad Absorption Line Properties on Accompanying Si IV and Al III Absorption: Relating Quasar-wind Ionization Levels, Kinematics, and Column Densities. *ApJ*, 791:88.
- Frank, J., A. King, and D. Raine
1992. *Accretion power in astrophysics*.
- Frank, J. and A. R. King
1981. A standard accretion disc model for RW Tri. *MNRAS*, 195:227–234.

- Gallagher, S. C., W. N. Brandt, G. Chartas, R. Priddey, G. P. Garmire, and R. M. Sambruna
2006. An Exploratory Chandra Survey of a Well-defined Sample of 35 Large Bright Quasar Survey Broad Absorption Line Quasars. *ApJ*, 644:709–724.
- Ganguly, R. and M. S. Brotherton
2008. On the Fraction of Quasars with Outflows. *ApJ*, 672:102–107.
- Ganguly, R., K. R. Sembach, T. M. Tripp, B. D. Savage, and B. P. Wakker
2006. High-Resolution Absorption Spectroscopy of Multiphase, High-Metallicity Gas Associated with the Luminous Quasar HE 0226-4110. *ApJ*, 645:868–889.
- Ghosh, K. K. and B. Punsly
2007. The Physical Nature of Polar Broad Absorption Line Quasars. *ApJ Letters*, 661:L139–L142.
- Goodrich, R. W.
1997. On the Fraction of Broad Absorption Line Quasi-stellar Objects. *ApJ*, 474:606–611.
- Goodrich, R. W. and J. S. Miller
1995. Polarization Clues to the Structure of Broad Absorption Line Quasi-stellar Objects. *ApJ Letters*, 448:L73.
- Green, P. J., T. L. Aldcroft, S. Mathur, B. J. Wilkes, and M. Elvis
2001. A Chandra Survey of Broad Absorption Line Quasars. *ApJ*, 558:109–118.
- Green, P. J. and S. Mathur
1996. Broad Absorption Line Quasars Observed by the ROSAT PSPC. *ApJ*, 462:637.
- Greenstein, J. L. and J. B. Oke
1982. RW Sextantis, a disk with a hot, high-velocity wind. *ApJ*, 258:209–216.
- Groot, P. J., R. G. M. Rutten, and J. van Paradijs
2004. A spectrophotometric study of RW Trianguli. *A&A*, 417:283–291.
- Grupe, D., S. Mathur, and M. Elvis
2003. XMM-Newton Observations of Two Broad Absorption Line QSOs: Q1246-057 and SBS 1542+541. *AJ*, 126:1159–1166.
- Gültekin, K., D. O. Richstone, K. Gebhardt, T. R. Lauer, S. Tremaine, M. C. Aller, R. Bender, A. Dressler, S. M. Faber, A. V. Filippenko, R. Green, L. C. Ho, J. Kormendy, J. Magorrian, J. Pinkney, and C. Siopis
2009. The M- σ and M-L Relations in Galactic Bulges, and Determinations of Their Intrinsic Scatter. *ApJ*, 698:198–221.

- Hamann, F., G. Chartas, S. McGraw, P. Rodriguez Hidalgo, J. Shields, D. Capellupo, J. Charlton, and M. Eracleous
2013. Extreme-velocity quasar outflows and the role of X-ray shielding. *MNRAS*, 435:133–148.
- Hamann, W.-R. and L. Koesterke
1998. Spectrum formation in clumped stellar winds: consequences for the analyses of Wolf-Rayet spectra. *A&A*, 335:1003–1008.
- Hamann, W.-R., L. M. Oschinova, and A. Feldmeier
2008. Spectrum formation in clumpy stellar winds. In *Clumping in Hot-Star Winds*, W.-R. Hamann, A. Feldmeier, and L. M. Oschinova, eds., P. 75.
- Häring, N. and H.-W. Rix
2004. On the Black Hole Mass-Bulge Mass Relation. *ApJ Letters*, 604:L89–L92.
- Harrop-Allin, M. K. and B. Warner
1996. Accretion disc radii in eclipsing cataclysmic variables. *MNRAS*, 279:219–228.
- Hartley, L. E., J. R. Murray, J. E. Drew, and K. S. Long
2005. Spiral waves and the secondary star in the nova-like variable V3885 Sgr. *MNRAS*, 363:285–292.
- Hassall, B. J. M.
1985. A superoutburst of the dwarf nova EK Trianguli Australis. *MNRAS*, 216:335–352.
- Haug, K.
1987. Continuum distributions and line profiles of UX UMa-type novalike systems. *AP&SS*, 130:91–102.
- Hazard, C., M. B. Mackey, and A. J. Shimmins
1963. Investigation of the Radio Source 3C 273 By The Method of Lunar Occultations. *Nature*, 197:1037–1039.
- Heap, S. R., A. Boggess, A. Holm, D. A. Klinglesmith, W. Sparks, D. West, C. C. Wu, A. Boksenberg, A. Willis, R. Wilson, F. Macchetto, P. O. Selvelli, D. Stickland, J. L. Greenstein, J. B. Hutchings, A. B. Underhill, R. Viotti, and J. A. J. Whelan
1978. IUE observations of hot stars - HZ43, BD +75 deg 325, NGC 6826, SS Cygni, Eta Carinae. *Nature*, 275:385–388.
- Heil, L. M., S. Vaughan, and P. Uttley
2012. The ubiquity of the rms-flux relation in black hole X-ray binaries. *MNRAS*, 422:2620–2631.

- Hessman, F. V., E. L. Robinson, R. E. Nather, and E.-H. Zhang
1984. Time-resolved spectroscopy of SS Cygni at minimum and maximum light. *ApJ*, 286:747–759.
- Higginbottom, N., C. Knigge, K. S. Long, S. A. Sim, and J. H. Matthews
2013. A simple disc wind model for broad absorption line quasars. *MNRAS*, 436:1390–1407.
- Higginbottom, N., D. Proga, C. Knigge, K. S. Long, J. H. Matthews, and S. A. Sim
2014. Line-driven Disk Winds in Active Galactic Nuclei: The Critical Importance of Ionization and Radiative Transfer. *ApJ*, 789:19.
- Hillier, D. J.
1991. The effects of electron scattering and wind clumping for early emission line stars. *A&A*, 247:455–468.
- Hillier, D. J. and D. L. Miller
1999. Constraints on the Evolution of Massive Stars through Spectral Analysis. I. The WC5 Star HD 165763. *ApJ*, 519:354–371.
- Hogg, J. D. and C. Reynolds
2015. Testing the Propagating Fluctuations Model with a Long, Global Accretion Disk Simulation. *ArXiv e-prints*.
- Honeycutt, R. K., E. M. Schlegel, and R. H. Kaitchuck
1986. Evidence for a bipolar wind in the cataclysmic variable PG 1012-029. *ApJ*, 302:388–402.
- Hönig, S. F., M. Kishimoto, K. R. W. Tristram, M. A. Prieto, P. Gandhi, D. Asmus, R. Antonucci, L. Burtscher, W. J. Duschl, and G. Weigelt
2013. Dust in the Polar Region as a Major Contributor to the Infrared Emission of Active Galactic Nuclei. *ApJ*, 771:87.
- Horne, K. and T. R. Marsh
1986. Emission line formation in accretion discs. *MNRAS*, 218:761–773.
- Hoyle, F. and R. A. Lyttleton
1939. The effect of interstellar matter on climatic variation. *Proceedings of the Cambridge Philosophical Society*, 35:405.
- Hubeny, I. and T. Lanz
1995. Non-LTE line-blanketed model atmospheres of hot stars. 1: Hybrid complete linearization/accelerated lambda iteration method. *ApJ*, 439:875–904.

- Idan, I., J.-P. Lasota, J.-M. Hameury, and G. Shaviv
2010. Accretion-disc model spectra for dwarf-nova stars. *A&A*, 519:A117.
- Kafka, S. and R. K. Honeycutt
2004. Detecting Outflows from Cataclysmic Variables in the Optical. *AJ*, 128:2420–2429.
- Kellermann, K. I., R. Sramek, M. Schmidt, D. B. Shaffer, and R. Green
1989. VLA observations of objects in the Palomar Bright Quasar Survey. *AJ*, 98:1195–1207.
- Kerzendorf, W. E. and S. A. Sim
2014. A spectral synthesis code for rapid modelling of supernovae. *MNRAS*, 440:387–404.
- King, A.
2003. Black Holes, Galaxy Formation, and the $M_{BH}-\sigma$ Relation. *ApJ Letters*, 596:L27–L29.
- King, A.
2005. The AGN-Starburst Connection, Galactic Superwinds, and $M_{BH}-\sigma$. *ApJ Letters*, 635:L121–L123.
- Knigge, C. and J. E. Drew
1997. Eclipse Mapping of the Accretion Disk Wind in the Cataclysmic Variable UX Ursae Majoris. *ApJ*, 486:445–456.
- Knigge, C., K. S. Long, W. P. Blair, and R. A. Wade
1997. Disks, Winds, and Veiling Curtains: Dissecting the Ultraviolet Spectrum of the Dwarf Nova Z Camelopardalis in Outburst. *ApJ*, 476:291–310.
- Knigge, C., K. S. Long, R. A. Wade, R. Baptista, K. Horne, I. Hubeny, and R. G. M. Rutten
1998a. Hubble Space Telescope Eclipse Observations of the Nova-like Cataclysmic Variable UX Ursae Majoris. *ApJ*, 499:414–428.
- Knigge, C., K. S. Long, R. A. Wade, R. Baptista, K. Horne, I. Hubeny, and R. G. M. Rutten
1998b. Hubble Space Telescope Eclipse Observations of the Nova-like Cataclysmic Variable UX Ursae Majoris. *ApJ*, 499:414.
- Knigge, C., S. Scaringi, M. R. Goad, and C. E. Cottis
2008. The intrinsic fraction of broad-absorption line quasars. *MNRAS*, 386:1426–1435.

- Knigge, C., J. A. Woods, and J. E. Drew
1995. The application of Monte Carlo methods to the synthesis of spectral line profiles arising from accretion disc winds. *MNRAS*, 273:225–248.
- Körding, E., M. Rupen, C. Knigge, R. Fender, V. Dhawan, M. Templeton, and T. Muxlow
2008. A Transient Radio Jet in an Erupting Dwarf Nova. *Science*, 320:1318–.
- Kotov, O., E. Churazov, and M. Gilfanov
2001. On the X-ray time-lags in the black hole candidates. *MNRAS*, 327:799–807.
- Krolik, J. H. and M. C. Begelman
1986. The Dynamical State of the Obscuring Torus in Seyfert Galaxies. In *Bulletin of the American Astronomical Society*, volume 18 of *BAAS*, P. 903.
- Krolik, J. H., C. F. McKee, and C. B. Tarter
1981. Two-phase models of quasar emission line regions. *ApJ*, 249:422–442.
- Krolik, J. H. and G. M. Voit
1998. What Is the True Covering Factor of Absorbing Matter in BALQSOs? *ApJ Letters*, 497:L5–L8.
- Kromer, M. and S. A. Sim
2009. Time-dependent three-dimensional spectrum synthesis for Type Ia supernovae. *MNRAS*, 398:1809–1826.
- Kurosawa, R. and D. Proga
2009. Three-Dimensional Simulations of Dynamics of Accretion Flows Irradiated by a Quasar. *ApJ*, 693:1929–1945.
- Kurucz, R. L.
1991. New Opacity Calculations. In *NATO ASIC Proc. 341: Stellar Atmospheres - Beyond Classical Models*, L. Crivellari, I. Hubeny, and D. G. Hummer, eds., P. 441.
- Kuulkers, E., S. Motta, J. Kajava, J. Homan, R. Fender, and P. Jonker
2015. Renewed activity of V404 Cyg (GS 2023+338). *The Astronomer's Telegram*, 7647.
- La Dous, C.
1989a. On the Balmer jump in dwarf novae during the outburst. *MNRAS*, 238:935–943.
- La Dous, C.
1989b. Synthetic optical and ultraviolet spectra of stationary accretion disks. *A&A*, 211:131–155.

- Lamy, H. and D. Hutsemékers
2000. Spectropolarimetry of the iron low ionization broad absorption line quasar Q 0059-2735. *A&A*, 356:L9–L12.
- Landi, E., G. Del Zanna, P. R. Young, K. P. Dere, and H. E. Mason
2012. CHIANTI—An Atomic Database for Emission Lines. XII. Version 7 of the Database. *ApJ*, 744:99.
- Laor, A. and W. N. Brandt
2002. The Luminosity Dependence of Ultraviolet Absorption in Active Galactic Nuclei. *ApJ*, 569:641–654.
- Long, K. S., W. P. Blair, A. F. Davidsen, C. W. Bowers, W. V. D. Dixon, S. T. Durrance, P. D. Feldman, R. C. Henry, G. A. Kriss, J. W. Kruk, H. W. Moos, O. Vancura, H. C. Ferguson, and R. A. Kimble
1991. Spectroscopy of Z Camelopardalis in outburst with the Hopkins Ultraviolet Telescope. *ApJ Letters*, 381:L25–L29.
- Long, K. S. and C. Knigge
2002. Modeling the Spectral Signatures of Accretion Disk Winds: A New Monte Carlo Approach. *ApJ*, 579:725–740.
- Long, K. S., R. A. Wade, W. P. Blair, A. F. Davidsen, and I. Hubeny
1994. Observations of the bright novalike variable IX Velorum with the Hopkins Ultraviolet Telescope. *ApJ*, 426:704–715.
- Longmore, A. J., T. J. Lee, D. A. Allen, and D. J. Adams
1981. Infrared observations of the cataclysmic variable RW Tri. *MNRAS*, 195:825–830.
- Lucy, L. B.
2002. Monte Carlo transition probabilities. *A&A*, 384:725–735.
- Lucy, L. B.
2003. Monte Carlo transition probabilities. II. *A&A*, 403:261–275.
- Lucy, L. B. and P. M. Solomon
1970. Mass Loss by Hot Stars. *ApJ*, 159:879.
- Lyubarskii, Y. E.
1997. Flicker noise in accretion discs. *MNRAS*, 292:679.
- MacGregor, K. B., L. Hartmann, and J. C. Raymond
1979. Radiative amplification of sound waves in the winds of O and B stars. *ApJ*, 231:514–523.

- Marinucci, A., S. Bianchi, G. Matt, D. M. Alexander, M. Baloković, F. E. Bauer, W. N. Brandt, P. Gandhi, M. Guainazzi, F. A. Harrison, K. Iwasawa, M. Koss, K. K. Madsen, F. Nicastro, S. Puccetti, C. Ricci, D. Stern, and D. J. Walton
2016. NuSTAR catches the unveiling nucleus of NGC 1068. *MNRAS*, 456:L94–L98.
- Marscher, A. P.
2006. Relativistic Jets in Active Galactic Nuclei. In *Relativistic Jets: The Common Physics of AGN, Microquasars, and Gamma-Ray Bursts*, P. A. Hughes and J. N. Bregman, eds., volume 856 of *American Institute of Physics Conference Series*, Pp. 1–22.
- Marsh, T. R. and K. Horne
1990. Emission-line mapping of the dwarf nova IP Pegasi in outburst and quiescence. *ApJ*, 349:593–607.
- Mathur, S., P. J. Green, N. Arav, M. Brotherton, M. Crenshaw, M. deKool, M. Elvis, R. W. Goodrich, F. Hamann, D. C. Hines, V. Kashyap, K. Korista, B. M. Peterson, J. C. Shields, I. Shlosman, W. van Breugel, and M. Voit
2000. Thomson Thick X-Ray Absorption in a Broad Absorption Line Quasar, PG 0946+301. *ApJ Letters*, 533:L79–L82.
- Matt, G., M. Guainazzi, and R. Maiolino
2003. Changing look: from Compton-thick to Compton-thin, or the rebirth of fossil active galactic nuclei. *MNRAS*, 342:422–426.
- Matthews, J. H., C. Knigge, K. S. Long, S. A. Sim, and N. Higginbottom
2015. The impact of accretion disc winds on the optical spectra of cataclysmic variables. *MNRAS*, 450:3331–3344.
- Mauche, C. W. and J. C. Raymond
1987. IUE observations of the dwarf nova HL Canis Majoris and the winds of cataclysmic variables. *ApJ*, 323:690–713.
- McConnell, N. J. and C.-P. Ma
2013. Revisiting the Scaling Relations of Black Hole Masses and Host Galaxy Properties. *ApJ*, 764:184.
- McHardy, I. M., E. Koerding, C. Knigge, P. Uttley, and R. P. Fender
2006. Active galactic nuclei as scaled-up Galactic black holes. *Nature*, 444:730–732.
- Mihalas, D. M.
1982. *Stellar atmospheres*.

- Motta, S., A. Beardmore, S. Oates, N. P. M. K. A. Sanna, E. Kuulkers, J. Kajava, and C. Sanchez-Fernandez
2015. X-ray and optical/UV variability from V404 Cyg (GS 2023+338) observed by Swift (part 1 of 2). *The Astronomer's Telegram*, 7665.
- Murray, N. and J. Chiang
1996. Wind-dominated optical line emission from accretion disks around luminous cataclysmic variable stars. *Nature*, 382:789–791.
- Murray, N. and J. Chiang
1997. Disk Winds and Disk Emission Lines. *ApJ*, 474:91–103.
- Murray, N., J. Chiang, S. A. Grossman, and G. M. Voit
1995. Accretion Disk Winds from Active Galactic Nuclei. *ApJ*, 451:498.
- Netzer, H.
1990. AGN emission lines. In *Active Galactic Nuclei*, R. D. Blandford, H. Netzer, L. Woltjer, T. J.-L. Courvoisier, and M. Mayor, eds., Pp. 57–160.
- Neugebauer, G., J. B. Oke, E. E. Becklin, and K. Matthews
1979. Absolute spectral energy distribution of quasi-stellar objects from 0.3 to 10 microns. *ApJ*, 230:79–94.
- Neustroev, V. V., V. F. Suleimanov, N. V. Borisov, K. V. Belyakov, and A. Shearer
2011. Dark spot, spiral waves and the SW Sextantis behaviour: it is all about UX Ursae Majoris. *MNRAS*, 410:963–977.
- Noebauer, U. M., K. S. Long, S. A. Sim, and C. Knigge
2010. The Geometry and Ionization Structure of the Wind in the Eclipsing Nova-like Variables RW Tri and UX UMa. *ApJ*, 719:1932–1945.
- O'Dowd, M. J., N. F. Bate, R. L. Webster, K. Labrie, and J. Rogers
2015. Microlensing Constraints on Broad Absorption and Emission Line Flows in the Quasar H1413+117. *ArXiv e-prints*.
- Osterbrock, D. E.
1989. *Astrophysics of gaseous nebulae and active galactic nuclei*.
- Owocki, S. P. and G. B. Rybicki
1984. Instabilities in line-driven stellar winds. I - Dependence on perturbation wavelength. *ApJ*, 284:337–350.
- Owocki, S. P. and G. B. Rybicki
1985. Instabilities in line-driven stellar winds. II - Effect of scattering. *ApJ*, 299:265–276.

- Patterson, J., R. Patino, J. R. Thorstensen, D. Harvey, D. R. Skillman, and F. A. Ringwald
1996. Periods and Quasiperiods in the Cataclysmic Variable BZ Camelopardalis. *AJ*, 111:2422.
- Pelletier, G. and R. E. Pudritz
1992. Hydromagnetic disk winds in young stellar objects and active galactic nuclei. *ApJ*, 394:117–138.
- Perley, R. A., J. W. Dreher, and J. J. Cowan
1984. The jet and filaments in Cygnus A. *ApJ Letters*, 285:L35–L38.
- Ponti, G., R. P. Fender, M. C. Begelman, R. J. H. Dunn, J. Neilsen, and M. Coriat
2012. Ubiquitous equatorial accretion disc winds in black hole soft states. *MNRAS*, 422:L11.
- Potash, R. I. and J. F. C. Wardle
1980. 4C 32.69 - A quasar with a radio jet. *ApJ*, 239:42–49.
- Pounds, K. A. and J. N. Reeves
2009. Quantifying the fast outflow in the luminous Seyfert galaxy PG1211+143. *MNRAS*, 397:249–257.
- Prinja, R. K., F. A. Ringwald, R. A. Wade, and C. Knigge
2000. HST ultraviolet observations of rapid variability in the accretion-disc wind of BZ Cam. *MNRAS*, 312:316–326.
- Proga, D., Y.-F. Jiang, S. W. Davis, J. M. Stone, and D. Smith
2014. The Effects of Irradiation on Cloud Evolution in Active Galactic Nuclei. *ApJ*, 780:51.
- Proga, D. and T. R. Kallman
2004. Dynamics of Line-driven Disk Winds in Active Galactic Nuclei. II. Effects of Disk Radiation. *ApJ*, 616:688–695.
- Proga, D., T. R. Kallman, J. E. Drew, and L. E. Hartley
2002. Resonance Line Profile Calculations Based on Hydrodynamical Models of Cataclysmic Variable Winds. *ApJ*, 572:382–391.
- Proga, D. and R. Kurosawa
2010. Outflows from AGN: Their Impact on Spectra and the Environment. In *Accretion and Ejection in AGN: a Global View*, L. Maraschi, G. Ghisellini, R. Della Ceca, and F. Tavecchio, eds., volume 427 of *Astronomical Society of the Pacific Conference Series*, P. 41.

- Proga, D., J. M. Stone, and J. E. Drew
1998. Radiation-driven winds from luminous accretion discs. *MNRAS*, 295:595.
- Proga, D., J. M. Stone, and T. R. Kallman
2000. Dynamics of Line-driven Disk Winds in Active Galactic Nuclei. *ApJ*, 543:686–696.
- Puccetti, S., F. Fiore, G. Risaliti, M. Capalbi, M. Elvis, and F. Nicastro
2007. Rapid N_H changes in NGC 4151. *MNRAS*, 377:607–616.
- Puebla, R. E., M. P. Diaz, D. J. Hillier, and I. Hubeny
2011. A Method for the Study of Accretion Disk Emission in Cataclysmic Variables. I. The Model. *ApJ*, 736:17.
- Reeves, J. N., P. T. O'Brien, and M. J. Ward
2003. A Massive X-Ray Outflow from the Quasar PDS 456. *ApJ Letters*, 593:L65–L68.
- Reichard, T. A., G. T. Richards, P. B. Hall, D. P. Schneider, D. E. Vanden Berk, X. Fan, D. G. York, G. R. Knapp, and J. Brinkmann
2003. Continuum and Emission-Line Properties of Broad Absorption Line Quasars. *AJ*, 126:2594–2607.
- Ringwald, F. A. and T. Naylor
1998. High-speed optical spectroscopy of a cataclysmic variable wind - BZ Camelopardalis. *AJ*, 115:286.
- Risaliti, G., M. Elvis, and F. Nicastro
2002. Ubiquitous Variability of X-Ray-absorbing Column Densities in Seyfert 2 Galaxies. *ApJ*, 571:234–246.
- Risaliti, G., M. Salvati, and A. Marconi
2011. [O III] equivalent width and orientation effects in quasars. *MNRAS*, 411:2223–2229.
- Rottenberg, J. A.
1952. Theoretical line profiles for stars of P Cygni type. *MNRAS*, 112:125.
- Rutten, R. G. M., J. van Paradijs, and J. Tinbergen
1992. Reconstruction of the accretion disk in six cataclysmic variable stars. *A&A*, 260:213–226.
- Rybicki, G. B. and D. G. Hummer
1978. A generalization of the Sobolev method for flows with nonlocal radiative coupling. *ApJ*, 219:654–675.

- Scaringi, S., E. Körding, P. Uttley, C. Knigge, P. J. Groot, and M. Still
2012. The universal nature of accretion-induced variability: the rms-flux relation in an accreting white dwarf. *MNRAS*, 421:2854–2860.
- Scaringi, S., T. J. Maccarone, E. Koerding, C. Knigge, S. Vaughan, T. R. Marsh, E. Aranzana, V. Dhillon, and S. C. C. Barros
2015. Accretion-induced variability links young stellar objects, white dwarfs, and black holes. *ArXiv e-prints*.
- Schwarzenberg-Czerny, A. and M. Rózyczka
1977. Theoretical UVB colours of accretion discs in cataclysmic variables. *ACTAA*, 27:429–436.
- Seaton, M. J.
1959. The solution of capture-cascade equations for hydrogen. *MNRAS*, 119:90.
- Seyfert, C. K.
1943. Nuclear Emission in Spiral Nebulae. *ApJ*, 97:28.
- Shakura, N. I. and R. A. Sunyaev
1973. Black holes in binary systems. Observational appearance. *A&A*, 24:337–355.
- Shaviv, G. and R. Wehrse
1991. Continuous energy distributions of accretion discs. *A&A*, 251:117–132.
- Shen, Y., G. T. Richards, M. A. Strauss, P. B. Hall, D. P. Schneider, S. Snedden, D. Bizyaev, H. Brewington, V. Malanushenko, E. Malanushenko, D. Oravetz, K. Pan, and A. Simmons
2011. A Catalog of Quasar Properties from Sloan Digital Sky Survey Data Release 7. *ApJs*, 194:45.
- Shlosman, I. and P. Vitello
1993. Winds from accretion disks - Ultraviolet line formation in cataclysmic variables. *ApJ*, 409:372–386.
- Shlosman, I., P. A. Vitello, and G. Shaviv
1985. Active galactic nuclei - Internal dynamics and formation of emission clouds. *ApJ*, 294:96–105.
- Silk, J. and M. J. Rees
1998. Quasars and galaxy formation. *A&A*, 331:L1–L4.
- Sim, S. A.
2004. Mass-loss rates for hot luminous stars: the influence of line branching. *MNRAS*, 349:899–908.

- Sim, S. A., J. E. Drew, and K. S. Long
2005. Two-dimensional Monte Carlo simulations of HI line formation in massive young stellar object disc winds. *MNRAS*, 363:615–627.
- Sim, S. A., K. S. Long, L. Miller, and T. J. Turner
2008. Multidimensional modelling of X-ray spectra for AGN accretion disc outflows. *MNRAS*, 388:611–624.
- Sim, S. A., L. Miller, K. S. Long, T. J. Turner, and J. N. Reeves
2010. Multidimensional modelling of X-ray spectra for AGN accretion disc outflows - II. *MNRAS*, 404:1369–1384.
- Sim, S. A., D. Proga, R. Kurosawa, K. S. Long, L. Miller, and T. J. Turner
2012. Synthetic X-ray spectra for simulations of the dynamics of an accretion flow irradiated by a quasar. *MNRAS*, 426:2859–2869.
- Simon, L. E. and F. Hamann
2010. The origins of a rich absorption line complex in a quasar at redshift 3.45. *MNRAS*, 409:269–283.
- Smak, J.
1981. On the Emission Lines from Rotating Gaseous Disks. *ACTAA*, 31:395.
- Smak, J.
1995. Eclipses in Cataclysmic Variables with Stationary Accretion Disks. V. RW Tri. *ACTAA*, 45:259–277.
- Sobolev, V. V.
1957. The Diffusion of La Radiation in Nebulae and Stellar Envelopes. *SvA*, 1:678.
- Sobolev, V. V.
1960. *Moving envelopes of stars*.
- Springel, V., T. Di Matteo, and L. Hernquist
2005. Black Holes in Galaxy Mergers: The Formation of Red Elliptical Galaxies. *ApJ Letters*, 620:L79–L82.
- Sutherland, R. S.
1998. Accurate free-free Gaunt factors for astrophysical plasmas. *MNRAS*, 300:321–330.
- Tatum, M. M., T. J. Turner, S. A. Sim, L. Miller, J. N. Reeves, A. R. Patrick, and K. S. Long
2012. Modeling the Fe K Line Profiles in Type I Active Galactic Nuclei with a Compton-thick Disk Wind. *ApJ*, 752:94.

- Tothline, J. E. and D. E. Osterbrock
1976. Variation of the spectrum of the Seyfert galaxy NGC 7603. *ApJ Letters*, 210:L117–L120.
- Tombesi, F., M. Cappi, J. N. Reeves, G. G. C. Palumbo, T. Yaqoob, V. Braito, and M. Dadina
2010. Evidence for ultra-fast outflows in radio-quiet AGNs. I. Detection and statistical incidence of Fe K-shell absorption lines. *A&A*, 521:A57.
- Turner, T. J. and L. Miller
2009. X-ray absorption and reflection in active galactic nuclei. *AAPR*, 17:47–104.
- Urry, C. M. and P. Padovani
1995. Unified Schemes for Radio-Loud Active Galactic Nuclei. *PASP*, 107:803.
- Uttley, P. and I. M. McHardy
2001. The flux-dependent amplitude of broadband noise variability in X-ray binaries and active galaxies. *MNRAS*, 323:L26–L30.
- Uttley, P., I. M. McHardy, and S. Vaughan
2005. Non-linear X-ray variability in X-ray binaries and active galaxies. *MNRAS*, 359:345–362.
- Šurlan, B., W.-R. Hamann, J. Kubát, L. M. Oskinova, and A. Feldmeier
2012. Three-dimensional radiative transfer in clumped hot star winds. I. Influence of clumping on the resonance line formation. *A&A*, 541:A37.
- Van de Sande, M., S. Scaringi, and C. Knigge
2015. The rms-flux relation in accreting white dwarfs: another nova-like variable and the first dwarf nova. *MNRAS*, 448:2430–2437.
- van Regemorter, H.
1962. Rate of Collisional Excitation in Stellar Atmospheres. *ApJ*, 136:906.
- Verner, D. A., G. J. Ferland, K. T. Korista, and D. G. Yakovlev
1996. Atomic Data for Astrophysics. II. New Analytic FITS for Photoionization Cross Sections of Atoms and Ions. *ApJ*, 465:487.
- Wade, R. A.
1984. A double grid of accretion disc model spectra for cataclysmic variable stars. *MNRAS*, 208:381–398.
- Wade, R. A.
1988. A test of synthetic accretion disk spectra using ultraviolet flux distributions of novalike variables. *ApJ*, 335:394–405.

- Walker, M. F.
1963. Photoelectric Observations of RW Trianguli. *ApJ*, 137:485.
- Weymann, R. J., S. L. Morris, C. B. Foltz, and P. C. Hewett
1991. Comparisons of the emission-line and continuum properties of broad absorption line and normal quasi-stellar objects. *ApJ*, 373:23–53.
- Weymann, R. J., J. S. Scott, A. V. R. Schiano, and W. A. Christiansen
1982. A thermal wind model for the broad emission line region of quasars. *ApJ*, 262:497–510.
- Woltjer, L.
1959. Emission Nuclei in Galaxies. *ApJ*, 130:38.
- Woods, D. T., R. I. Klein, J. I. Castor, C. F. McKee, and J. B. Bell
1996. X-Ray-heated Coronae and Winds from Accretion Disks: Time-dependent Two-dimensional Hydrodynamics with Adaptive Mesh Refinement. *ApJ*, 461:767.
- Woods, J. A.
1991. PhD thesis, D. Phil thesis, Univ. Oxford , (1991).
- Zhou, H., T. Wang, H. Wang, J. Wang, W. Yuan, and Y. Lu
2006. Polar Outflows in Six Broad Absorption Line Quasars. *ApJ*, 639:716–723.